

**FEDERAL UNIVERSITY OF AMAZONAS  
PRO-RECTORY OF RESEARCH AND POSGRADUATE  
POSTGRADUATE PROGRAM IN PHYSICS**

YAN MATHEUS COLARES PINTO

**UNDERSTANDING THE LITHIUM SALTS EFFECTS ON  
PVA-BASED MEMBRANES FROM AN EXPERIMENTAL  
VISION FOR SOLID-STATE ELECTROLYTES**

Support



Manaus-AM

2025

YAN MATHEUS COLARES PINTO

**UNDERSTANDING THE LITHIUM SALTS EFFECTS ON  
PVA-BASED MEMBRANES FROM AN EXPERIMENTAL  
VISION FOR SOLID-STATE ELECTROLYTES**

Thesis presented to the Postgraduate Program in Physics at the Federal University of Amazonas, as a partial requirement for obtaining the degree of Doctor in Physics.

Concentration area: Condensed Matter Physics.

Advisor: Prof. Dr. Yurimiler Leyet Ruiz.

Co-Advisor: Prof. Dra. Lianet A. Domínguez.

Manaus-AM

2025

Ficha Catalográfica

Elaborada automaticamente de acordo com os dados fornecidos pelo(a) autor(a).

---

P659u      Pinto, Yan Matheus Colares  
Understanding the lithium salts effects on PVA-based membranes from an experimental vision for solid-state electrolytes / Yan Matheus Colares Pinto. - 2025.  
111 f. : il., p&b. ; 31 cm.

Orientador(a): Yurimiler Leyet Ruiz.  
Coorientador(a): Lianet Aguilera Domínguez .  
Tese (doutorado) - Universidade Federal do Amazonas, Programa de Pós-Graduação em Física, Manaus-AM, 2025.

1. Electrolyte. 2. Membrane. 3. Lithium salts. 4. Impedance. 5. Conductivity. I. Ruiz, Yurimiler Leyet. II. Domínguez, Lianet Aguilera. III. Universidade Federal do Amazonas. Programa de Pós-Graduação em Física. IV. Título

---

*To my wife and children,  
Jackeline, Yelena, and Heitor,  
whose smile gives meaning to every effort.*

## ACKNOWLEDGMENTS

First, I thank God for giving meaning to every step of this journey and for guiding me toward another achievement. I am also deeply grateful to my family, who have always supported me: my parents, José Raimundo and Concilei Colares; my siblings, Nicléa, Yon, Yago, and Yasmin.

I thank my friends and colleagues from the PPGFIS program, Luã Catique, Placilene Cardoso, Henrique Pecinatto, Salomão dos Santos, Jamilton Boaes, Priscila de Carvalho, Thainnar Sales, Cássio Macêdo, Lilian Rodrigues, Cleverton Dias, and Philippe Soares for their partnership, support, and encouragement throughout my Master's and Doctoral studies.

I am also grateful to the professors who, directly or indirectly, helped shape my academic path, from undergraduate studies at UEA to postgraduate studies at UFAM: Prof. Angsula Gosh, Prof. Edgar Aparecido Sanchez, Prof. Hidemberg Ordozgoith da Frota, Prof. Fidel Zayas, Prof. Marceliano Oliveira, Prof. Adriano Márcio dos Santos, and Prof. Júlio César da Fonseca. My sincere thanks go to Prof. Wautraud M. Kriven for her guidance and collaboration during my Ph.D. research as a visiting student at the University of Illinois Urbana-Champaign (UIUC).

I owe heartfelt gratitude to my advisor, Prof. Yurimiler Leyet, and my co-advisor, Lianet Aguilera, for welcoming me into their group and for their patience, support, and encouragement throughout my development as an experimental physicist. I also appreciate the entire team at the Laboratory of Technological Materials Processing (LPMat): Juliana Pereira, Jardson Braz, Ariel Delgado, Eliezer Costa, Ana Carolina, Sávio Bentes, Carlos Yago Batista, and Rodrigo Lavareda and all other researchers and collaborators.

Finally, I thank CAPES and FAPEAM for their financial support, and PPGFIS-UFAM for the laboratory infrastructure and all the opportunities to learn.

## RESUMO

A crescente demanda por dispositivos de armazenamento de energia mais seguros, estáveis e eficientes tem motivado o desenvolvimento de eletrólitos poliméricos sólidos, capazes de melhorar o desempenho e a segurança das baterias modernas. Nesse contexto, este trabalho tem como objetivo investigar a influência de diferentes concentrações de sais iônicos em membranas poliméricas à base de álcool polivinílico (PVA), visando seu uso nessa aplicação. As membranas de PVA com adição de hidróxido de lítio (LiOH) nas concentrações de 1, 3, 5, 7 e 9% e perclorato de lítio (LiClO<sub>4</sub>) nas concentrações de 1, 5 e 10% foram obtidas por moldagem via evaporação de solvente (SCM) e caracterizadas quanto às propriedades estruturais, morfológicas, térmicas, mecânicas e iônicas. A espectroscopia de infravermelho por transformada de Fourier (FT-IR) indicou interações entre os íons Li<sup>+</sup> e a matriz polimérica, resultado confirmado pelos cálculos de teoria funcional da densidade (DFT), que apontaram um mecanismo de forte coordenação iônica com energia de formação de  $-1,27$  eV e comprimento de ligação Li–O entre  $1,85$  Å e  $1,96$  Å, em função do aumento da proporção de sais. Complementarmente, a difração de raios X (DRX) revelou fase monoclinica (grupo espacial P2<sub>1</sub>/m) e cristalinidades próximas a 30%, classificando os materiais como semicristalinos. A caracterização térmica por análise termogravimétrica e calorimetria diferencial (TGA/DSC) mostrou boa correlação com os dados de DRX, além do aumento das temperaturas de transição, atingindo  $T_g = 84,3$  °C,  $T_m = 199,5$  °C e  $T_D = 299$  °C até 9% de LiOH e 5% de LiClO<sub>4</sub>, com queda apenas na amostra com 10% de perclorato. As imagens de microscopia eletrônica de varredura (SEM) evidenciaram superfícies suaves e sinais de tensões internas em concentrações elevadas de sal, especialmente com LiClO<sub>4</sub>, por isso, o desempenho mecânico foi avaliado por análise mecânica dinâmica (DMA) e testes de tração, revelando módulo de armazenamento na faixa dos MPa e alongamento acima de 300%, indicando boa flexibilidade e integridade estrutural. Adicionalmente, as propriedades de transporte iônico foram investigadas pela espectroscopia de impedância complexa (CIS), com análise baseada em modelos de circuitos equivalentes, função de Havriliak–Negami e lei de potência de Jonscher. Ambos os sistemas apresentaram melhorias na condutividade iônica, com valores da ordem de  $10^{-6}$  S/cm e  $10^{-5}$  S/cm e tempos de relaxação de  $10^{-5}$  s. Esses resultados demonstram o potencial das membranas como candidatas promissoras a eletrólitos sólidos em dispositivos de armazenamento de energia avançados.

**Palavras-chave:** Eletrólito, Membrana, Sais de lítio, Impedância, Condutividade.

## ABSTRACT

The growing demand for safer, more stable, and efficient energy storage devices has driven the development of solid polymer electrolytes, which can enhance both the performance and safety of modern batteries. In this context, the present work aims to investigate the influence of different concentrations of ionic salts on poly(vinyl alcohol) (PVA)-based polymer membranes, aiming at their use in this application. PVA membranes with the addition of lithium hydroxide (LiOH) at concentrations 1, 3, 5, 7, and 9% and lithium perchlorate (LiClO<sub>4</sub>) at concentrations 1, 5, and 10% were prepared using the solvent casting method (SCM) and characterized with respect to their structural, morphological, thermal, mechanical, and ionic properties. Fourier-transform infrared (FT-IR) spectroscopy indicated interactions between Li<sup>+</sup> ions and the polymer matrix, as confirmed by density functional theory (DFT) calculations, which revealed a strong ionic coordination mechanism with formation energies of –1.27 eV and Li–O bond lengths ranging from 1.85 Å to 1.96 Å, depending on the increasing salt content. Complementarily, X-ray diffraction (XRD) revealed a monoclinic phase (space group P2<sub>1</sub>/m) and crystallinities close to 30%, classifying the materials as semicrystalline. Thermal characterization by thermogravimetric analysis and differential scanning calorimetry (TGA/DSC) showed good correlation with the XRD data, in addition to increased transition temperatures, reaching  $T_g = 84.3$  °C,  $T_m = 199.5$  °C, and  $T_D = 299$  °C for up to 9% LiOH and 5% LiClO<sub>4</sub>, with a decrease observed only in the sample containing 10% perchlorate. Scanning electron microscopy (SEM) images revealed smooth surfaces and signs of internal stress at high salt concentrations, particularly with LiClO<sub>4</sub>, prompting the evaluation of mechanical performance by dynamic mechanical analysis (DMA) and tensile testing, which showed storage modulus values in the MPa range and elongation above 300%, indicating good flexibility and structural integrity. Additionally, ionic transport properties were investigated by complex impedance spectroscopy (CIS), with analysis based on equivalent circuit models, the Havriliak–Negami function, and Jonscher’s power law. Both systems exhibited improvements in ionic conductivity, with values on the order of 10<sup>–6</sup> S/cm and 10<sup>–5</sup> S/cm, and relaxation times of 10<sup>–5</sup> s. These results demonstrate the potential of the membranes as promising candidates for solid electrolytes in advanced energy storage devices.

**keywords:** Electrolyte, Membrane, Lithium salts, Impedance, Conductivity.

## LIST OF FIGURES

2.1	Representation of Voltaic Pile [1]. . . . .	6
2.2	Comparison of Acid-Lead, NiCd, NiMH, and Lithium secondary batteries [2]. . . . .	8
2.3	Stages of fires and explosions in liquid batteries due to overcharging, high currents, or internal shorts [3]. . . . .	9
2.4	Battery model based on solid ion-lithium electrolyte. Components: electrodes, separator, and electrolyte [4]. . . . .	10
2.5	Amorphous and crystallite portions of polymer morphology and crystallinity [5]. . . . .	11
2.6	Classification of polymer electrolytes. Source: Author. . . . .	12
2.7	Most used Polymer Hosts in polymeric membranes. The side molecular groups help to form the GPEs, SPEs and CPEs dissociating additive materials [6]. . . . .	14
2.8	SCM synthesis method steps [6]. . . . .	15
2.9	Setup and method of the Electrospinning synthesis [7]. . . . .	16
2.10	Illustration of phase inversion method [8]. . . . .	17
2.11	Comparison of different characteristics of lithium salt, adapted from [3]. . . . .	19
2.12	Interchain and Intrachain ion hopping and ion cluster hopping mechanisms in a Polymer Matrix [9]. . . . .	20
2.13	PVAs mer, n and m repetitions when partially hydrolized and pure mer for fully hydrolized [10]. . . . .	21
2.14	PVA structure by Brun et al. c and b projections [11]. . . . .	23
3.1	Impedance graphs of single and combined electric elements. They represent: A) Resistance, B) Capacitor, C) Inductor, D) CPE element, E) Finite Lenght Warburg and F) RC circuit. . . . .	31



3.2	Representative log–log plot of $\sigma'_{\text{elec}}$ , as a function of frequency at constant temperature, illustrating the typical behavior of disordered conductive materials. [12]. . . . .	36
4.1	Vibrational modes associated to molecular dipole moment [13]. . . . .	42
4.2	Bragg's law illustration based on incident and diffracted X-rays angles, wavelength and distance between structure planes [13]. . . . .	43
4.3	Perkim Elmer DMA 8000 model [14]. . . . .	45
4.4	Standard strain-stress setup [14]. . . . .	47
5.1	A) FT-IR and B) Raman spectra of the membranes with LiOH addition. . . . .	52
5.2	X-ray diffraction patterns of precursor substances (pure PVA and LiOH powders) and PVA/LiOH membranes. . . . .	55
5.3	Fitted experimental X-ray diffraction pattern of the PVA–7% LiOH sample obtained through Rietveld structural refinement. . . . .	55
5.4	PVA's unit cell and mer repetitions. The PVA unit cell, assigned to the monoclinic space group $P2_1/m$ , contains two polymer chains related by a mirror plane, with one being the mirror image of the other. This symmetry promotes packing through intermolecular hydrogen bonding. . . . .	57
5.5	Relaxed structures before and after lithium ion insertion. PVA-1 structure projected onto the $-\mathbf{b} \times \mathbf{a}$ plane and PVA-2 structure projected onto the $-\mathbf{b} \times -\mathbf{c}$ plane. Li–O bond lengths varying approximately between 1.85 Å and 1.96 Å for the PVA-1+Li system, and between 1.87 Å and 1.99 Å for PVA-2+Li. O–H and C–C bond lengths also increased but the presence of lithium maintained the structural stability of both systems. . . . .	59
5.6	Morphology images of the membranes by SEM, labeled from A) to F). Image A) shows the pure PVA membrane, while images B) through F) correspond to membranes with increasing LiOH content at 1%, 3%, 5%, 7%, and 9% (w/w), respectively. . . . .	60
5.7	TG and DTG curves of PVA membrane. Major mass loss peaks are highlighted. . . . .	62

5.8	TG and DSC (exo up convention) curves of PVA/LiOH membranes. Glass and melting temperature are indicated in the graph. . . . .	62
5.9	Cole–Cole plots for PVA-based membranes containing different LiOH concentrations. It is revealing a progressive decrease in bulk resistance. . . . .	65
5.10	Cole–Cole plots were fitted using the ECM. Chi-square and sum of squares statistics are provided to evaluate the accuracy and reliability of the model fits. . . . .	67
5.11	Real and imaginary spectra of the electrical modulus. . . . .	70
5.12	Imaginary part of the electrical modulus fitted by the Havriliak-Negami (HN) model, with parameters $\alpha_{\text{HN}}$ , $\beta_{\text{HN}}$ , and relaxation time $\tau_{\text{HN}}$ . . . . .	71
5.13	Conductivity spectra fitted by Jonscher’s power law for low, medium and high range frequencies. . . . .	72
5.14	Transmittance and Raman intensities of PVA/LiClO <sub>4</sub> . . . . .	74
5.15	A)XRD patterns and B) Comparison of background intensities for different compositions. . . . .	76
5.16	Rietveld structural refinements at different LiClO <sub>4</sub> concentrations. Background and residual curves illustrate the semicrystalline/amorphous nature of the samples. . . . .	77
5.17	Surface morphologies of polymer membranes with the addition of 1% B), 5% C), and 10% D) LiClO <sub>4</sub> in PVA. . . . .	78
5.18	Surface image of PVA membrane containing 10% LiClO <sub>4</sub> , showing the presence of cracks attributed to the high concentration of lithium salt. . . . .	79
5.19	Weight loss and DTG data of the pure PVA membrane A); comparison between pure PVA and PVA/LiClO <sub>4</sub> membranes B); and heat flow data in two different temperature ranges: 10 °C to 120 °C, C) and 100 °C to 200 °C, D). . . . .	80
5.20	Frequency-dependent mechanical response of the material at different LiClO <sub>4</sub> concentrations: (A) real modulus $M'_{\text{mech}}$ ; (B) imaginary modulus $M''_{\text{mech}}$ ; (C) loss factor $\tan \delta$ . . . . .	82

5.21 Strain–Stress and Tensile limit at failure. Transition between elastic and plastic behaviors are separated by dashed lines. . . . .	84
5.22 Calculated Young Modulus and Toughness. . . . .	85
5.23 Cole-Cole fitting By Equivalent Circuit Model. . . . .	86
5.24 Cole–Cole plots for PVA-based polymer membranes containing different LiOH concentrations, showing a progressive decrease in bulk resistance. . . . .	87
5.25 The real component of the electrical modulus indicates an insulating dielectric behavior for PVA and 1% LiClO <sub>4</sub> , while the imaginary component shows a shift of the peaks toward higher frequencies. . . . .	89
5.26 HN model fitting peaks and their parameters. . . . .	89

# LIST OF TABLES

2.1	Degree of hydrolysis for various commercial PVA grades along with the associated residual content PVAc[15]. . . . .	21
2.2	DP, Mn, and solution viscosity of four commercial grades of PVA [16]. . . . .	22
2.3	Conductivity and solvent systems of lithium-based polymer composites comprising either single-polymer matrices or dual-polymer blends. . . . .	26
2.4	Mw and Degree of Hydrolysis of PVA-based composites. . . . .	27
3.1	Impedance equations of ideal and non-ideal electrical elements used in equivalent circuit modeling. . . . .	30
3.2	Comprehensive matrix illustrating the mathematical relationships between the complex electrical formalisms $M_{elec}^*$ (modulus), $Z^*$ (impedance), $Y^*$ (admittance), and $\epsilon_{elec}^*$ (permittivity), commonly used in CIS [17]. . . . .	34
4.1	Sample thicknesses for different PVA-based membranes. Thickness of approximately 0.1 mm ( $\pm 0.025$ mm) and diameter of 1.60 cm ( $\pm 0.010$ cm). . . . .	41
5.1	Assignments of FT-IR and Raman for PVA. (stretching = $\nu$ , bending = $\delta$ , wagging = $\gamma$ , rocking = $\rho$ ). . . . .	53
5.2	Force constant values corresponding to the effects of lithium ions on PVA bonding, obtained through the diatomic molecule vibrational oscillator model, utilizing FT-IR-derived wavenumbers. . . . .	54
5.3	PVA lattice parameters (monoclinic symmetry, space group $P2_1/m$ , $\alpha = \gamma = 90^\circ$ ) and crystallinity obtained from Rietveld refinement and literature. . . . .	57
5.4	Formation energies ( $E_F$ ) for PVA conformations with Li adsorption . . . . .	58
5.5	Elemental composition of the analyzed samples as determined by EDS, presented in weight percent (Wt%) along with the associated standard deviations ( $\sigma_{EDS}$ ). . . . .	61

<i>List of Tables</i>	xii
5.6 Glass transition, melting and decomposition temperatures, enthalpy ( $\Delta H_m$ ), and crystallinity ( $X_c$ ) of the PVA and PVA/LiOH samples. . . . .	64
5.7 Electrical circuit elements and their corresponding fitted values obtained from the CIS analysis of PVA and PVA–7% LiOH membranes. . . . .	69
5.8 Bulk resistance ( $R_b$ ) and calculated DC conductivity ( $\sigma_{DC}$ ) for PVA-based membranes with different LiOH contents. . . . .	69
5.9 Values of $s$ , $R$ , and $\chi$ parameters and their respective errors for different frequency ranges, obtained by fitting the conductivity data using Jon-scher’s model. . . . .	73
5.10 Lattice parameters $a$ , $b$ , and $c$ , monoclinic angle $\beta$ , and unit cell volume of PVA/LiClO <sub>4</sub> composites, determined through Rietveld refinement analysis, alongside their corresponding crystallinity indices. . . . .	77
5.11 Elemental composition by EDS – Comparison between PVA sample and PVA with 10% LiClO <sub>4</sub> . . . . .	79
5.12 Thermal properties ( $T_D$ , $\Delta H_m$ ) and crystallinity ( $X_c$ ) of the PVA and PVA/LiClO <sub>4</sub> samples. . . . .	81
5.13 Electrical elements and their values from CIS fitting of PVA and PVA–LiClO <sub>4</sub> membranes. . . . .	88
5.14 Measured bulk resistance ( $R_b$ ) and corresponding DC conductivity ( $\sigma_{DC}$ ) values for PVA–LiClO <sub>4</sub> membranes. . . . .	88
5.15 Comparison of calculated $\sigma_{DC}$ values for PVA-based membranes synthe-sized with the results reported in the literature. . . . .	91

## **LIST OF ABBREVIATIONS AND ACRONYMS**

PVA	Alcohol Polyvinyl
LiClO <sub>4</sub>	Lithium Perchlorate
LiOH	Lithium Hydroxide
SCM	Solvent Casting Method
SSBs	Solid State Batteries
PEs	Polymeric Electrolytes
CIS	Complex Impedance Spectroscopy
ECM	Equivalent Circuit Model
CPE	Constant Phase Element
DFT	Density Functional Theory
FT-IR	Fourier Transform Infrared Spectroscopy
XRD	X-ray Diffraction
TGA	Thermogravimetric Analysis
DSC	Differential Scanning Calorimetry
DMA	Dynamic Mechanical Analysis
SEM	Scanning Electron Microscopy

# CONTENTS

<b>1</b>	<b>INTRODUCTION</b>	<b>1</b>
<b>2</b>	<b>CONTEXTUALIZATION AND CONCEPTUAL FOUNDATIONS</b>	<b>5</b>
2.1	Primary and Secondary Liquid Batteries and the Technological Advancement of Solid-State Batteries. . . . .	5
2.2	State of the Art . . . . .	9
2.3	Polymer Electrolytes . . . . .	10
2.4	Synthesis method of PEs . . . . .	14
2.5	Ionic Salts and transport mechanisms . . . . .	17
2.6	PVA: structure, properties and composites . . . . .	20
2.6.1	Molecular mer . . . . .	20
2.6.2	Degree of Hydrolysis and its Effects on Mechanical Analysis .	21
2.6.3	Structure and Crystallinity . . . . .	22
2.6.4	Thermal Stability . . . . .	25
2.6.5	Conductivity and composites with PVA matrix . . . . .	25
<b>3</b>	<b>THEORETICAL REVIEW</b>	<b>28</b>
3.1	Impedance Fundamental Elements . . . . .	28
3.1.1	Permittivity and Electric Modulus. . . . .	32
3.2	Conductivity Spectra and Jonscher Model . . . . .	35
3.3	First-Principles Calculations Using DFT: A Literature Review. . . . .	37
<b>4</b>	<b>Methodology</b>	<b>40</b>
4.1	Membranes preparation . . . . .	40

<i>Contents</i>	xv
4.2 Experimental Characterizations . . . . .	41
4.2.1 Fourier Transform Infrared Spectroscopy: . . . . .	41
4.2.2 Raman Spectroscopy: . . . . .	42
4.2.3 X-Ray Diffraction: . . . . .	43
4.2.4 Scanning Electron Microscopy and Energy Dispersive X-ray Spectroscopy: . . . . .	44
4.2.5 Differential Scanning Calorimetry and Thermogravimetric: . .	44
4.2.6 Dynamical Mechanical Analysis: . . . . .	45
4.2.7 Strain-stress tensile test: . . . . .	46
4.2.8 Complex Impedance Spectroscopy: . . . . .	48
4.3 Theoretical calculations: . . . . .	49
4.3.1 DFT approaches. . . . .	49
<b>5 Results and Discussion</b>	<b>51</b>
5.1 PVA/LiOH membranes . . . . .	51
5.1.1 Structural/Morphological Properties Investigated via Experi- mental and theoretical Techniques. . . . .	51
5.1.1.1 Energetic Stability and Lithium Ion Coordination Analysis by DFT . . . . .	57
5.1.1.2 Morphological Characterization of the Samples . .	60
5.1.2 Assessment of Thermal Properties Using Tg and DSC Tech- niques . . . . .	62
5.1.3 Impedance Spectroscopy Analysis of PVA/LiOH Membranes	65
5.2 PVA/LiClO <sub>4</sub> membranes . . . . .	74
5.2.1 Investigation of Structural and Morphological Aspects by Spectroscopic, Crystallographic, and Microscopic Analyses .	74
5.2.2 Thermal Evaluation Using Thermogravimetric and Calorimet- ric Techniques. . . . .	79



<i>Contents</i>	xvi
5.2.3 Mechanical analysis . . . . .	81
5.3 Electrical Characterization and Properties Based on CIS. . . . .	85
5.4 Discussion and Contextualization of the results. . . . .	90
<b>6 CONCLUSIONS</b>	<b>93</b>
6.1 Perspectives for Future Studies . . . . .	95
<b>References</b>	<b>96</b>
<b>Scientific Impacts</b>	<b>109</b>

# 1 INTRODUCTION

The advancement of modern systems is fundamentally grounded in scientific research, where rigorous investigations provide insights into material properties and interactions that are essential for developing and improving technological devices [18]. A comprehensive understanding of these physical and chemical properties drives progress in key sectors such as semiconductors, sensors, and circuits [19], while empirical studies further refine theoretical models to enhance the efficiency of emerging technologies. With increasing demands for innovation, experimental research plays a pivotal role in advancing performance, miniaturization, and energy efficiency [20].

In parallel, research on polymeric membranes has gained global prominence due to their versatile applications, ranging from water reuse in treatment facilities [21] and hydrogen purification to nanoimprint lithography, biomedical materials, and nanocomposite electrolytes for fuel cells [22, 23, 24]. These applications provide a foundation for exploring polymeric membranes in energy storage technologies, particularly in flexible and solid-state batteries (SSBs).

One prominent example of how material research drives innovation is the development of flexible batteries, which are increasingly adopted in high-tech devices due to their shape adaptability through the incorporation of polymeric membranes [3]. Central to the performance of these systems is the solid electrolyte, which enables ion transport between electrodes during charge and discharge processes [25]. By integrating solid electrolytes, SSBs achieve a combination of advantages, including improved safety by minimizing leakage risks, enhanced mechanical stability, longer lifespan, compact design, and higher storage capacity [3].

To achieve these benefits, the choice of electrolyte material is crucial, as it governs ion mobility, structural integrity, and overall performance. In this context, polymeric electrolytes (PEs) stand out for their structural flexibility, thermal stability, and lower flammability risk when prepared in solid or gel form [26, 27]. These materials retain,

or slightly alter, key polymer properties such as crystallinity and exhibit enhanced ionic conductivity upon incorporation of lithium salts such as lithium hexafluorophosphate ( $\text{LiPF}_6$ ),  $\text{LiOH}$ ,  $\text{LiClO}_4$ , and lithium metaborate ( $\text{LiBO}_4$ ) [3, 28]. Thus, the combination of polymers with these ionic compounds results in composite materials with essential characteristics for applications in SSBs.

A polymer that exhibits these advantageous properties is PVA, mainly due to its favorable characteristics, such as high viscosity, nontoxicity, and an amorphous structure, in addition to its chemical, thermal, and mechanical stability [29]. Moreover, its water solubility contributes to its user-friendly nature, making it easier to handle [30]. Consequently, PVA is used in combination with a lot of materials, including ceramics, polymers, salts, and fibers, producing copolymers, blends, and composites that progressively enhance specific properties [31].

Despite prior knowledge of some PVA properties, some concerns need to be considered. Even though the 2D mer structure is known, many studies on PVA often overlook methods to determine crystallinity in experimental powder X-ray diffraction analysis [30, 32, 33]. This omission is possibly due to the fact that polymers typically exhibit broad peaks, resulting in overlapping peaks from different crystalline planes, which complicates analysis and leads, for example, to theoretical analyses based on predefined structures rather than experimental data. Additionally, it is worth noting that only a few articles have specifically investigated the detailed electrical properties using both the Equivalent Circuit Model (ECM) and the Jonscher model, as well as electrical modulus parameters of PVA-based polymer electrolytes complexed with lithium salts [34, 35]. In fact, ECM method is quite used, but the connection with other physical models to confirm the results are scarce in the literature [32].

#### **General objective:**

To investigate the influence of ionic salt concentrations of  $\text{LiOH}$  and  $\text{LiClO}_4$  in PVA-based membranes, exploring their conduction dynamics, dielectric behavior, and structural, thermal, and mechanical parameters, with the aim of evaluating their potential application as solid-state electrolytes.

#### **Specific objectives:**

- To synthesize PVA/ $\text{LiOH}$  and PVA/ $\text{LiClO}_4$  membranes by the Solvent Casting Method.

- To characterize the material using spectroscopic (FT-IR and Raman), XRD, SEM-Energy Dispersive X-ray Spectroscopy (EDS), TGA and DSC, DMA, and tensile testing techniques.
- To perform first-principles calculations based on DFT to investigate polymer-ion interactions, structural relaxation, and formation energy of the materials.
- To analyze ionic behavior transport properties through Complex Impedance Spectroscopy using Equivalent Circuit Modeling, the Havriliak–Negami function, and Jonscher’s law.

The structure of the thesis is organized as follows:

Chapter 2 is divided into several sections. Sections 2.1 and 2.2 provide a historical overview through the explanation of primary and secondary liquid batteries and a state-of-the-art discussion on the different types of batteries currently developed. Special attention is given to the importance of lithium-ions SSBs based on solid electrolytes and their potential applications in portable devices. Sections 2.3, 2.4, and 2.5 present a review of various polymer matrices and ionic salts, as well as the most commonly used synthesis methods. In Section 2.6 a comparative analysis is conducted, highlighting favorable and unfavorable properties for this application area, contrasting their effectiveness under different conditions, and assessing their feasibility. Also includes a brief review of the PVA structure, focusing on its backbone and unit cell. This section also discusses ion transport along the polymer chains and interactions between ions and the polymer matrix. This review lays the groundwork for understanding the selection of PVA as the primary matrix in the synthesis of polymer membranes using SCM.

Chapter 3 presents a discussion on the electrical components used in CIS. It distinguishes between real and adapted components, explains the governing equations, and analyzes Cole–Cole plots based on Ohm’s generalized law within the complex impedance formalism. Theoretical models and methodologies commonly employed to simulate and calculate the physical properties of solid electrolytes are also discussed.

Chapters 4 and 5 focus on the methodology and results. These chapters detail the preparation of polymer membranes and the characterization studies performed. Experimental investigations address the influence of LiOH and LiClO<sub>4</sub> ions on PVA within PVA/LiOH and PVA/LiClO<sub>4</sub> membranes. The properties of these membranes were comprehensively examined using several techniques. FT-IR was employed to evalu-

ate the influence of  $\text{Li}^+$  ions on the vibrational modes of the polymer's polar groups. XRD analysis was used to verify ion dissociation and assess the impact of salts on the crystallinity, with crystallinity calculated using Rietveld refinement. TGA and DSC were applied to determine thermal properties such as glass transition temperature, melting point, and decomposition temperature, with the results compared to the XRD data for crystallinity. DMA and Strain-stress tests were conducted for mechanical studies. First-principles calculations based on DFT approaches were conducted to explore polymer-ion interactions. Finally, CIS was modeled using an ECM to acquire bulk resistance and the Jonscher model was applied to fit the conductivity spectra and Havriliak–Negami model was applied in Electrical Module peaks.

Chapter 6 presents the conclusions and discusses future perspectives from both experimental and theoretical viewpoints. Prior to the references, the scientific impact of this research are also included.

## **2 CONTEXTUALIZATION AND CONCEPTUAL FOUNDATIONS**

Human development has long been driven by the need to overcome basic challenges such as food preservation, disease treatment, transportation, safety, and shelter needs that have historically fueled research and innovation. One of the most critical demands is electricity, along with the vast array of devices that depend on it, making modern life inseparable from electronic technology. This reliance highlights key concerns regarding the efficiency, cost, capacity, safety, and sustainability of energy systems, prompting ongoing efforts to improve energy storage technologies, crucial factors for ensuring a reliable and sustainable energy supply.

To address the context of energy storage systems, mainly batteries, terms like batteries, electrodes, and electrolytes have undergone a continuous process of conceptual evolution aimed at clarifying their functions and applications.

In the next sections of this chapter, we will seek to address the basic definitions with focus in electrolytes, beginning with an analysis of the historical context, followed by the evolution of the types of batteries developed and introduced into the industrial market over the past decades. We will then explore the materials that have been and continue to be used in the manufacturing of these batteries, adopting an approach grounded in conceptual definitions and future perspectives.

### **2.1 Primary and Secondary Liquid Batteries and the Technological Advancement of Solid-State Batteries.**

Although empirical investigations and observations date back to classical antiquity, significant development of electrical concepts occurred between the 17th and 19th centuries. Renowned scientists such as Benjamin Franklin, Luigi Galvani, André-Marie

Ampère, Georg Simon Ohm, and Alessandro Volta contributed to this progress, fostering the scientific method and systematic observation.

Alessandro Volta (1745–1827), an Italian physicist, is best known for discovering the electric cell, later called the “Voltaic Pile” [36]. He demonstrated that stacking discs of silver and zinc separated by paper soaked in salt water generated electricity, with silver producing positive and zinc negative charges. This arrangement constituted the first battery model in 1800 [1, 36].



Figure 2.1: Representation of Voltaic Pile [1].

Thirty-six years later, John Frederic Daniell developed the Daniell Cell to address problems in Volta’s cell, such as electrode corrosion and polarization caused by hydrogen bubbles [37]. To overcome these issues, he introduced copper sulfate and zinc sulfate solutions as electrolytes, a term formalized by Svante Arrhenius in 1887 [38] which enhanced current generation and electrode durability. Around the same period, key concepts such as electrode, cathode, and anode were introduced by Michael Faraday in 1834 [39]. As a result, Daniell cells became widely used in 19th-century telegraphy [37].

Other battery models emerged to mitigate polarization effects, including the Grove cell (1839) with hydrogen and oxygen electrodes, the Leclanché cell (1866) composed of zinc and manganese dioxide—important for portable batteries—and the Clark cell (1881), a zinc-silver dioxide device used as a stable reference potential. Likewise, the zinc-carbon cell, employing zinc as anode and manganese dioxide as cathode, also played a significant role [37, 40, 41].

By the 1950s, alkaline cells further advanced battery technology through the use of powdered zinc anodes, manganese dioxide cathodes, and potassium hydroxide (KOH) electrolytes, thereby enhancing capacity and lifespan [42]. Later, metallic lithium anodes appeared in lithium-manganese batteries, offering high energy density (200 Wh/kg) and long life, although at higher cost and with limitations at very high temperatures [43, 37].

These are classified as primary batteries due to their disposable nature, in contrast to rechargeable secondary batteries.

The origin of secondary batteries dates back to the lead-acid batteries (LABs) invented by Gaston Planté in 1860. These batteries employ a metallic lead anode and a  $\text{PbO}_2$  cathode, with a diluted sulfuric acid ( $\text{H}_2\text{SO}_4$ ) electrolyte [44, 45]. To prevent direct contact between plates while allowing ion transport, Planté used a cotton mesh with porous structure. LABs are rechargeable because lead sulfate forms on both electrodes during discharge, releasing energy, and reverses during charging [37].

Between 1970 and 1980, sealed valve LABs were widely used in electric vehicles despite drawbacks such as high density, limited cycle life, and the “memory effect,” in which partial recharging occurred without full discharge. Nickel-Cadmium (NiCd) batteries, developed earlier but mass-produced in the 1970s, improved upon LABs by incorporating nickel to increase storage capacity and reduce the cadmium memory effect [46, 37]. In 1989, the Nickel-Metal Hydride (NiMH) battery emerged as a more eco-friendly alternative by replacing cadmium with hydrogen-based alloys [46, 2]. Both NiCd and NiMH batteries employ potassium hydroxide (KOH) electrolytes and polymer separators, which facilitate ionic conduction without directly participating in the electrochemical reactions [46].

The major breakthroughs in batteries came with the invention of lithium cobalt oxide  $\text{LiCoO}_2$  cathodes in 1980 and the demonstration of lithium’s electrochemical reversibility in graphene in 1982 by John Goodenough and Rachid Yamazaki [47]. These innovations offered high storage density and nominal voltages around 3.6 V, three times higher than Ni-based batteries [48]. Lithium’s high electrochemical potential enabled lightweight, compact devices and advanced clean energy technologies, particularly electric vehicles. Sony began mass-producing lithium-ion batteries in 1991 [47, 48, 49].

Primary and secondary batteries are mass-produced for different applications,



Parameter	Battery Type	Acid-Lead	NiCd	NiMH	Li
Voltage / cell (nom.)		2	1.2	1.2	3.6
Density of energy		High	Low	Medium	High
Fast charge / discharge		No	Yes	Yes	Yes
Operating temperature		-20÷40 °C	-40÷60 °C	-20÷60 °C	-30÷60 °C
Internal resistance		Low	High	Medium	Low
Memory		No	Yes	No	No
Lifetime (cycles)		1,000	>3,000	>3,000	>1,000
Cost		Medium	Low	Medium	High

Figure 2.2: Comparison of Acid-Lead, NiCd, NiMH, and Lithium secondary batteries [2].

with both types typically relying on liquid electrolytes. Primary batteries serve low-maintenance devices, such as alkaline batteries for remotes and lithium-metal batteries for watches, whereas secondary batteries (e.g., LABs) are used to power vehicles. NiCd batteries remain in use for power tools, while NiMH and lithium-ion batteries (LiBs) dominate the portable electronics sector [50].

Although LiBs with liquid or gel electrolytes dominate consumer electronics and electric vehicles including phones, notebooks, and EVs, their liquid electrolytes present significant safety risks, such as leakage, overheating, and thermal runaway. These issues typically occur at the electrode/electrolyte interfaces and can lead to fires or explosions, as illustrated in Figure 2.3 [3]. Despite these concerns, liquid electrolytes still accounted for approximately 50–55% of the market in 2024. However, gel electrolytes have gained traction, representing a 42.3% revenue growth due to improved safety performance. Meanwhile, solid electrolytes currently hold a smaller market share (2–5%) but are attracting increasing attention because of their potential to significantly enhance both performance and safety [51].

Solid-state batteries, investigated since the 1970s, aim to replace conventional liquid electrolytes with solid ionic conductors and have made substantial progress in response to the growing demand for cleaner and safer energy storage solutions [52]. Instead of relying on liquid electrolytes, SSBs are generally classified into four main categories: polymer-based, metal–organic frameworks (MOFs), ceramic-based, and organic–inorganic composite electrolytes [53].

Polymer-based electrolytes with ionic additives exhibit ionic conductivities ranging from  $10^{-8}$  to  $10^{-5}$  S/cm, and offer advantages such as high flexibility, low inter-

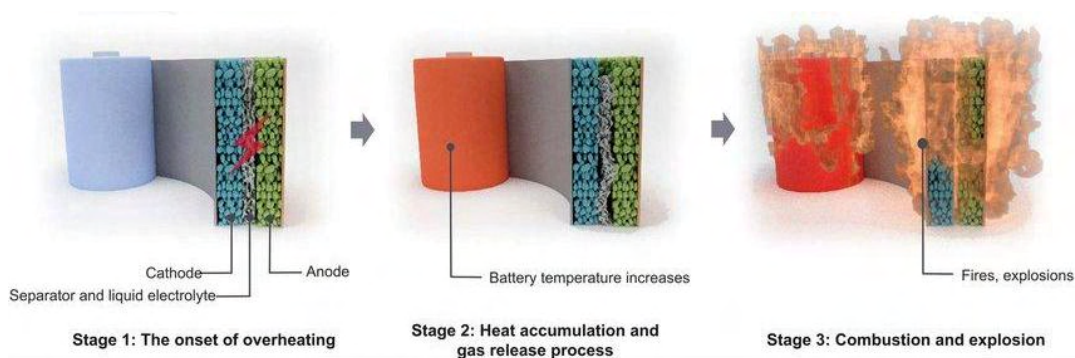


Figure 2.3: Stages of fires and explosions in liquid batteries due to overcharging, high currents, or internal shorts [3].

facial impedance, scalable fabrication, and improved safety. Inorganic electrolytes including perovskite, garnet, NASICON-type oxides, sulfides, and halides reach higher conductivities ( $10^{-5}$  to  $10^{-3}$  S/cm) and are widely studied for their chemical stability, mechanical strength, and compatibility with lithium metal [54, 55, 56, 57, 58, 59]. MOFs, show moderate conductivity ( $10^{-7}$  to  $10^{-5}$  S/cm) and good mechanical properties [60]. Organic–inorganic composites ( $10^{-7}$  to  $10^{-4}$  S/cm ) combine the strengths of both phases, offering improved mechanical performance and interfacial stability [61].

SSB materials are a key focus in next-generation battery research due to their safety, stability, and compatibility with lithium metal. While they offer advantages over liquid electrolytes, such as eliminating leakage and flammability risks, they still face challenges, including lower ionic conductivity at room temperature, high interfacial resistance, and processing difficulties. Nevertheless, their potential continues to drive intensive research as a promising route toward safer and more efficient energy storage.

## 2.2 State of the Art

From the historical context, we can summarize that the batteries have components that are made up of: electrode (cathode and anode), separator (which prevents short circuits), and the electrolyte. Electrolytes can be liquid, solid, or semi-solid in a gel/solid state. The ions move from the cathode to the anode during charging, and the opposite happens during discharging, as shown in Figure 2.4.

It can be asserted that the electrolyte is a crucial component, as it facilitates the chemical charge/discharge process through the migration of ions within it. Therefore,

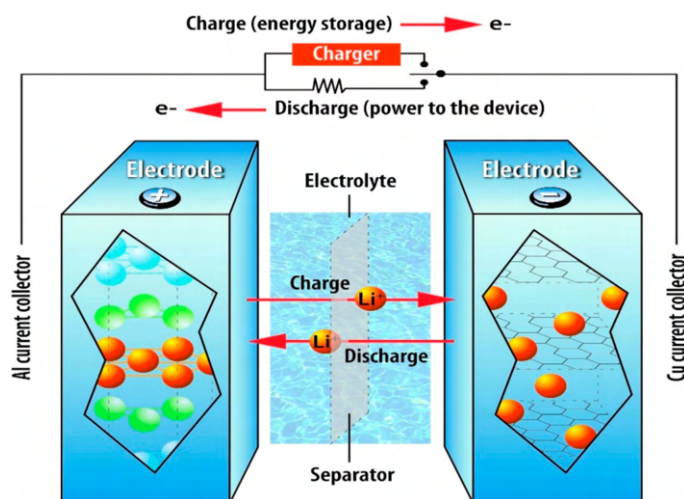


Figure 2.4: Battery model based on solid ion-lithium electrolyte. Components: electrodes, separator, and electrolyte [4].

it must possess the necessary properties to ensure the proper functioning of a battery. The following characteristics are particularly important:

- Good ionic conductivity.
- Inert with respect to the other components of the battery cell.
- Mechanical and thermal stability.
- Low volatility and flammability.
- Environmentally friendly.

The classification of electrolytes in SSBs is extensive and involves a detailed analysis, which can consider inorganic, organic, and composite materials derived from them. In line with the objective of this research, the following sections will detail the main materials used as electrolytes in SSBs, with a focus on polymer composites, taking into account the primary synthesis methods, matrix polymers, additive materials, and solvents.

## 2.3 Polymer Electrolytes

By definition, polymers capable of forming membranes and possessing ion-conducting properties, which can be used as electrolytes in batteries, are referred to

as electrolyte polymers. PEs are considered promising alternatives in SSBs due to their significant advantage of being safer than liquid electrolytes.

It is important to highlight that not all of these materials can form membranes or thin films, as this behavior depends on factors such as molecular weight ( $M_w$ ) and crystallinity [62]. The degree of polymerization, which refers to the number of repeating units (mers) linked to form the chain and consequently the associated average  $M_w$  that can vary considerably [63, 64]. When the  $M_w$  is below 20,000 g/mol, the resulting materials typically exhibit low mechanical strength and thermal stability, making them unsuitable for most membrane applications. In contrast,  $M_w$  values above 100,000 g/mol lead to longer and more entangled chains, which hinder solubility and processing. Therefore, although exceptions exist, the intermediate  $M_w$  range between 20,000 g/mol and 100,000 g/mol is considered ideal, as it provides a balance between flexibility and rigidity [5].



Figure 2.5: Amorphous and crystallite portions of polymer morphology and crystallinity [5].

The organization of polymer chains is also an essential factor to be considered. In general, all polymers exhibit regions of disordered and ordered molecular arrangement, known as amorphous and crystalline structures, respectively. The percentage of each of these regions in a sample is referred to as the degree of crystallinity. A polymer is considered amorphous when its crystallinity is below 30%–35%, and it is considered semi-crystalline when the crystallinity exceeds that value. It is worth noting that this percentage may vary for the same polymer, depending on its solubility, the synthesis method used, or the additives introduced [5].

For example, polyethylene—including High-Density Polyethylene (HDPE) and Polytetrafluoroethylene (PTFE)—is not capable of forming flexible membranes due

to its molecular weight range, which varies from 100,000 g/mol to 1,000,000 g/mol, and its crystallinity above 60%, characteristics that make the material rigid and unsuitable for use in polymeric solutions [65, 66]. These structural properties compromise the flexibility and adaptability of polyethylene, limiting its application in systems that require greater flexibility and conformability, such as PEs for SSBs.

Next, we present the classification of the types of PEs and how they are analyzed from different perspectives. They can be based on:

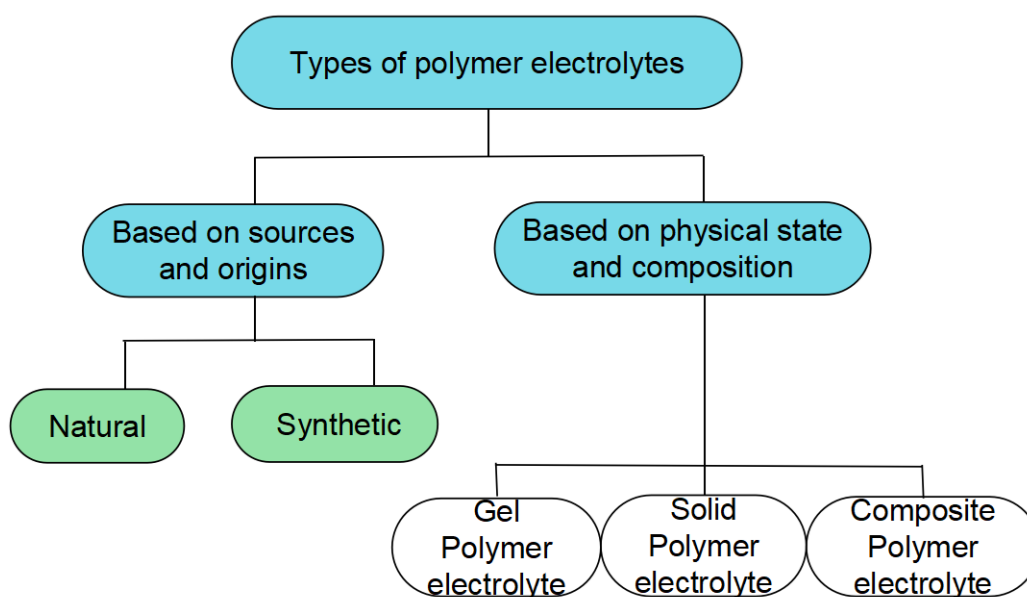


Figure 2.6: Classification of polymer electrolytes. Source: Author.

- Sources and Origins:

**Natural:** These polymers are found in nature, derived from plants or living organisms through natural processes. Cellulose, for instance, is the most abundant natural polymer, obtained from plant cell walls. Chitosan comes from the exoskeleton of marine animals, while rice and corn starch are also representative examples [67].

**Synthetic:** They do not occur naturally and are artificially produced through chemical processes known as polymerization. During synthesis, properties such as the average molecular weight distribution, chain structure (whether linear, branched, or crosslinked), degree of crystallinity, transition temperatures, and density are taken into account. Examples include polyethylene (PEO), polypropylene (PP), polyamides, fluorinated polymers, and others [67, 68].

\* Although not part of the traditional classification, the class of biopolymers is important for understanding PEs, as it includes both natural and synthetic polymers designed for environmentally friendly applications. In contexts where sustainability matters, these are valued for their biodegradability or biocompatibility [69]. Polylactic acid (PLA) is an example of a natural biopolymer derived from corn starch, while the synthetic polymer PVA is also classified as such due to its water solubility.

- Physical State and Composition:

- Gel Polymer Electrolytes (GPEs) are composed of polymer matrices that are swollen or immersed in liquid electrolytes. Among them, Polyethylene Glycol (PEG) is widely employed, typically in combination with lithium chloride and the addition of plasticizers. This composition classifies it as a GPE [68].

- Solid Polymer Electrolytes (SPEs) exhibit relative rigidity due to interactions between the mer units within their polymer chains. They also contain a low proportion of solvent, as observed in materials based on PEO, polyvinylidene fluoride (PVDF), and polymethyl methacrylate (PMMA) [68].

- Polymer Composites (CPEs) may include different polymer matrices (blends), variations in their mere composition (copolymers), and the incorporation of salts, fibers, nanomaterials, fillers, or other reinforcing materials with desirable properties into the main matrix [68, 70].

In addition to the general classification discussed in the previous paragraphs, another important classification within the scope of PEs can be added below.

- \* Host polymers: These are included in both synthetic classifications and within GPEs, SPEs, and CPEs. Host polymers contain reactive functional groups in the structure of their mere units, acting as a base matrix for the addition of other materials. Although polymers such as PP (-CH<sub>2</sub>-CH(CH<sub>3</sub>)-) and PE (-CH<sub>2</sub>-CH<sub>2</sub>-) are synthetically produced, they do not fit into this classification because they lack reactive groups in their side chains. [68].

Polymers that contain ether (-O-), amide (-CONH-), carboxylate (-COO-), alcohol (-OH-), imide (-C(O)N-), sulfate (-SO<sub>3</sub>H), phosphate PO<sub>4</sub><sup>2-</sup>, nitrogen (-NH<sub>2</sub>), fluoride, and cyclic ring groups have the ability to act as host polymers, facilitating the dissociation of reinforcing materials. Figure 2.7 shows

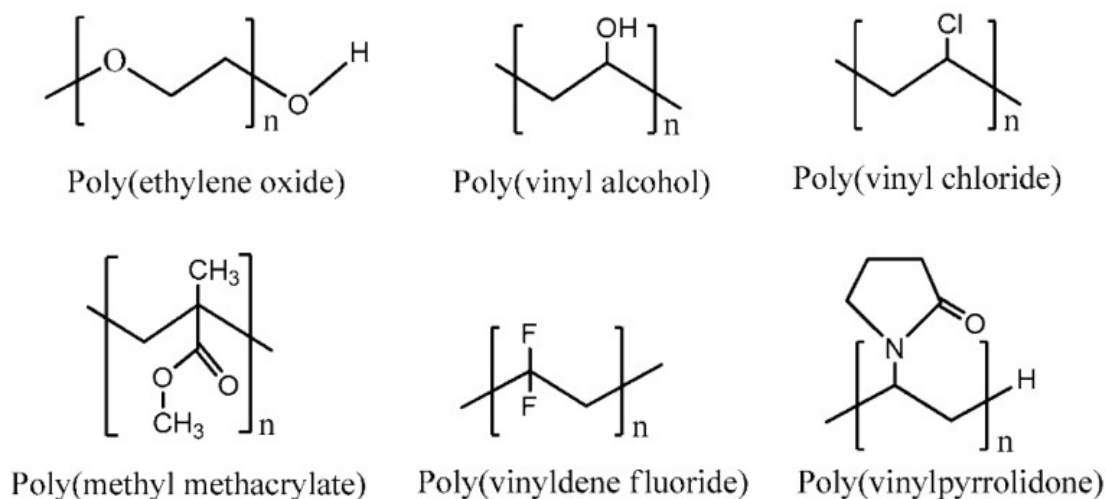


Figure 2.7: Most used Polymer Hosts in polymeric membranes. The side molecular groups help to form the GPEs, SPEs and CPEs dissociating additive materials [6].

the structure of some host polymers, including the aforementioned PEO, PVA, PVDF, polyvinylidene chloride (PVC), PMMA, PVDF, and polyvinylpyrrolidone (PVP).

## 2.4 Synthesis method of PEs

The synthesis of membranes for solid polymer electrolytes constitutes a critical procedure in the development and optimization of these materials, particularly in energy storage systems. The efficiency and stability of solid electrolytes depend on the quality and functional characteristics of the membranes, which must effectively conduct ions while preserving structural integrity. The following outlines three principal techniques implemented in their fabrication, each presenting distinct advantages and challenges.

- Solvent Casting Method (SCM):

It is commonly the most widely used method for this type of material, primarily due to its simplicity, practicality, low cost, dimensional control, versatility with respect to the polymers used, and membrane flexibility. The procedure begins with ensuring the homogeneity of the dissolution of the host polymer in a compatible solvent, while regulating stirring frequency and duration. Subsequently, the reinforcing material is incorporated while maintaining the homogeneity of the solution. The resulting solution

or gel is then cast onto Petri dishes and placed in a vacuum oven, with temperature and evaporation time carefully controlled to produce the thin film or polymeric membrane [6].

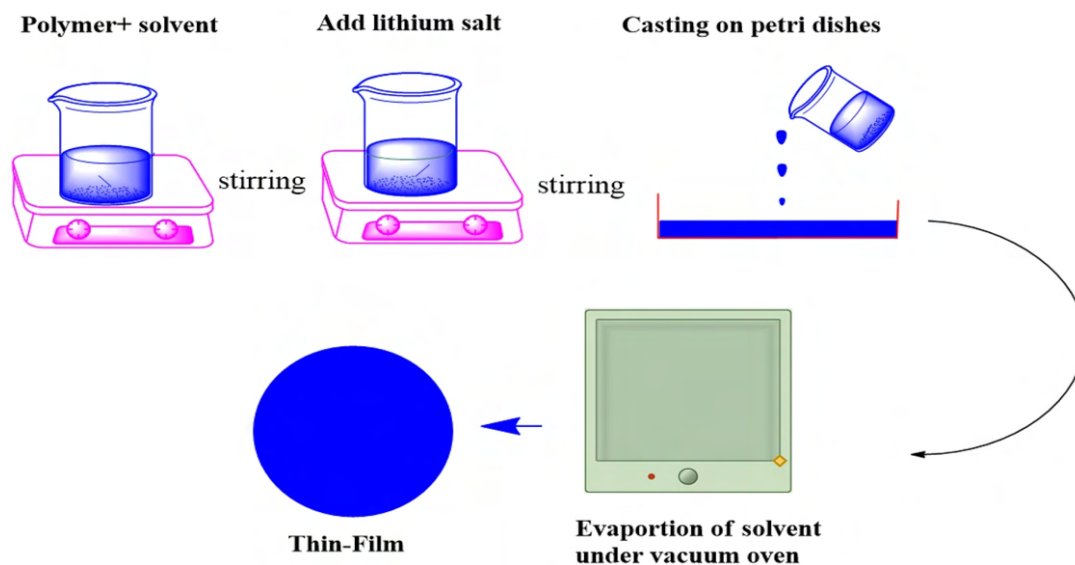


Figure 2.8: SCM synthesis method steps [6].

Factors such as the polymer's Mw and solubility in the chosen solvent, as well as the solvent's quantity and volatility (particularly for organic solvents), must be carefully considered. Furthermore, challenges related to microstructure control, membrane uniformity, and limitations in scaling up the process should also be taken into account [71].

- **Electrospinning:**

Unlike the SCM method, the electrospinning technique employs an apparatus composed of at least four predefined components: a syringe containing the polymer solution; the spinneret, which is attached to the syringe and where fiber formation occurs during electrospinning; a collector screen onto which the fibers are directed for membrane deposition; and a high-voltage source that generates the electric field between the spinneret and the collector screen.

The following images provide vertical and horizontal representations of the method. The Taylor cone phenomenon is also illustrated, which occurs when the solution is drawn during the electrospinning process and assumes a conical shape.

The solution density, the distance between the needle and the collector, and the power supply voltage are parameters that must be predefined, as they directly affect



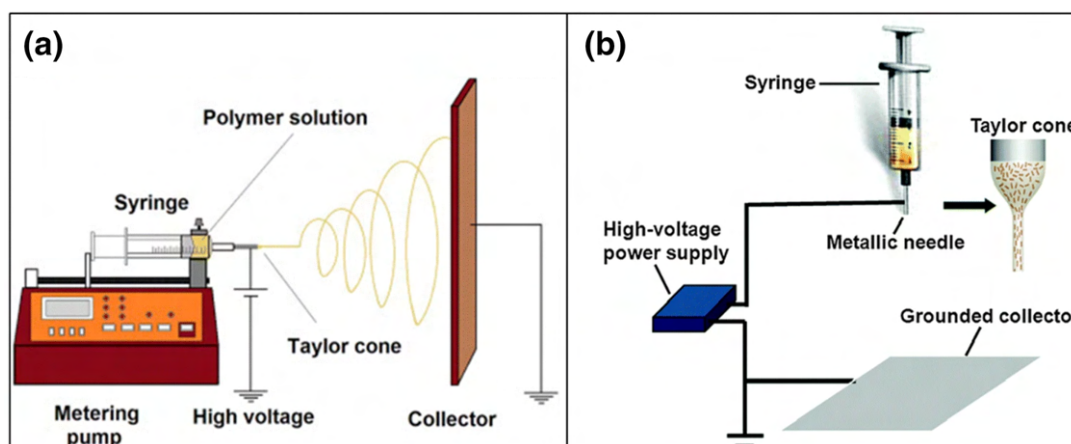


Figure 2.9: Setup and method of the Electrospinning synthesis [7].

the final membrane. Different types of spinnerets and collectors can also be used depending on the intended design, influencing the distribution, diameter, and orientation of the fibers, and consequently, the properties of the membranes [72].

For scientific applications, electrospinning is promising due to its simplicity, accessibility, and low cost, while allowing precise control over fiber dimensions, thereby affecting the material's morphology. However, the technique also faces challenges in scalability, mechanical stability, and potential polymer degradation caused by the high applied voltage.

- Phase inversion:

This process involves the phase inversion of a liquid polymer solution, in which the polymer is transformed into a solid porous membrane. Several fabrication techniques rely on this method, including microfiltration, ultrafiltration, nanofiltration, reverse osmosis, pervaporation, gas separation, and membrane permeation. First, the polymer solution is prepared and spread onto a flat surface using a casting blade to control the sample dimensions. The material is then immersed in a coagulation bath, where solvent–nonsolvent exchange takes place. Finally, the membrane is washed to remove residual solvents and nonsolvents, followed by drying [73].

It is well established that most commercial porous membranes are produced by this method due to its simplicity, low cost, and the ability to control porosity. Nevertheless, its main drawbacks are the low mechanical strength of the membranes and their high sensitivity to process parameters.

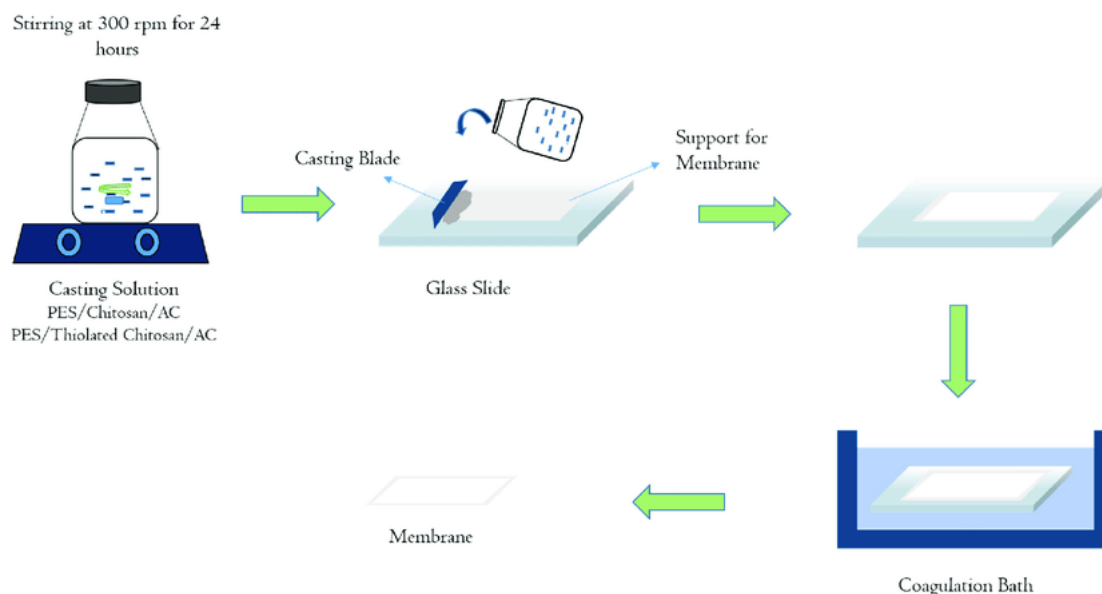


Figure 2.10: Illustration of phase inversion method [8].

The techniques mentioned are the most commonly employed in laboratory studies for the synthesis of both porous and non-porous membranes for PEs. These processes require precise control of synthesis parameters such as temperature, reaction time, and composition, as well as careful evaluation of membrane stability during production and operation. In addition to these conventional techniques, other relevant methods include sol–gel, drop-coating, freeze casting, in situ polymerization, and hot pressing, which provide flexibility for tailoring membranes to different types and performance requirements [74, 75, 76]. In parallel, large-scale industrial processes such as roll-to-roll and extrusion enable continuous and high-volume membrane production, which is essential for commercial manufacturing and applications in larger devices [77, 78].

## 2.5 Ionic Salts and transport mechanisms

The polymer must promote dissociation of the reinforcing material during solubilization. Since the host polymer is typically an insulator with covalently bonded chains, it cannot conduct electricity on its own. Therefore, incorporating ionically conductive salts is essential to enhance conductivity in LiBs [79]. As a result, polymer-based LiBs act as CPEs, combining membrane flexibility with ionic conduction from lithium ions.

To properly select the additive material to be used, certain parameters directly influence the ionic dynamics and compatibility with the matrix in solution. Ionic dy-

namics are generally compared based on ionic conductivity, molecular weight, ionic mobility, dissociation constant, and donor number. Figure 2.11, these properties are compared for ionic salts that are frequently used in polymer-based materials [3].

Lithium hexafluoroarsenate ( $\text{LiAsF}_6$ ) exhibits the highest ionic conductivity due to the less coordinated nature of its  $\text{AsF}_6^-$  anion compared to  $\text{PF}_6^-$  in  $\text{LiPF}_6$ , which promotes enhanced ionic dissociation [80]. However, its carcinogenic and neurotoxic effects, combined with its high corrosiveness in the presence of moisture, make it life-threatening and unsuitable for practical applications [81]. Alternatively, lithium tetrafluoroborate ( $\text{LiBF}_6$ ) and lithium trifluoromethanesulfonate ( $\text{LiTf}$ ) are less toxic and exhibit good ionic mobility, but they suffer from drawbacks such as lower conductivity, thermal instability, and higher cost [82, 83].

Among these salts,  $\text{LiPF}_6$  is the most widely used, both in liquid electrolytes and in studies involving polymer electrolytes. It provides high ionic conductivity, compatibility with a broad range of solvents, and good thermal stability under the typical operating conditions of electronic devices [84, 85]. In addition, it benefits from large-scale industrial production. Nevertheless, caution is required when handling  $\text{LiPF}_6$ , as it can decompose and release toxic HF gases at elevated temperatures.

Promising alternatives to  $\text{LiPF}_6$ , such as  $\text{LiClO}_4$  and lithium bis(trifluoromethanesulfonyl)imide ( $\text{LiTFSI}$ ), offer relatively high ionic conductivity, good ionic mobility, and favorable dissociation constants [86, 87].  $\text{LiClO}_4$  is advantageous due to its cost-effectiveness, ease of purification, and good solubility, although it is not as inexpensive as  $\text{LiPF}_6$ .  $\text{LiTFSI}$ , on the other hand, stands out for its superior thermal and chemical stability, being less reactive and presenting a lower risk of decomposition at elevated temperatures [88, 87]. Both salts exhibit lower reactivity compared to  $\text{LiPF}_6$ , providing greater safety and durability under various operating conditions, in addition to reducing the release of toxic byproducts [3].

Another lithium source employed in PEs is lithium hydroxide, which enhances ionic transport efficiency in polymer chains [89].  $\text{LiOH}$  also improves thermal and mechanical stability, as its dissociation generates light ions that contribute to these properties. Furthermore,  $\text{LiOH}$  is easy to prepare and shows low reactivity, making it an attractive option for polymer electrolyte applications.

In this context, polymers with a high affinity for metal-ion coordination typically contain side chains with oxygen-bearing functional groups. Oxygen, being an elec-

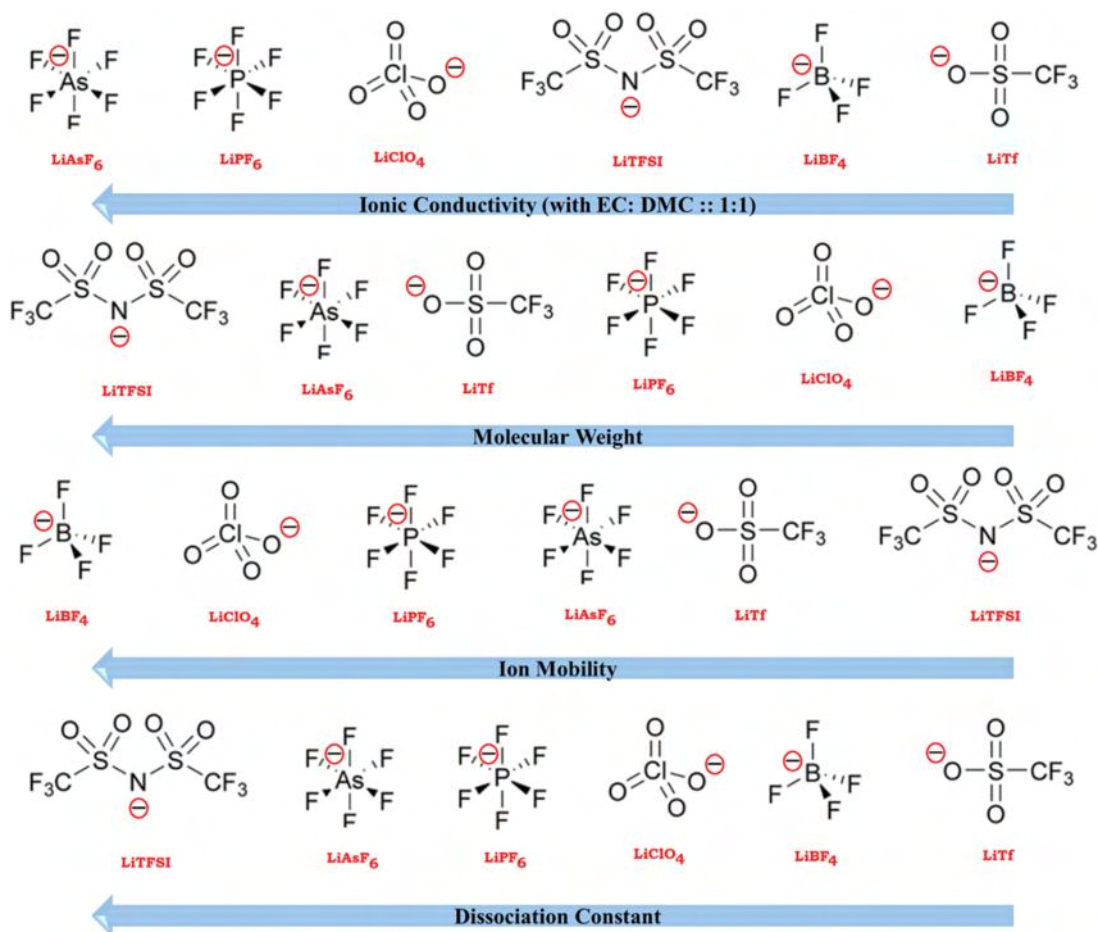


Figure 2.11: Comparison of different characteristics of lithium salt, adapted from [3].

tronegative atom, carries a partial negative charge, which enables it to attract atoms with partial positive charges. This polarity allows polymer segments to coordinate with metal cations from lithium salts, thereby facilitating ionic conduction [9].

In Figure 2.12, the left panel illustrates host polymer chains interacting with metal cations. The conformations of segments within the same chain (intrachain) enable cation conduction while maintaining flexibility during this interaction. Interactions between different chains (interchain) are also depicted, which may occur through hydrogen bonding or through direct coordination with the present ion [9, 90].

In the presence of organic or aqueous solvents, ionic complexes may form around the cation, initiating the solvation process. This occurs when solvent molecules interact with the ions, creating a solvation shell that surrounds the cation. Such an arrangement stabilizes the ions and facilitates ionic conduction. The resulting ionic complexes are referred to as “ion clusters,” which can vary in size and structure depending on the ion concentration and the nature of the solvent. This process affects ionic mobility and

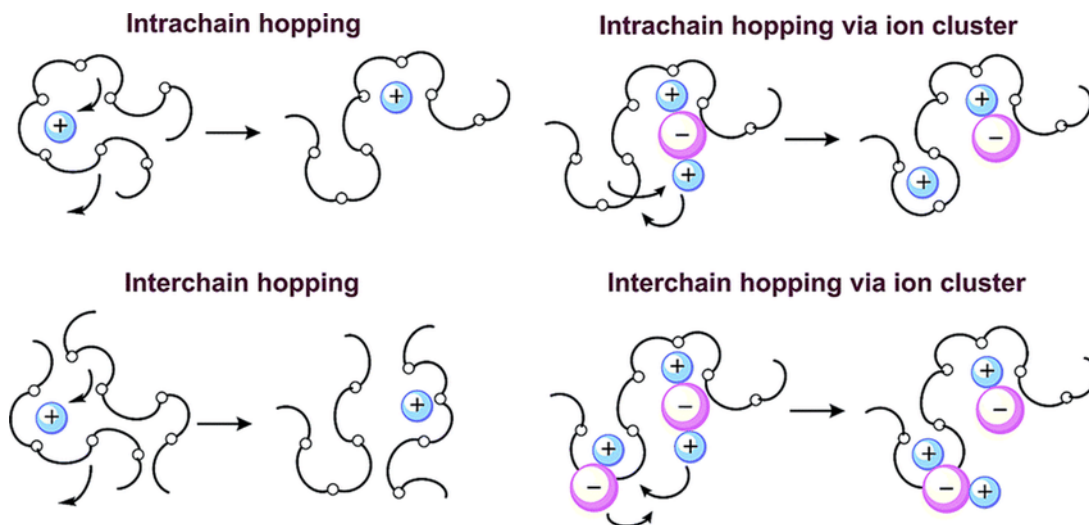


Figure 2.12: Interchain and Intrachain ion hopping and ion cluster hopping mechanisms in a Polymer Matrix [9].

conduction, as illustrated on the right side of Figure 2.12 [9].

## 2.6 PVA: structure, properties and composites

In this work, polyvinyl alcohol is employed as the host polymer, combined with the salts LiOH and LiClO<sub>4</sub> to form polymer composites. This section discusses the properties of PVA and reviews previous studies that have investigated these materials in composites with these and other additives.

PVA is a synthetic polymer widely used across various fields due to its versatility and favorable properties. It is considered an environmentally friendly polymer, as it is non-toxic and can be biodegraded by biological organisms, water, and organic solvents. This characteristic makes it a promising alternative to other synthetic polymers, which often present challenges for natural decomposition, resulting in long-term environmental impacts. Furthermore, PVA exhibits a remarkable ability to form malleable thin membranes and films, contributing to its widespread use in industrial applications due to its versatility and reliable performance under different conditions [4].

### 2.6.1 Molecular mer

Figure 2.13 presents a detailed representation of the PVA repeat unit (mer). The molecular formula of PVA is  $[\text{CH}_2\text{CH}(\text{OH})]_n$ , indicating that it is composed of re-

peating vinyl mer units, in which each ethylene unit (-CH<sub>2</sub>-CH<sub>2</sub>-) contains a hydroxyl group (-OH) on one of the side chains [10]. This structure provides PVA with unique properties, including high water solubility due to the hydroxyl groups and the ability to form strong, thin films.

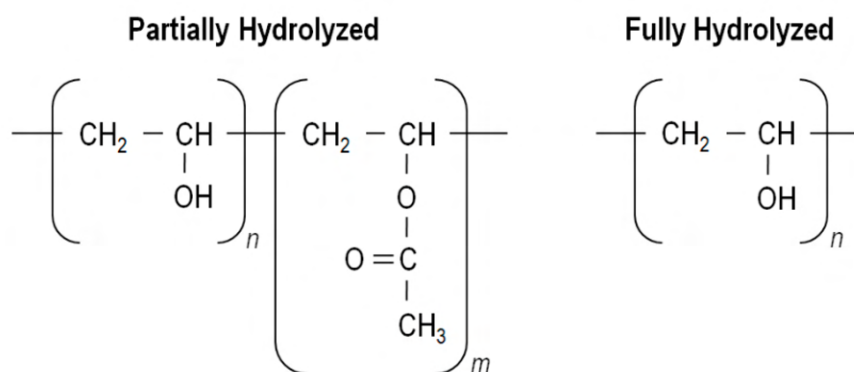


Figure 2.13: PVAs mer, n and m repetitions when partially hydrolyzed and pure mer for fully hydrolyzed [10].

## 2.6.2 Degree of Hydrolysis and its Effects on Mechanical Analysis

PVA is derived from polyvinyl acetate (PVAc) via hydrolysis using an alkaline catalyst, which may leave residual PVAc. When the degree of hydrolysis is between 87–90%, PVA is considered partially hydrolyzed, exhibiting moderate solubility and polymer chain arrangements influenced by the hydrolysis level. Highly hydrolyzed PVA (>98%) possesses higher purity and solubility but is less flexible and more sensitive to moisture. Intermediate degrees of hydrolysis display a balance of these properties. Table 2.2 also presents the acetyl group content in molar terms [15].

Table 2.1: Degree of hydrolysis for various commercial PVA grades along with the associated residual content PVAc[15].

Hydrolyzation grade	Degree of hydrolysis (mol%)	Residual acetyl groups (mol%)
Fully	98–99	0.6–1.5
Intermediate	93–97	2.7–6.9
Partially	85–90	10–15

The bonding between the mers is characterized by the degree of polymerization (DP) of the material. Since this value is not constant, the molecular weight is deter-

mined as an average. It is important to note that both DP and Mw can vary depending on the degree of hydrolysis, the preparation method, and other factors. Table 2.2 presents these values for four commercial PVA materials. In all cases, Mw falls within the ideal range for the production of membranes and thin films, although values up to 120,000 g/mol are also used in certain analyses [16].

Table 2.2: DP, Mn, and solution viscosity of four commercial grades of PVA [16].

<b>Grades</b>	<b>DP</b>	<b>Mw</b>	<b>Solution viscosity</b>
Low	550	22,000–27,000	4–7
Intermediate	900	35,000–40,000	13–18
Medium	1500	75,000–82,000	26–30
High	2200	89,000–100,000	48–65

The viscosity of the solution, presented in Table 2.2, reflects the PVA concentration in the solvent. Higher viscosity indicates greater PVA content, typically associated with increased Mw and DP.

The combination of Mw and degree of hydrolysis significantly influences the mechanical behavior of PVA membranes. Strain–stress tests reveal substantial variations in tensile strength and elongation, as both flexibility and mechanical stability are closely dependent on these parameters.

For PVA with a Mw above 50,000 g/mol, and considering different degrees of hydrolysis (low, intermediate, and high), tensile strength can range from 20 MPa to 50 MPa, reflecting the direct impact of Mw on membrane stiffness and strength [91]. Elongation can range from 100% to 400% [92]. Generally, a higher degree of hydrolysis results in a more rigid and less extensible membrane, particularly when Mw is also high. Membranes exhibiting mechanical properties within these ranges of elasticity and tensile strength are considered mechanically stable until failure.

### 2.6.3 Structure and Crystallinity

In 1935, Halle et al. [93] were the first to attempt identifying patterns in stretched PVA samples. They suggested that the periodic nature is approximately 2.50 Å [93]. In the same year, Perrin, M.W. et al. [94] sought to understand the ethylene and vinyl alcohol interpolymers, which were prepared by copolymerization followed by hydroly-

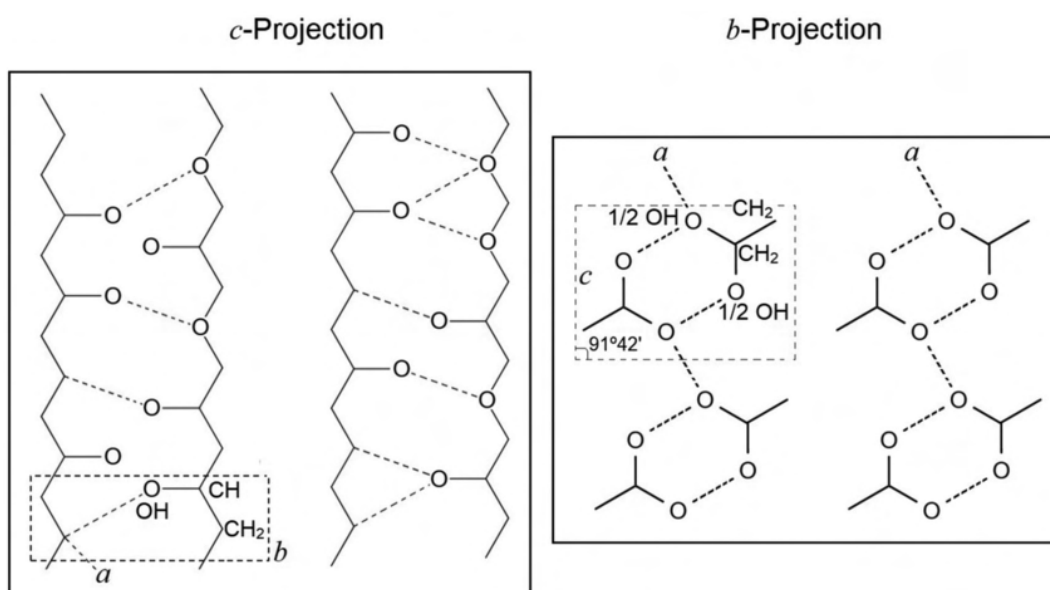


Figure 2.14: PVA structure by Brun et al. c and b projections [11].

ysis, and obtained the same repeating distance corresponding to zigzag chains of hydrocarbons. This indicates that the repetition of PVA monomers does not follow a defined pattern.

In 1947 and 1948, C.W. BRUNN and H.S. PEISER, based on X-ray diffraction photographs, considered that the hydroxyl groups could be placed randomly in the left and right positions of the backbone [95, 11]. The reflection patterns for two molecules followed structures of monoclinic units with the unit cell parameters:  $a = 7.81 \text{ \AA}$ ,  $b = 2.52 \text{ \AA}$ ,  $c = 5.51 \text{ \AA}$ , and  $\beta = 91.42^\circ$ , satisfying the  $P2_1/m$  symmetry with the following atomic positions: C (from CH<sub>2</sub>) at 0.190, 0.250, and 0.806, C (from CH) at 0.277, 0.750, and 0.708, half of the oxygen atoms at 0.451, 0.750, and 0.782, and the others oxygen atoms at 0.277, 0.750, and 0.450.

In Figure 2.14, the structure of PVA is projected in two directions, showing the unit cell, mers chains, and the possibility of hydrogen bonds through weak non-covalent interactions, occurring between the hydrogen contained in one polymer chain attracted to oxygen atoms of the adjacent molecule.

A fundamental property that can be obtained from XRD is the crystallinity of a specific material. In current studies, it is common to use curve fitting methods of the obtained diffractograms to determine the degree of crystallinity of a polymer. To do this, the set of crystalline peaks is compared with the 'non-crystalline peak', which refers to the background associated with the amorphism of the material [96].



The most frequently used adjustments are related to the deconvolution method, which employs Gaussian, Lorentzian, symmetric, and antisymmetric functions [97]. This method stands out for its effectiveness, as it can approach the expected results and also allows for the identification of other important parameters, such as the gull width at half maximum (FWHM) and the peak center [98]. It is worth noting that this approach is limited to the applied mathematical models and does not allow for direct identification of the peaks, especially when they are overlapped. What is typically done is a comparison with the literature to assign peaks close to each other in order to increase accuracy.

From the deconvolution analysis of the peaks, it was determined that the crystallinity of PVA ranges between 25% and 42% [97, 3, 99, 100, 101]. This range reflects the presence of varying degrees of structural order in the material, from amorphous to semicrystalline character.

Another relatively powerful method for precise data analysis, correct peak identification, and crystallinity calculation is Rietveld Refinement; however, this approach is mostly applied to crystalline materials with well-defined structures. Specialized software for this analysis includes FullProf, Material Analysis Using Diffraction (MAUD), and General Structure Analysis System (GSAS)[102, 103, 104]. These programs require input files such as the experimental Datafile, the Instrumental File containing information related to the diffraction instrument, and the Crystallographic Information File (CIF) containing the potential phase(s) of the material. CIFs can be obtained from databases such as the Inorganic Crystal Structure Database (ICSD), Cambridge Structural Database (CSD), and Crystallography Open Database (COD)[105, 106, 107]. Although ICSD and COD include organic compounds, many polymers lack CIFs, which limits the application of these programs for detailed polymer structure analysis.

Only recently, A. Lobo-Guerrero [33] analyzed PVA membranes (99%) with molecular weight 89,000–98,000 g/mol mixed in deionized water and immersed in citric acid to induce changes in crystallinity. The space groups  $P2_1/m$  and  $P2_1/c$  were tested, adapting the parameters considered by Brunn and creating a phase in the MAUD program. As a result, the model based on the  $P2_1/c$  space group satisfied the datafiles, instead of the original  $P2_1/m$ , and showed that crystallinity decreased with pH.

## 2.6.4 Thermal Stability

PVA exhibits favorable thermal properties that make it particularly suitable for the fabrication of PEs. One of its main advantages is the ability to be processed at relatively low temperatures, around 60 °C, which facilitates molding and the formation of membranes without requiring high-temperature treatment [108, 109]. This behavior is attributed to its glass transition temperature ( $T_g$ ), which occurs near 80 °C, allowing greater flexibility and ease of processing [110, 111]. Additionally, PVA demonstrates excellent thermal stability, with a decomposition temperature above 250 °C, ensuring material integrity even under elevated temperatures [111].

Thermogravimetric and differential scanning calorimetry analyses are essential for studying crystallinity in single-matrix polymers, as they allow measurement of enthalpy variations and, consequently, the degree of crystallinity. These results can be compared with XRD data, providing a more accurate and reliable assessment of the crystalline structure and thermal properties of the material.

## 2.6.5 Conductivity and composites with PVA matrix

Due to its lack of free charge carriers, PVA is an insulating, highly polar polymer whose hydroxyl groups form hydrogen bonds but do not enable efficient charge transport, resulting in conductivities between  $10^{-8}$  and  $10^{-12}$  S/cm, thus, it is typically used as a host matrix with ionic salts to obtain flexible, semiconductive membranes [112, 99, 113, 114].

With the addition of the lithium salts discussed in section 2.6, composites have already been made with  $\text{LiPF}_6$ ,  $\text{LiBF}_4$ ,  $\text{LiOH}$ ,  $\text{LiTFSI}$ ,  $\text{LiClO}_4$ ,  $\text{LiTf}$ , added to PVA. The corresponding ionic conductivity of each is presented in Table 2.3, as well as the combination of different polymers and these salts [85, 82, 89, 87, 86, 83].

By directly comparing the data in Table 2.3, it's evident that the addition of lithium salts increases the conductivity of PVA by at least four orders of magnitude, and, as expected,  $\text{LiPF}_6$  and  $\text{LiOH}$  provided the higher values, around  $10^{-4}$  S/cm.  $\text{LiPF}_6$  has a low activation energy, favoring its mobility, while  $\text{LiOH}$  has good solubility and ionic dissociation [85, 89].

Despite the improvement in the results, constructive criticisms should be made when comparing these materials:

Table 2.3: Conductivity and solvent systems of lithium-based polymer composites comprising either single-polymer matrices or dual-polymer blends.

Material	Conductivity (S/cm)	Solvent
PVA/ $LiPF_6$ [85]	$8.70 \times 10^{-3}$	DMSO
PVA/ $LiClO_4$ [86]	$4.00 \times 10^{-6}$	Water
PVA/LiTFSI [87]	$4.50 \times 10^{-5}$	DMSO
PVA/ $LiBF_4$ [82]	$8.90 \times 10^{-4}$	DMF
PVA/LiTf [83]	$4.57 \times 10^{-8}$	Water
PVA/LiOH [89]	$1.33 \times 10^{-3}$	Water
PEO/PVA/LiOH [32]	$1.25 \times 10^{-4}$	Water
PVA/PEG/LiOH [115]	$2.65 \times 10^{-5}$	Water
PVA/PMMA/ $LiBF_4$ [82]	$1.14 \times 10^{-5}$	DMF

Solvent: The dissociation of lithium salts in polymeric systems depends on the solvent's dielectric constant and its ability to dissolve both the salt and the host polymer. High-permittivity solvents such as water ( $\epsilon \approx 80$ ), DMSO ( $\epsilon \approx 46$ ), and DMF ( $\epsilon \approx 36$ ) are commonly used, as they enable efficient salt dissociation [116]. Additionally, these solvents are compatible with a variety of polymers, enabling strong interactions between the salt and the polymer matrix. Thus, selecting an appropriate solvent is essential to optimize polymer solubility and ionic dissociation.

Mw and Degree of Hydrolysis: Table 2.4 shows that several materials lack information regarding Mw and degree of hydrolysis. The absence of this data hinders direct comparison between materials, as these parameters directly influence the crystallinity and Mw of the composites. When provided, the variation in Mw is significant; for example, in the PVA/PEO/LiOH composite, the Mw of PVA is 60,000 g/mol, whereas in other composites, this value exceeds 85,000 g/mol. Furthermore, in the PVA/LiOH and PVA/ $LiClO_4$  membranes, both parameters are missing, which limits the possibility of a direct comparison between them.

Sample Dimensions: Another commonly missing piece of information is the membrane dimensions, such as area and thickness, which are essential for calculating the electrical properties of the materials. The absence of this information complicates performance comparison and analysis, compromising the reproducibility of experiments.

Table 2.4: Mw and Degree of Hydrolysis of PVA-based composites.

<b>Material</b>	<b>Molecular Weight</b>	<b>Degree of Hydrolysis</b>
PVA/ <i>LiPF</i> <sub>6</sub>	85,000–125,000	88%
PVA/ <i>LiClO</i> <sub>4</sub>	Not provided	Not provided
PVA/ <i>LiTFSI</i>	125,000	88%
PVA/ <i>LiBF</i> <sub>4</sub>	115,000	Not provided
PVA/ <i>LiTf</i>	Not provided	99%
PVA/ <i>LiOH</i>	Not provided	Not provided
PEO/PVA/ <i>LiOH</i>	60,000/700,000	Not provided
PVA/PEG/ <i>LiOH</i>	8,000/125,000	Not provided
PVA/PMMA/ <i>LiBF</i> <sub>4</sub>	115,000/120,000	Not provided

Therefore, specifying membrane dimensions is essential to ensure consistent and reliable results.

Studying PVA membranes with *LiOH* and *LiClO*<sub>4</sub> is essential for energy storage applications. However, many studies lack key analyses such as XRD, mechanical, thermal, and impedance spectroscopy, which are crucial for assessing structural, stability, and ionic transport properties. This omission limits the understanding and optimization of such materials for practical use.

Studying PVA membranes with *LiOH* and *LiClO*<sub>4</sub> is particularly relevant for energy storage applications. However, many studies lack key analyses, such as XRD, mechanical testing, thermal characterization, and impedance spectroscopy, which are crucial for assessing structural properties, stability, and ionic transport. This omission limits the understanding and optimization of these materials for practical applications.

## 3 THEORETICAL REVIEW

### 3.1 Impedance Fundamental Elements

The experimental procedure of complex impedance spectroscopy measurements generates a range of electrical data essential for understanding the studied material. Among these, the real and imaginary components of the impedance are particularly important, as they quantify the opposition to current flow when an electric field is applied. These quantities enable the investigation of conduction processes within the frequency range of the applied signal.

When a voltage  $V(t) = V_m \sin(\omega t)$ , with angular frequency  $\omega = 2\pi f$ , is applied to a material, the resulting current  $i(t) = I_m \sin(\omega t + \theta)$  is measured. The complex impedance  $Z^*(\omega)$ , expressed in ohms ( $\Omega$ ), depends on frequency and generalizes resistance by incorporating both magnitude and phase differences between voltage and current [117].

The general impedance equation is described by the equation 3.1, in cartesian coordinates and equation 3.2 in polar coordinates:

$$Z^* = Z' + iZ'' \quad (3.1)$$

$$Z^*(\omega) = \frac{V^*(\omega)}{I^*(\omega)} = |Z| \cdot \exp(i \cdot \varphi) \quad (3.2)$$

Here,  $i$  denotes the imaginary unit, and the phase difference represents the angle between the applied electric field and the resulting current. Equation 3.2 is derived from the generalized Ohm's law.

In practice, fitting in Cole–Cole plots ( $Z'$  vs  $Z''$ ) is often analyzed using parameters from equations that model electrical components, either as real circuit elements or as their mathematical representations. The interpretation of the studied material, as well

as the mathematical definitions associated with it, also originates from the generalized Ohm's law operating in the frequency domain.

In electrical circuit modeling, several fundamental components are commonly employed, as summarized in Table 3.1. The resistor, denoted by  $R$ , exhibits an impedance consisting solely of a real component, meaning that its impedance equals its resistance. The capacitor, represented by  $C$ , displays a purely imaginary impedance inversely proportional to frequency, where  $C$  denotes the capacitance. The inductor, symbolized by  $L$ , has an impedance directly proportional to frequency.

For elements that do not have direct analogues among standard electrical components, mathematical models are employed to accurately describe their behavior. The Constant Phase Element (CPE) is one such model, generalizing the capacitor to account for material inhomogeneities. Typically, an ideal capacitor is replaced by a CPE, characterized by two parameters: CPE-P, an exponent ranging from 0 to 1, and CPE-T, a coefficient that effectively replaces the capacitance  $C$ . When CPE-P equals 1, CPE-T corresponds exactly to the capacitance, thereby reducing the CPE to classical capacitive behavior [118, 119].

For elements that do not have direct analogues among standard electrical components, mathematical models are employed to accurately describe their behavior. The Constant Phase Element (CPE) is one such model, generalizing the capacitor to account for material inhomogeneities. Typically, an ideal capacitor is replaced by a CPE, characterized by two parameters: CPE-P, an exponent ranging from 0 to 1, and CPE-T, a coefficient that effectively replaces the capacitance  $C$ . When CPE-P equals 1, CPE-T corresponds exactly to the capacitance, thereby reducing the CPE to classical capacitive behavior [118, 119]. The exponent CPE-P is dimensionless, whereas CPE-T has units that formally depend on CPE-P, generally expressed as  $\Omega^{-1} \cdot s^{\text{CPE-P}}$ . In practice, however, publications commonly report only the numerical value of CPE-T without units, since the combination of CPE-T and CPE-P fully characterizes the element's behavior.

Table 3.1: Impedance equations of ideal and non-ideal electrical elements used in equivalent circuit modeling.

Component	Impedance Equation
Resistor ( $R$ )	$Z^* = Z' = R$
Capacitor ( $C$ )	$Z^* = Z'' = \frac{1}{i\omega C}$
Inductor ( $L$ )	$Z^* = Z'' = i\omega L$
Constant Phase Element (CPE)	$Z^* = \frac{1}{[T(i\omega)]^P}$
Finite Length Warburg ( $W$ )	$Z^* = R \cdot \frac{\coth((T\omega)^P)}{(T\omega)^P}$

Another important element in impedance modeling is the Finite Length Warburg element, denoted by  $W$ , which represents diffusion processes under open-circuit boundary conditions. This element exhibits both resistive and capacitive characteristics and is described by the parameters  $W$ - $R$ ,  $W$ - $T$ , and  $W$ - $P$ . Also known as the Generalized Finite Warburg (GFW), it is well established that when the parameter  $W$ - $P$  equals 0.5, the element produces a characteristic diagonal line in the Cole–Cole plot, indicative of diffusion-limited processes or electrode polarization [119].

It should be noted that other elements are also possible, such as distributed elements, extended distributed elements, and element followers. Likewise, if necessary, the equations of an element can be adjusted to better reflect the observed impedance behavior, provided that the modification maintains a valid physical-mathematical interpretation.

Figure 3.1 illustrating the previous equations, plots done using Zview Program [120]. Figure 3.1A) it is seen only one point which represents  $R$  component, it does not change with frequency. Figure 3.1B) and C) as similar because both have just complex components, and they correspond to and components, noting  $L$  is real. Figure 3.1D) is the CPE component showing a diagonal line, not necessarily with  $0.45^\circ$  angle. While Warburg generalized it all, by a diagonal line in high frequencies and semicircle in low frequency range, but it needs to keep an angle of  $45^\circ$ , see Figure 3.1E).

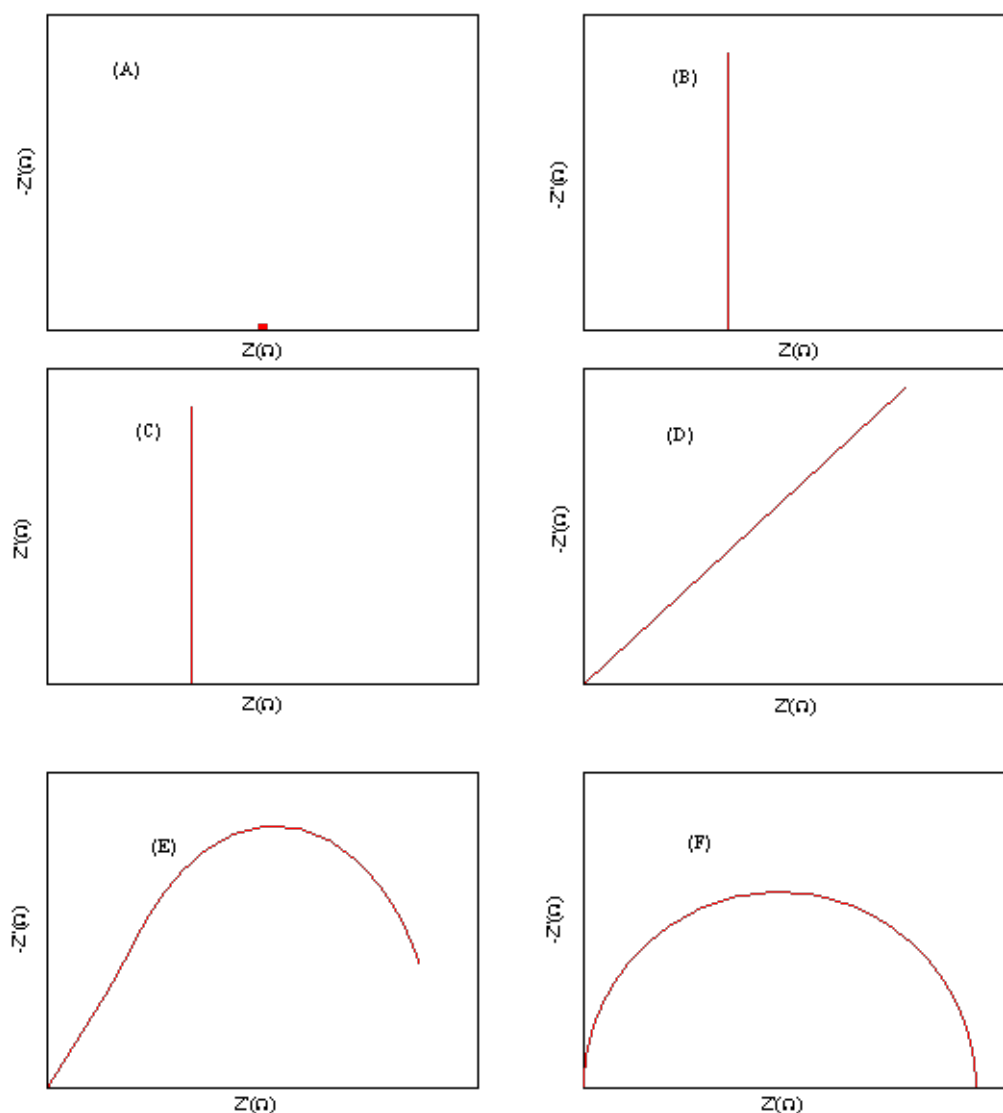


Figure 3.1: Impedance graphs of single and combined electric elements. They represent: A) Resistance, B) Capacitor, C) Inductor, D) CPE element, E) Finite Length Warburg and F) RC circuit.

Combinations between electrical components are also possible. Whether in series, parallel or mixed circuits. Figure 3.1F) we have the representation of a resistor combined with a capacitor, these connected in parallel, thus generating a semi-circle. The semicircle's diameter is proportional to the resistance, while its radius is inversely related to the capacitance. This behavior is typically seen in RC circuits and provides valuable insights into the electrochemical properties of the system.

As one might expect, analyzing the electrical behavior of materials—whether



metallic, ceramic, polymeric, or composite—is not straightforward. Even when an equivalent circuit is successfully fitted to the CIS data, this does not ensure the model’s correctness or uniqueness. Therefore, it is often necessary to interpret the material’s response within specific frequency regions to extract information aligned with the research goals. This approach helps identify conduction mechanisms and relate them to structural or intrinsic properties of the material [121].

In polymeric electrolyte applications, semicircles commonly appear across a wide frequency range—often complete or incomplete—and typically intersect the real axis, indicating the bulk ionic resistance  $R_B$  [3, 29, 30]. When reinforcing materials are introduced, variations in conductivity may arise, and equivalent circuit fitting becomes necessary to estimate  $\rho_{DC}$ . Doping and interfacial effects can further introduce additional conduction mechanisms at low frequencies, observed as extra semicircles or diagonal lines. These factors highlight the importance of fitting impedance data using appropriate models and non-ideal elements to reliably extract  $\rho_{DC}$ , capacitance, and conductivity. In this process, accurately determining  $R_B$ , CPE-T, and CPE-P is crucial for meaningful physical interpretation of the material’s electrical behavior.

### 3.1.1 Permittivity and Electric Modulus.

Upon application of an alternating electric field to the material, the dipolar entities do not respond instantaneously to the field oscillations. This results in a phase difference between the external field and the dipole reorientation, thereby inducing energy dissipation within the system.

$$\varepsilon_{\text{elec}}^* = \varepsilon'_{\text{elec}}(\omega) + i\varepsilon''_{\text{elec}}(\omega) \quad (3.3)$$

Where  $\varepsilon'_{\text{elec}}(\omega)$  is the real part and  $\varepsilon''_{\text{elec}}(\omega)$  is the imaginary part of the relative permittivity, representing the dielectric loss of the material. The complex permittivity  $\varepsilon_{\text{elec}}^*$  can be derived from the complex impedance  $Z^*$  using the following equations:

$$\varepsilon_{\text{elec}}^* = -\frac{Z^*}{\omega C} \left[ (Z')^2 + (Z'')^2 \right] \quad (3.4)$$

where  $C = \frac{\varepsilon_0 A}{l}$  is the capacitance of the sample,  $A$  is the area,  $l$  is the sample thickness, and  $\varepsilon_0$  is the vacuum permittivity, equal to  $8.854 \times 10^{-12}$  F/m.

The Debye model describes the behavior of permanent dipoles in a material under an alternating electric field. Polar molecules tend to align with the field, but this alignment is delayed due to rotational inertia and interactions with the medium, characterized by the Debye relaxation time. Consequently, the dielectric response depends on frequency: at low frequencies, dipoles follow the field oscillations and contribute significantly to permittivity; at high frequencies, their reorientation is too slow, reducing their effect. The Debye equation is given by [122].

$$\varepsilon'_{\text{elec}}(\omega) = \varepsilon_{\infty} + \frac{\varepsilon_s - \varepsilon_{\infty}}{1 + (\omega\tau)^2} \quad (3.5a)$$

$$\varepsilon''_{\text{elec}}(\omega) = \frac{(\varepsilon_s - \varepsilon_{\infty}) \omega\tau}{1 + (\omega\tau)^2} \quad (3.5b)$$

Where  $\varepsilon_s$  is the static permittivity at low frequencies,  $\varepsilon_{\infty}$  is the permittivity at high frequencies (when dipoles can no longer follow the electric field) and  $\tau$  is the Debye relaxation time.

Although the response of an RC circuit is mathematically equivalent to the solution described by the Debye model, only a limited number of real systems strictly conform to the Debye equations. To account for the deviations commonly observed in experimental spectra, several models have been proposed to describe the dielectric behavior of different materials [123]. Among the main extensions of the Debye model are the Cole–Cole and Davidson–Cole models, which modify only the denominator of the original expression to better fit real materials. The Cole–Cole model (1941) replaces the Debye term  $(1 + i\omega\tau)$  with  $(1 + (i\omega\tau)^\alpha)$ , introducing  $\alpha$  to account for symmetric broadening. The Davidson–Cole model (1951), in turn, uses  $(1 + i\omega\tau)^\beta$ , where  $\beta$  describes asymmetric broadening. In both cases, the parameters satisfy  $0 \leq \alpha, \beta \leq 1$ , improving agreement with experimental data [123].

Building upon these, the Havriliak–Negami model- HN (1966) generalizes both by incorporating the two parameters,  $\alpha$  and  $\beta$  simultaneously, which account for both symmetric and asymmetric broadening of the relaxation spectrum. This model is especially important because it provides greater flexibility in fitting experimental data from complex systems, such as polymers and complex mechanisms [124, 125]. HN equation model is given by:

$$\varepsilon^*_{\text{elec}}(\omega) = \varepsilon_{\infty} + \frac{\varepsilon_s - \varepsilon_{\infty}}{[1 + (i\omega\tau)^\alpha]^\beta} \quad (3.6)$$

The specific case of  $\alpha = 1$  and  $\beta = 1$  represents the Debye dispersion function. For  $\beta, \alpha \neq 1$ , it corresponds to the Cole-Cole model, and for  $\alpha = 1, \beta \neq 1$ , it corresponds to the Cole-Davidson model.

Besides permittivity, in certain situations specific quantities provide a more insightful representation of the electrical behavior of the material. One such quantity is the dielectric modulus  $M^*$ , which is defined as the inverse of the complex permittivity and is particularly useful for analyzing relaxation processes.  $M^*$  is written as:

$$M_{\text{elec}}^* = \frac{1}{\epsilon_{\text{elec}}^*} \quad (3.7)$$

And, using Eq. 3.4, we have:

$$M_{\text{elec}}^* = \frac{\epsilon_{\text{elec}}^*}{(\epsilon'_{\text{elec}})^2 + (\epsilon''_{\text{elec}})^2} \quad (3.8)$$

Since  $M_{\text{elec}}^*$  is a complex quantity, its real part  $M'_{\text{elec}}$  is associated with the inverse of the dielectric's ability to store electrical energy, while  $M''_{\text{elec}}$  corresponds to the inverse of the energy dissipation.

Table 3.2: Comprehensive matrix illustrating the mathematical relationships between the complex electrical formalisms  $M_{\text{elec}}^*$  (modulus),  $Z^*$  (impedance),  $Y^*$  (admittance), and  $\epsilon_{\text{elec}}^*$  (permittivity), commonly used in CIS [17].

	$M^*$	$Z^*$	$Y^*$	$\epsilon^*$
$M^*$	$M^*$	$\mu Z^*$	$\mu/Y^*$	$1/\epsilon^*$
$Z^*$	$M^*/\mu$	$Z^*$	$1/Y^*$	$1/\mu\epsilon^*$
$Y^*$	$\mu/M^*$	$1/Z^*$	$Y^*$	$\mu\epsilon^*$
$\epsilon^*$	$1/M^*$	$1/\mu Z^*$	$Y^*/\mu$	$\epsilon^*$

In complex impedance spectroscopy, the dielectric modulus formalism improves the resolution of relaxation phenomena, particularly in materials exhibiting high capacitance or significant electrode polarization. Unlike permittivity or impedance plots, which may mask bulk material responses, the modulus representation highlights distinct features such as well-defined peaks, thereby facilitating a more precise analysis

of relaxation processes.

Table 3.2 illustrate a resume of formalisms derivated from impedance, in which  $Y^*$  denotes an alternative formalism, the admittance, although less commonly used in this research field [17].

## 3.2 Conductivity Spectra and Jonscher Model

The analysis of the conductivity spectrum provides a powerful tool for investigating the electrical properties of materials, enabling the separation of distinct physical processes based on frequency, such as ionic conduction, polarization effects, and interfacial phenomena. This approach allows for the identification of underlying transport mechanisms, including ion migration and hopping processes, in addition to enabling the accurate determination of both the AC and DC components of conductivity. This analysis is essential for understanding and improving the performance of PEs.

The conductivity equation is given by:

$$\sigma_{\text{elec}}^* = \frac{l}{A} \times \frac{Z^*}{(Z'^2 + Z''^2)} \quad (3.9)$$

$$\sigma_{\text{elec}}^*(\omega) = \sigma'_{\text{elec}}(\omega) + i\sigma''_{\text{elec}}(\omega) \quad (3.10)$$

Where  $l$  is the thickness of the membrane and  $A$  refers to the effective area and conductivity  $\sigma'_{\text{elec}}$  (real) and  $\sigma''_{\text{elec}}$  (imaginary), see equation 3.9. The area is mostly circular, particularly in laboratory experiments, where membranes are molded into discs to facilitate handling .

A general plot of conductivity versus frequency is shown in Figure 3.2. It can be described as follows: at low frequencies, electrode polarization is observed, where the system's response is limited by the interface resistance between the electrode and the material. This is followed by the DC plateau, which may occur at both low and intermediate frequencies, reflecting the conductivity associated with direct current. Finally, at high frequencies, the conductivity exhibits dispersion, which is related to the material's response to rapid changes in the electric field. This effect is more pronounced in disordered or amorphous materials.

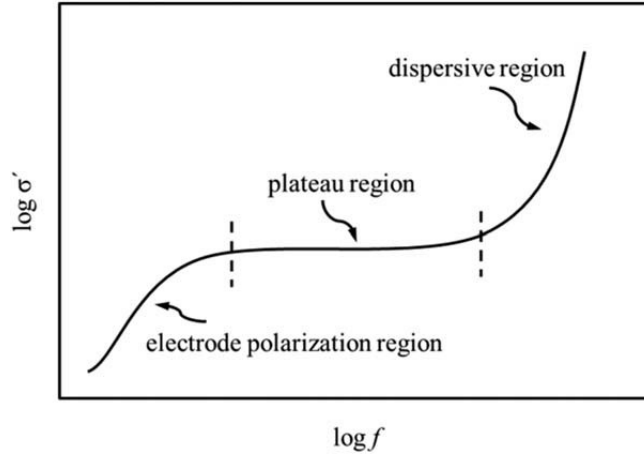


Figure 3.2: Representative log–log plot of  $\sigma'_{\text{elec}}$ , as a function of frequency at constant temperature, illustrating the typical behavior of disordered conductive materials. [12].

The conductivity behavior at low and high frequencies is modeled by Jonscher's Power Law [126]:

$$\sigma_{\text{elec}}(\omega) = \sigma_{DC} + A(2\pi f)^s \quad (3.11)$$

where:  $A$  is a characteristic parameter,  $f$  is the frequency and  $s$  is an exponent dependent on frequency or temperature.

The exponent  $s$  provides insights into the charge transport mechanisms in PEs and reflects the degree of interaction between charge carriers and their local environment [126]. The specific interpretations associated with different values of  $s$  are as follows:

- $s = 0$ : Ionic conduction, indicates that the conductivity is frequency-independent, meaning the material exhibits a purely DC (direct current) response. This suggests that the charge carriers move freely without exhibiting dispersive effects.
- $s = 1$ : Ideal Debye dielectric behavior.
- $0 < s < 1$ : Hopping mechanism, especially in disordered systems, such as PEs.

The characteristic parameter  $A$  reflects the effects of polarizability. A high value of  $A$  corresponds to a stronger polarizability force, which in turn increases the electrical resistance. Moreover, the polarizability strength can influence the frequency dependence of materials, such that the greater the polarizability strength, the more rapidly the electrical resistance will increase with increasing frequency [127].

In general, Equation 3.11 is used to fit the full conductivity curve, but fitting may be unsatisfactory over the entire frequency range due to system heterogeneity and varying charge carrier dynamics. In such cases, it is often more effective to analyze specific frequency ranges. Additionally, the DC term  $\sigma_{DC}$  may be absent from the experimental data, making the curve better described by the dispersive term  $A(2\pi f)^s$ .

### 3.3 First-Principles Calculations Using DFT: A Literature Review.

First-principles calculations, also known as *ab initio* methods, are computational approaches that aim to describe physical and chemical systems based solely on the fundamental laws of quantum mechanics, without relying on empirical parameters. Among these methods, DFT stands out as one of the most widely adopted frameworks for determining the electronic structure of molecules and materials due to its balance between computational efficiency and accuracy [128].

The quantum description of a system composed of  $N$  interacting electrons and  $M$  fixed nuclei (within the Born-Oppenheimer approximation) begins with the time-independent Schrödinger equation [129]:

$$\hat{H}\Psi(\mathbf{r}_1, \mathbf{r}_2, \dots, \mathbf{r}_N) = E\Psi(\mathbf{r}_1, \mathbf{r}_2, \dots, \mathbf{r}_N) \quad (3.12)$$

where the total Hamiltonian  $\hat{H}$  is composed of three main contributions:

$$\hat{H} = - \sum_{i=1}^N \frac{\hbar^2}{2m_e} \nabla_i^2 + \sum_{i<j} \frac{e^2}{|\mathbf{r}_i - \mathbf{r}_j|} + \sum_{i=1}^N V_{\text{ext}}(\mathbf{r}_i) \quad (3.13)$$

The first term represents the kinetic energy of the electrons, the second accounts for the electron–electron Coulomb repulsion, and the third corresponds to the interaction with the external potential generated by the nuclei. However, solving this many-body equation exactly becomes computationally intractable as the number of electrons increases, due to the exponential scaling of the many-electron wavefunction  $\Psi$ . To overcome this limitation, Density Functional Theory provides an alternative formulation in which the central quantity is no longer the many-body wavefunction, but the electron density  $\rho(\mathbf{r})$ .

According to the Hohenberg–Kohn theorems, (i) the ground-state electron density uniquely determines the external potential  $V_{\text{ext}}(\mathbf{r})$ , and (ii) there exists a universal energy functional  $E[\rho]$  that is minimized by the true ground-state density [129].

Kohn and Sham introduced a practical implementation of DFT by constructing a fictitious system of non-interacting electrons that reproduces the same electron density as the interacting system. The Kohn–Sham equations are written as:

$$\left[ -\frac{\hbar^2}{2m_e} \nabla^2 + V_{\text{eff}}(\mathbf{r}) \right] \psi_i(\mathbf{r}) = \varepsilon_i \psi_i(\mathbf{r}) \quad (3.14)$$

where  $\psi_i(\mathbf{r})$  are the Kohn–Sham orbitals and  $\varepsilon_i$  are their associated eigenvalues. The electron density is constructed from the occupied orbitals:

$$\rho(\mathbf{r}) = \sum_i^{\text{occ}} |\psi_i(\mathbf{r})|^2 \quad (3.15)$$

The effective potential  $V_{\text{eff}}(\mathbf{r})$  includes three components:

$$V_{\text{eff}}(\mathbf{r}) = V_{\text{ext}}(\mathbf{r}) + V_H(\mathbf{r}) + V_{\text{xc}}(\mathbf{r}) \quad (3.16)$$

where  $V_H$  is the classical Hartree term describing electron–electron repulsion, and  $V_{\text{xc}}$  is the exchange–correlation potential incorporating all many-body quantum effects.

A fundamental aspect of solving the Kohn–Sham equations is that the effective potential  $V_{\text{eff}}(\mathbf{r})$  depends on the electron density  $\rho(\mathbf{r})$ , which in turn depends on the orbitals  $\psi_i(\mathbf{r})$ . This circular dependency requires an iterative, self-consistent field (SCF) procedure to obtain converged solutions. The SCF process, proceeds as follows [130]:

1. An initial guess for the electron density  $\rho_0(\mathbf{r})$  is provided.
2. Using  $\rho_0(\mathbf{r})$ , the effective potential  $V_{\text{eff}}(\mathbf{r})$  is constructed.
3. The Kohn–Sham equations are solved to yield a new set of orbitals  $\{\psi_i\}$  and eigenvalues  $\{\varepsilon_i\}$ .
4. A new electron density  $\rho_1(\mathbf{r})$  is calculated from the updated orbitals.
5. The difference between  $\rho_1$  and  $\rho_0$  is assessed; if it falls below a predetermined convergence threshold, the process terminates.

6. Otherwise, a mixing scheme is applied to generate an updated density guess, and steps 2–5 are repeated until convergence.

This SCF cycle ensures that the output density and potential are consistent with one another, yielding the ground-state electron density and total energy of the system.

DFT offers a quantum mechanical approach for simulating structural relaxation by minimizing the system's total energy with respect to atomic positions. Based on the Hohenberg–Kohn theorems and Kohn–Sham formalism, it uses a self-consistent field (SCF) procedure to iteratively solve for the ground-state electron density and total energy. Starting from initial atomic configurations, DFT predicts the system's evolution toward a low-energy, stable state. At each step, atomic forces derived from the electronic structure guide position updates until convergence is reached, revealing the coupling between electronic behavior and atomic arrangement.

In composite materials, DFT-calculated formation energies are key to evaluating stability when reinforcement materials, such as ionic salts in polymer matrices, are added. These calculations predict whether the composite structure remains stable, aiding material design. Simulations are typically conducted using software like VASP, Quantum ESPRESSO, CASTEP, and ABINIT, which accurately model electronic and energy-related properties in complex systems.



## 4 METHODOLOGY

In this chapter, the synthesis process of the polymeric membranes (composites) is described, together with the experimental procedures employed for their structural, morphological, mechanical, thermal, and electrical characterization. The theoretical framework adopted for the analysis of their structural and electronic properties is also presented. In addition, the fundamental physical principles and equations underlying the applied methodologies are discussed, with the aim of justifying the chosen approaches and providing a clearer understanding of the obtained results.

### 4.1 Membranes preparation

The samples of polymeric membranes were prepared based on the Solvent Casting Method. Polyvinyl alcohol powder (PVA, hydrolyzed, average chemical purity 90%, average molecular weight of 30,000–60,000 g/mol) was purchased from Sigma-Aldrich. Lithium perchlorate ( $\text{LiClO}_4$ , purity > 95%) and lithium hydroxide ( $\text{LiOH}$ , purity > 95%) were both purchased from Sigma-Aldrich. Deionized water (DI) was used as a solvent in order to efficiently dissolve the polymers.

PVA/ $\text{LiOH}$  and PVA/ $\text{LiClO}_4$  were dissolved in water and homogenized until transparent solutions were obtained. The solutions contained  $\text{LiClO}_4$  at concentrations of 0, 1, 5, and 10%, and  $\text{LiOH}$  at concentrations of 0, 1, 3, 5, 7, and 9%. A magnetic stirrer was used for approximately 1 h under controlled conditions (700 rpm, 60 °C). To further ensure homogenization, the mixtures were subjected to an ultrasonic bath (LL20 Schuster) for 30 min. Subsequently, the solutions were cast into Petri dishes and dried in a laboratory oven at 60 °C to evaporate the solvent and form solid membranes. Finally, the dried films were removed, yielding the PVA-based membranes.

Table 4.1: Sample thicknesses for different PVA-based membranes. Thickness of approximately 0.1 mm ( $\pm 0.025$  mm) and diameter of 1.60 cm ( $\pm 0.010$  cm).

Sample	Thickness (mm)	Sample	Thickness (mm)
PVA	0.105	PVA	0.105
PVA- 1% LiOH	0.103	PVA- 1% LiClO <sub>4</sub>	0.101
PVA- 3% LiOH	0.124	PVA- 5% LiClO <sub>4</sub>	0.092
PVA- 5% LiOH	0.089	PVA- 10% LiClO <sub>4</sub>	0.104
PVA- 7% LiOH	0.122	—	—
PVA- 9% LiOH	0.122	—	—

## 4.2 Experimental Characterizations

### 4.2.1 Fourier Transform Infrared Spectroscopy:

The structural characteristics of the membranes were analyzed using FT-IR spectroscopy with a Cary Compact 630 spectrometer equipped with an ATR (Attenuated Total Reflection) device, which employs an internal reflection system. The measurements were conducted in transmittance mode over a broad spectral range (650–4000  $\text{cm}^{-1}$ ), providing a comprehensive profile of the membranes. The resulting spectra allowed a detailed examination of their chemical structure and composition, yielding valuable insights into their properties. All analyses were performed at NANOPOL – Laboratório de Polímeros Nanoestruturados, Universidade Federal do Amazonas (UFAM).

This study aims to analyze the vibrational modes of the composites as detected by FT-IR spectroscopy. The possible vibrational motions are illustrated in Figure 4.1. These modes include stretching, bending, twisting, and scissoring vibrations of molecular bonds. The FT-IR spectra enable the identification of functional groups and provide insights into the chemical structure, bonding environment, and possible interactions with the reinforcement material.

By examining shifts in peak positions or variations in intensity, changes in molecular interactions or the formation of new bonding environments can be inferred. Accordingly, the force constant ( $k$ ) of a vibrational mode can be calculated using Equation 4.1:

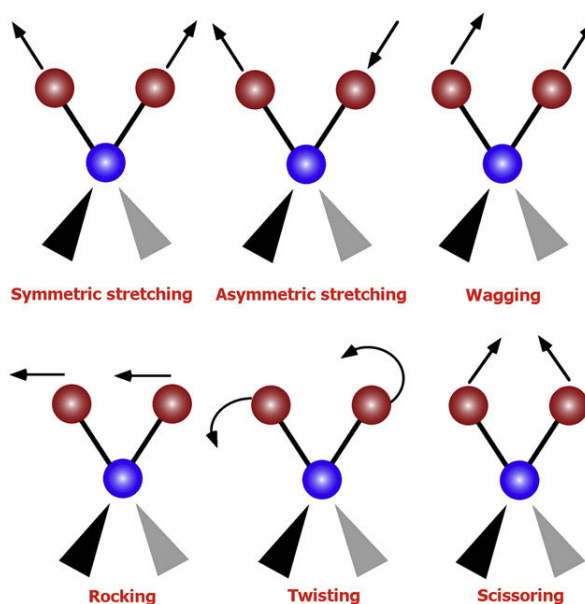


Figure 4.1: Vibrational modes associated to molecular dipole moment [13].

$$k = 4\pi^2 c^2 \mu \bar{\nu}^2 \quad (4.1)$$

where:  $\bar{\nu}$  is the wavenumber ( $\text{cm}^{-1}$ ),  $c$  is the speed of light ( $\text{cm/s}$ ),  $k$  is the bond force constant ( $\text{N/cm}$ ) and  $\mu$  is the reduced mass of the two atoms ( $\text{kg}$ ). The reduced mass  $\mu$  of the atoms involved can be calculated by:

$$\mu = \frac{m_1 m_2}{m_1 + m_2} \quad (4.2)$$

where  $m_1$  and  $m_2$  are the atomic masses of the atoms involved.

### 4.2.2 Raman Spectroscopy:

The structural characteristics of the membranes were examined by Raman spectroscopy (BWTech i-Raman Plus) using a 532 nm green laser. The output power was restricted to 25% of the maximum capacity to prevent thermal or photodegradation of the samples. Spectra were acquired in the 70–3800  $\text{cm}^{-1}$  range, providing a comprehensive evaluation of molecular vibrations and functional groups within the membranes.

Measurements were performed at the Escola Superior de Tecnologia (EST), Universidade do Estado do Amazonas (UEA).

### 4.2.3 X-Ray Diffraction:

Several material properties are intrinsically related to the structural arrangement defined by the atomic dispositions within the system. X-ray diffraction is employed to elucidate crystalline, semicrystalline, and amorphous structures based on the scattering of X-rays.

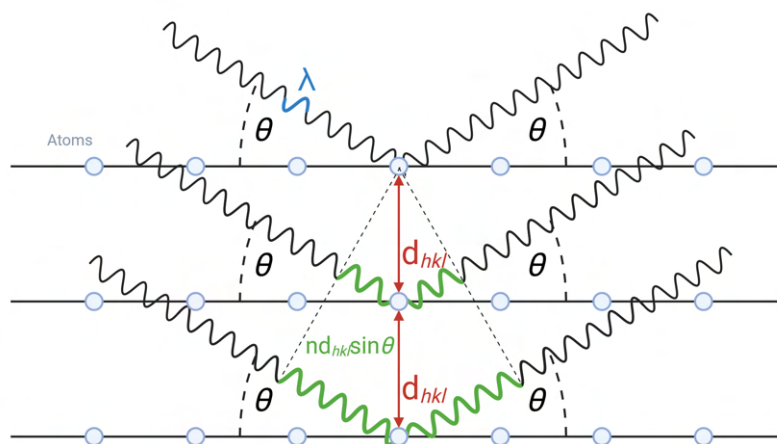


Figure 4.2: Bragg's law illustration based on incident and diffracted X-rays angles, wavelength and distance between structure planes [13].

Bragg's Law, fundamental to X-ray diffraction, provides a relationship between the wavelength of incident X-rays and the angle at which they are diffracted by a crystalline material. It is mathematically expressed as  $n\lambda = 2d \sin(\theta)$ , where  $n$  is an integer representing the diffraction order,  $\lambda$  is the wavelength of the X-ray,  $d$  is the distance between the crystal planes, and  $\theta$  is the angle of incidence. The term  $d_{hkl}$  refers to the interplanar spacing between the crystal planes indexed by the Miller indices  $h$ ,  $k$ , and  $l$ , which are specific to the crystallographic structure. Furthermore,  $nd_{hkl}$  represents the effective spacing for higher-order reflections, where  $n$  is the diffraction order. This law enables the determination of the crystal structure by analyzing the angles and intensities of the diffracted X-rays, thus providing crucial insights into the atomic arrangement of materials.

X-ray diffraction data were collected on an Empyrean diffractometer (Panalytical), using  $\text{CuK}\alpha$  radiation ( $\lambda = 1.54056 \text{ \AA}$ ), an accelerating voltage of 40 kV and a current of 40 mA. Measurements were performed in the angular range of  $5^\circ$  to  $60^\circ$  ( $2\theta$ ), with step sizes of  $0.01313^\circ$  with 300 s each step. X-ray photon detection was performed using a PIXcel3D-Medipix3 1x1 area detector.

The crystallographic parameters obtained from the measured XRD patterns were refined using the Rietveld method implemented in the GSAS software package. For the peak profile analysis, a modified Thompson-Cox-Hasting pseudo-Voigt profile function (CW profile function 4 in GSAS) was employed. The instrumental broadening was assessed using a certified LaB<sub>6</sub> standard (NIST 660b).

The background was fitted by using Chebyshev polynomials with 10 terms. So, the crystallinity percentage ( $x_c$ ) was calculated by:

$$x_c(\%) = \frac{100 \cdot (I_{\text{total}} - I_{\text{BG}})}{I_{\text{total}}} \quad (4.3)$$

Where  $I_{\text{total}}$  and  $I_{\text{BF}}$  are the total integrated and background intensities.

From the crystallographic parameters, a CIF file was generated, and these data were used to observe the unit cell, then mer repetitions. XCRYSDEN was the program used.

The measurements were conducted at the Materials Laboratory (LabMat), established within the Department of Physics at UFAM.

#### **4.2.4 Scanning Electron Microscopy and Energy Dispersive X-ray Spectroscopy:**

SEM-EDS analysis was performed using a TESCAN VEGA3 microscope to obtain high-resolution morphological images of the membranes. A tungsten filament source was coupled with an energy-dispersive X-ray spectrometer to determine the elemental composition of the samples. To enhance image quality and ensure accurate surface analysis, the samples were metallized prior to examination in the scanning electron microscope. The resulting images covered a size range from 25  $\mu\text{m}$  to 2  $\mu\text{m}$  and were acquired at an acceleration voltage of 5 kV.

All measurements were conducted at Denso Industrial da Amazônia, Manaus.

#### **4.2.5 Differential Scanning Calorimetry and Thermogravimetric:**

Thermal analysis was performed using DSC and TGA measurements under an N<sub>2</sub> atmosphere with a flow rate of 10 ml/min. The samples were analyzed over a temperature range from room temperature (25 °C) to 700 °C, with a heating rate of

10 °C/min. Through these measurements, key thermal properties such as the glass transition temperature, melting temperature ( $T_m$ ), and heat of fusion/enthalpy were determined.

The crystallinity percentage was calculated by the equation:

$$X_c(\%) = \frac{\Delta H_m}{\Delta H_m^0} \times 100 \quad (4.4)$$

Where  $\Delta H_m^0 = 138.6 \text{ J/g}$  is the heat to melting PVA 100% crystalline. The term  $\Delta H_m$  refers to the melting enthalpy of the sample, which represents the heat absorbed during the melting of its crystalline regions.

The measurements were performed at LFQM, Laboratório de ensaios de Físico-Química de Materiais, Department of Materials Engineering, UFAM.

#### 4.2.6 Dynamical Mechanical Analysis:

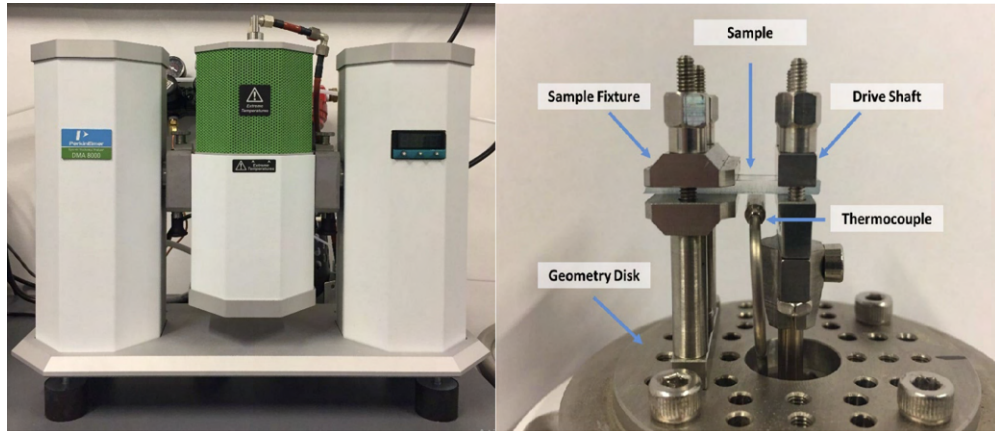


Figure 4.3: Perkin Elmer DMA 8000 model [14].

The anelastic properties of PVA membranes were characterized through complex Young's modulus measurements. The storage modulus, often denoted as  $M'_{\text{mech}}$  or simply as the modulus, and the loss modulus,  $M''_{\text{mech}}$ , are key parameters in Dynamic Mechanical Analysis analysis. These moduli are typically represented as the real and imaginary components of a complex modulus  $M^*_{\text{mech}}$ , and their relationship can be expressed by Equations 4.5 and 4.6, where  $i$  is the imaginary unit:

$$M^*_{\text{mech}} = M'_{\text{mech}} + iM''_{\text{mech}} \quad (4.5)$$

$$\tan(\delta) = \frac{M''_{\text{mech}}}{M'_{\text{mech}}} \quad (4.6)$$

The  $\tan \delta$  in DMA is defined as the ratio of the loss modulus ( $M''_{\text{mech}}$ ) to the storage modulus ( $M'_{\text{mech}}$ ), reflecting the balance between the viscous and elastic behavior of a material. This parameter is frequency-dependent, as viscoelastic materials respond differently to slow and fast deformations.

Now about the DMA setup. In the tensile mode of DMA, the sample is securely clamped at both ends, while the drive shaft applies oscillatory deformation along its length. The sample fixture ensures proper alignment and stability during testing. This setup allows for precise evaluation of the viscoelastic behavior of thin polymer membranes under uniaxial tensile stress, see Figure 4.3.

Dynamical Mechanical Analyzer (DMA, Perkin Elmer DMA 8000) was the machine used. The DMA operated in a tension geometry with a displacement of 10  $\mu\text{m}$ , covering frequencies of 0.1, 1, and 10 Hz at room temperature (25 °C) fixed by the thermocouple. The samples utilized in DMA measurements were thin membranes with a width of approximately 4-5 mm, a length of 10 mm, and a thickness ranging from 0.3-0.5 mm. The DMA protocol involved time scans over 30 minutes under isothermal conditions, utilizing the single frequency mode. DMA data were collected every 15 s for 1 and 10 Hz, while for 0.1 Hz, the acquisition time extended to about 45 s.

The testing was conducted at Federal University of São Carlos (UFSCar).

#### **4.2.7 Strain-stress tensile test:**

Mechanical properties, such as Young's modulus and toughness, are essential for understanding a material's response under load. Young's modulus quantifies the stiffness of the material within the elastic region, whereas toughness reflects its capacity to absorb energy prior to failure. These parameters are typically determined through uniaxial tensile testing, providing critical insights into both strength and ductility.

The linear elasticity observed during uniaxial deformation at low stress allows the calculation of the Young's modulus ( $E$ ) using the classic stress–strain relation, as expressed in Equation 4.7:

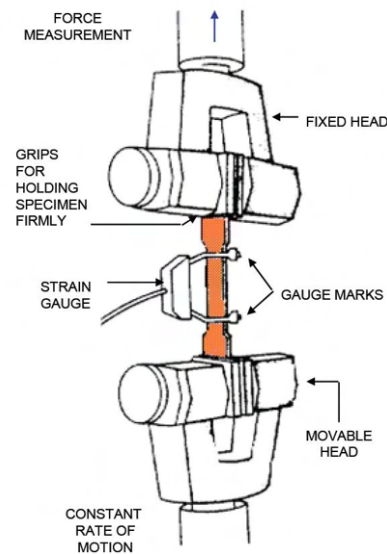


Figure 4.4: Standard strain-stress setup [14].

$$E = \frac{\sigma_{\text{mech}}}{\varepsilon_{\text{mech}}} \quad (4.7)$$

where  $E$  is given in MPa.

The area under the stress–strain curve allows for the calculation of the material’s resistance to fracture. This parameter, referred to as toughness, is defined as the total energy absorbed per unit volume prior to failure, reflecting both the material’s strength and ductility. Toughness ( $U_T$ ) is obtained by integrating the stress ( $\sigma_{\text{mech}}$ ) over the strain ( $\varepsilon_{\text{mech}}$ ), as shown in Equation 4.8:

$$U_T = \int_0^{\varepsilon_f} \sigma_{\text{mech}} d\varepsilon_{\text{mech}} \quad (4.8)$$

Strain–stress tests were conducted using an Instron 5564 tensile tester equipped with Bluehill Universal software, following the guidelines of ASTM D882 (considering gauge measurements) for thin plastic sheets, as illustrated in Figure 4.4. The specimens were preloaded to 1.0 N, with grips fixed, and subjected to testing at a constant displacement rate of 1 N/min. Measurements were recorded with a vertical ramp rate of 10 mm/min until membrane failure. To ensure reliability and accuracy, three membranes from each sample were tested, and the average values were reported.

All testing was performed at INDT, Instituto de Desenvolvimento Tecnológico, Manaus.



## 4.2.8 Complex Impedance Spectroscopy:

To investigate the electrical response of the solid membranes, Complex Impedance Spectroscopy was employed. Measurements were conducted using a Solartron 1260 (Analytical Ametek) over a frequency range of 10 Hz to 1 MHz. An AC voltage of 500 mV was applied at room temperature, allowing determination of the bulk resistance. All analyses were performed at LPMat – Laboratório de Processamento de Materiais Tecnológicos, UFAM.

The resulting CIS spectra were analyzed and fitted using ZView<sup>®</sup> software, applying complex nonlinear least-squares fitting with Calc-Modulus weighting to accurately model the experimental data. The quality of the fitting was evaluated using two key parameters:

- **Correlation Coefficient ( $R$ )**

The correlation coefficient evaluates the degree of linear relationship between the experimental data and the fitted values. An  $R$  value close to 1 indicates a highly reliable fit.

- **Reduced Chi-Square ( $\chi_{\text{red}}^2$ )**

The reduced chi-square is a statistical indicator that measures the discrepancy between experimental and model-predicted values, normalized by the degrees of freedom. A value of  $\chi_{\text{red}}^2$  close to 1 typically suggests a good fit, whereas significantly higher or lower values may indicate overfitting or underfitting.

$$\chi^2 = \frac{1}{N - P} \sum_{i=1}^N \left[ (Z'_{i,\text{exp}} - Z'_{i,\text{fit}})^2 + (Z''_{i,\text{exp}} - Z''_{i,\text{fit}})^2 \right] \quad (4.9)$$

where:

- $N$  is the total number of data points,
- $P$  is the number of fitted parameters,
- $Z'_{i,\text{exp}}$  and  $Z''_{i,\text{exp}}$  are the real and imaginary parts of the experimental impedance at point  $i$ ,
- $Z'_{i,\text{fit}}$  and  $Z''_{i,\text{fit}}$  are the corresponding real and imaginary parts from the fitted model.

The corresponding formalisms derived from the impedance data—namely, electrical conductivity, electric modulus, and permittivity—were obtained through Equations 3.9, 3.8, and 3.4, respectively.

The conductivity spectrum is analyzed using the Jonscher model, equation 3.11 (defined as Model 1) is applied to different frequency regions. While the following equation is defined as Model 2:

$$\sigma_{\text{elec}}(\omega) = A(2\pi f)^s \quad (4.10)$$

And, to study the relaxation processes of the different mechanisms observed, the electric modulus formalism was chosen, which in the Havriliak-Negami model is expressed as:

$$M_{\text{elec}}^* = M_{\infty} (1 - F_{HN}(\omega)) \quad (4.11)$$

where,

$$F_{HN} = \frac{1}{(1 + (i\omega\tau_{HN})^{\alpha})^{\gamma}} \quad (4.12)$$

Where  $M_{\infty}$  is the relaxed modulus,  $\tau_{HN}$  is the relaxation time, and  $\alpha$  and  $\gamma$  are relaxation parameters ranging from 0 to 1. The model consists of fitting the experimental data using the real and imaginary parts of the complex quantity through equations that relate the characteristic empirical parameters to a relaxation time distribution function. The values of the constants are associated with the correlation of motion between the hopping ions and their surroundings.

## 4.3 Theoretical calculations:

### 4.3.1 DFT approaches.

First-principles calculations based on DFT were carried out to investigate the interaction between  $\text{Li}^+$  ions and the PVA chain in the formation of PVA/LiOH membranes. Initial atomic structures were derived from experimental CIF files and fully relaxed using the QUANTUM ESPRESSO package. A LiOH content of 7% was used to match

experimental conditions, with concentration fixed based on the molecular masses of LiOH and PVA. The PVA chains were periodically extended along the  $x$ -axis in an orthorhombic box, with coordinates consistent. The supercell model consisted of 56 atoms. Calculations employed the Perdew–Burke–Ernzerhof (PBE) functional within the generalized gradient approximation (GGA), with plane-wave cutoffs of 1.2 keV for kinetic energy and 12 keV for charge density. Brillouin zone sampling was performed using a  $4 \times 4 \times 4$  Monkhorst-Pack  $k$ -point grid, and van der Waals interactions were accounted for via Grimme’s DFT-D2 correction. Structural visualization was conducted using XCRYSDEN.

The cluster allocated at the Laboratório de Modelagem e Simulação Computacional - LMSC of UFAM was utilized to perform the computational calculations presented in this thesis.

The interaction between lithium ions and polymer matrices plays a critical role in defining the ion transport properties of polymeric systems. The adsorption energy serves as a measure of the strength of these interactions, which must be optimized to ensure both effective coordination and sufficient ionic mobility. Achieving this balance is essential for enabling efficient ion conduction in applications where controlled lithium transport is required. So, the formation energies due to adsorption were calculated using:

$$E_F = E_{\text{Li-PVA}(\alpha)} - E_{\text{Li}} - E_{\text{PVA}(\alpha)} \quad (4.13)$$

## 5 RESULTS AND DISCUSSION

### 5.1 PVA/LiOH membranes

#### 5.1.1 Structural/Morphological Properties Investigated via Experimental and theoretical Techniques.

The structural characterization of the polymeric membranes was performed using FT-IR and Raman spectroscopies, along with XRD analysis. These complementary techniques provide valuable insights into the functional groups, molecular interactions, and crystalline behavior of the materials. Together, they enable a comprehensive understanding of the structural modifications induced by the incorporation of additives into the PVA matrix. Additionally, DFT calculations supported the interpretation of structural stability and Lithium adsorption. Morphological and elemental analyses were further conducted through SEM coupled with EDS, allowing visualization of surface features and elemental distribution.

The vibrational spectrum of PVA can be interpreted based on the vibrational modes of its repeating unit,  $-\text{CH}_2-\text{CHOH}-$ , also known as the mer, which contains seven atoms. In the absence of significant crystallinity or long-range order, the vibrational behavior of PVA can be approximated using a simple linear molecular model. According to the standard rule for non-linear molecules, the number of fundamental vibrational modes is given by  $3N - 6$ , where  $N$  is the number of atoms. For the PVA repeating unit with  $N = 7$ , this corresponds to 15 fundamental vibrational modes. However, in real polymer systems, such as cast membranes, additional effects must be considered. Local symmetry breaking, vibrational coupling between adjacent molecular units, and intermolecular interactions (e.g., hydrogen bonding) can lead to the splitting or activa-

tion of otherwise IR-inactive modes, potentially increasing the number of observable bands to 17 or more. Conversely, some vibrational modes may also become inhibited or suppressed, depending on the molecular environment[131, 132].

The FT-IR transmittance spectrum of pure PVA reveals the main characteristic bond vibrations of the polymer, as shown in Figure 5.1A). A broad absorption band centered at  $3273\text{ cm}^{-1}$  corresponds to the O–H stretching of hydroxyl groups, while a band at  $2926\text{ cm}^{-1}$  is attributed to C–H stretching. The C–O stretching vibration is observed at  $1080\text{ cm}^{-1}$ . Additionally, a peak around  $1700\text{ cm}^{-1}$  is assigned to the C=O stretching of residual acetate groups present in partially hydrolyzed PVA [133].

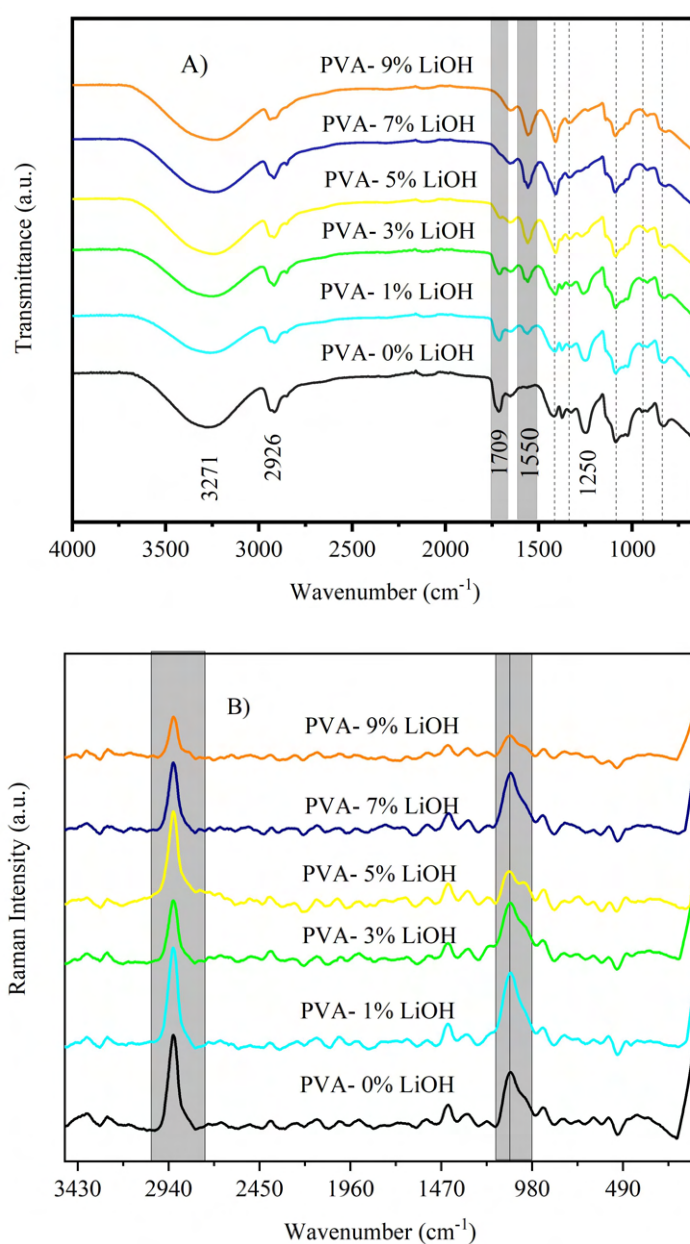


Figure 5.1: A) FT-IR and B) Raman spectra of the membranes with LiOH addition.

The absence of new peaks in the FT-IR and Raman spectra indicates that  $\text{Li}^+$  ions do not form covalent bonds with either the crystalline or amorphous regions of the PVA structure. Upon incorporation of LiOH into the polymer matrix, the salt dissociates into  $\text{Li}^+$  and  $\text{OH}^-$  ions. The hydroxide ions, due to their strong basic and nucleophilic nature, promote the hydrolysis of residual acetate groups [134]. This reaction converts ester groups into carboxylate species, effectively eliminating the  $\text{C}=\text{O}$  stretching band at approximately  $1700\text{ cm}^{-1}$ . As a result, this band disappears following the addition of LiOH, and a new band corresponding to the asymmetric or bending ( $\text{C}-\text{O}$  or  $\text{O}-\text{H}$ ) stretching emerges, indicating chemical modification of the polymer backbone. The grey vertical stripes in Figure 5.1A) highlight the key vibrational modes discussed.

In Figure 5.1B), the Raman spectra of the PVA and PVA/LiOH samples are presented. A similar behavior is observed compared to the FT-IR spectra, confirming that these are characteristic peaks of PVA. A band associated with  $\text{C}-\text{H}$  vibrations is observed at  $2900\text{ cm}^{-1}$ , while a symmetric  $\text{C}-\text{O}$  stretching vibration appears around  $1100\text{ cm}^{-1}$ . Covalent bonds such as  $\text{C}-\text{C}$  and  $\text{C}-\text{H}$  do not exhibit sufficient changes in polarizability to produce Raman-active modes. Therefore, only polar vibrational modes, which are more sensitive to inelastic light scattering, are identified in the Raman spectra.

Table 5.1: Assignments of FT-IR and Raman for PVA. (stretching =  $\nu$ , bending =  $\delta$ , wagging =  $\gamma$ , rocking =  $\rho$ ).

Wavenumber ( $\text{cm}^{-1}$ )	Assignment
830	$\nu_{\text{CC}} / \rho_{\text{CH}}$ [135, 136]
920	$\delta_{\text{CC}}$ [135]
1080	$\nu_{\text{CO}}$ [135, 136, 137]
1240	$\delta_{\text{CH}}$ [136, 137]
1330	$\nu_{\text{CH}} + \delta_{\text{OH}}$ [135, 137]
1370	$\delta_{\text{CH}}$ [136]
1420	$\nu_{\text{C-H}}$ [136, 137]
1440	$\gamma_{\text{CH}}$ [135]
1550	$\nu_{\text{C-O}}, \delta_{\text{C-O}}, \delta_{\text{O-H}}$
1709	$\nu_{\text{C=O}}$ (residual acetate) [135, 137]
2926	$\nu_{\text{C-H}}$ [136, 137]
3273	$\nu_{\text{O-H}}$ [135, 136, 137]

To organize the information obtained from both spectra, Table 5.1 summarizes all FT-IRx and Raman assignments for PVA according to their corresponding wavenumbers [135, 136, 137].

Significant changes in the intensity of the O–H, C–H, and C–O peaks were observed, indicating and supporting the occurrence of physical interactions between lithium ions and the polymer matrix. Additionally, subtle redshifts in the O–H and C–C stretching vibrations were detected. These shifts in wavenumber observed in the FT-IR spectra can be attributed to changes in bond force constants and slight variations in bond lengths, reflecting modifications in the local chemical environment.

The force constant ( $k$ ) of a vibrational mode can be calculated using Equation 4.1, where  $m_1$  and  $m_2$  represent the atomic masses of the atoms involved in the vibration (e.g., O, H, or C). The vibrational wavenumbers and the corresponding atomic pairs required for this calculation are listed in Table 5.2.

Table 5.2: Force constant values corresponding to the effects of lithium ions on PVA bonding, obtained through the diatomic molecule vibrational oscillator model, utilizing FT-IR-derived wavenumbers.

<b>Chemical bond</b>	<b>Wavenumber (cm<sup>-1</sup>)</b>	<b>Force Constant, <math>k</math> (N/cm)</b>
O–H	3271	417.4
O–H	3233	408.5
C–C	1428	1.14
C–C	1409	1.11

As shown in Table 5.2, the force constants for both O–H and C–C bonds decrease. This reduction in  $k$  indicates a weakening of these bonds, suggesting an increase in the interatomic bond length. Such behavior can be attributed to polarization effects induced by the presence of ions.

Figure 5.2 presents the normalized powder X-ray diffraction (PXRD) patterns for pure PVA powder, crystalline LiOH, and PVA membranes containing 1, 3, 5, 7, and 9 wt% of LiOH. Notably, the characteristic diffraction peaks of crystalline LiOH are absent in the PXRD profiles of the PVA membranes after synthesis, indicating that LiOH has fully dissociated during the process. The PVA powder exhibits distinct peaks at 19.6° and 22.8°, consistent with the findings of Rajendran et al. [138]. These peaks correspond to reflections from the monoclinic unit cell of the polymer. Furthermore, M.A. Bzra et al. [139] associated the peak at 40.3° with crystalline features, attribut-

ing it to the (11 $\bar{1}$ ) plane. The PVA membranes exhibit a lower baseline and reduced intensity of the peaks at 22.8° and 40.3°, which can be ascribed to changes in polymer chain length caused by hydrolytic degradation during synthesis.

The XRD patterns of the membranes exhibit a visually similar profile, displaying pronounced amorphous behavior that persists regardless of the composition.

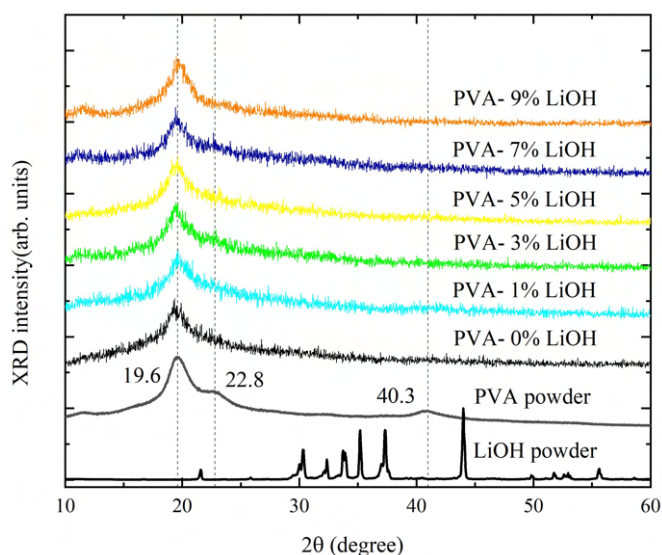


Figure 5.2: X-ray diffraction patterns of precursor substances (pure PVA and LiOH powders) and PVA/LiOH membranes.

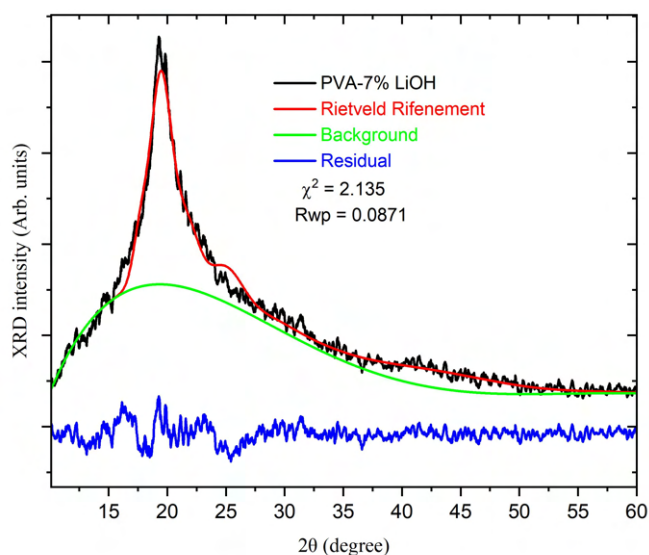


Figure 5.3: Fitted experimental X-ray diffraction pattern of the PVA-7% LiOH sample obtained through Rietveld structural refinement.

To investigate subtle differences among the diffraction patterns of the membranes, XRD analysis was performed using the Rietveld refinement method, incorporating



atomic positions and unit cell reported in the literature, with approximate values  $a = 7.82 \text{ \AA}$ ,  $b = 2.52 \text{ \AA}$ ,  $c = 5.52 \text{ \AA}$ , and  $\beta = 91.05^\circ$  [95, 11]. Reference [33] proposed two monoclinic space groups,  $P2_1/m$  and  $P2_1/c$ , to describe the diffraction profile of PVA powder, suggesting that the  $P2_1/c$  model provided a better fit to their data. However, in the present study, the  $P2_1/c$  space group did not yield satisfactory refinement results for our samples. In contrast, the refinement using the  $P2_1/m$  model resulted in acceptable agreement with the experimental patterns, supporting its suitability for describing the membrane structure under our processing conditions.

According to Table 5.3, the unit cell parameters gradually increased, supporting the interpretations previously discussed in the FT-IR and Raman analyses. Additionally, the degree of crystallinity was calculated, indicating that the membranes predominantly exhibit amorphous structures, with a slight increase in crystallinity observed upon the addition of the ionic salt.

Through Rietveld refinement, the unit cell structure—and consequently the repetition of polymer monomer units—was confirmed, as illustrated in Figure 5.4. It is important to note that this structural model represents a general configuration, based on Brunn's proposition. Its successful refinement was achieved using this model, which reproduces two oxygen atoms bonded to two carbon atoms within the unit cell. However, this configuration does not strictly correspond to the actual structure of PVA, as oxygen atoms in PVA randomly alternate along the polymer chain, forming atactic repetitions rather than a perfectly ordered arrangement.

In an atactic configuration, the hydroxyl groups (OH) attached to the polymer backbone are distributed without defined stereochemical order, resulting in a random spatial orientation of these side groups [140]. This lack of regularity disrupts the stereoregular symmetry typically observed in isotactic or syndiotactic polymers, contributing to partial structural disorder. To account for this statistical distribution within the crystallographic model, the hydroxyl groups are represented as half-occupied positions ( $1/2 \text{ OH}$ ), reflecting their averaged presence across possible sites rather than fixed locations. Despite this local disorder, the zigzag conformation of the PVA backbone is clearly observed in projections along the  $a$  and  $b$  crystallographic axes, indicating a trans-planar chain arrangement.

Table 5.3: PVA lattice parameters (monoclinic symmetry, space group  $P2_1/m$ ,  $\alpha = \gamma = 90^\circ$ ) and crystallinity obtained from Rietveld refinement and literature.

Sample	$a$ (Å)	$b$ (Å)	$c$ (Å)	$\beta$ (°)	$V$ (Å <sup>3</sup> )	$x_c$ (%)
PVA	7.832(5)	2.549(2)	5.512(7)	92.35(9)	109.9(1)	28.3
1 wt%	7.837(6)	2.554(2)	5.516(4)	92.16(9)	110.4(2)	27.6
3 wt%	7.852(5)	2.562(1)	5.519(3)	92.13(9)	111.1(1)	28.4
5 wt%	7.861(6)	2.569(6)	5.520(5)	92.07(12)	111.5(2)	28.9
7 wt%	7.876(5)	2.574(3)	5.521(2)	92.00(10)	112.0(1)	29.8
9 wt%	7.890(4)	2.582(5)	5.523(3)	91.93(7)	112.5(4)	30.4
Ref. [33]	7.823	2.524	5.500	90.21	108.6	–
Ref.[11]	7.81	2.52	5.51	91.42	108.4	

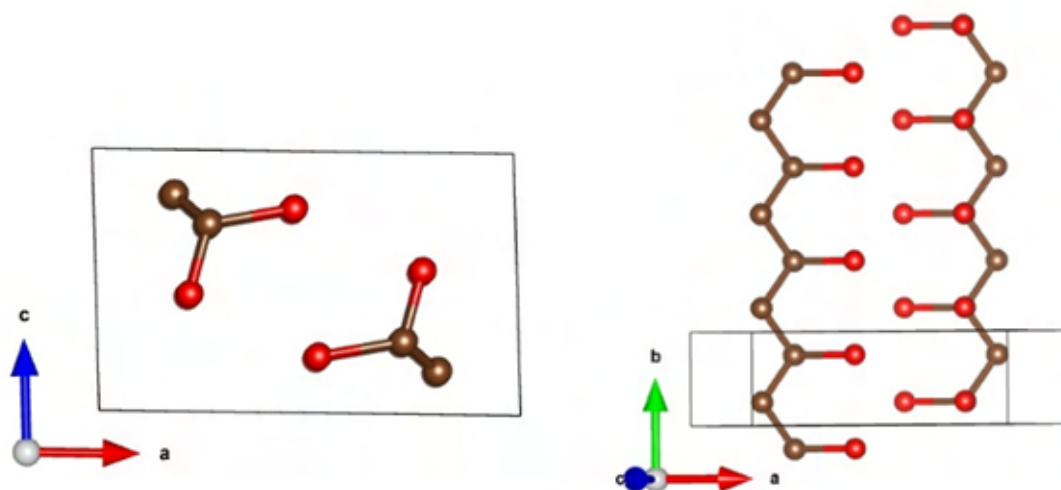


Figure 5.4: PVA's unit cell and mer repetitions. The PVA unit cell, assigned to the monoclinic space group  $P2_1/m$ , contains two polymer chains related by a mirror plane, with one being the mirror image of the other. This symmetry promotes packing through intermolecular hydrogen bonding.

#### 5.1.1.1 Energetic Stability and Lithium Ion Coordination Analysis by DFT

The system generated from the experimental Crystallographic Information File, obtained from X-ray diffraction measurements, was separated into individual unit cell conformations. Hydrogen atoms were added, and the structures were subsequently relaxed. It was confirmed that both conformations remained stable upon separation and are shown in Figure 5.5, labeled as PVA-1 and PVA-2.

Figure 5.5 illustrates the optimized structures, in which carbon atoms are depicted in yellow, oxygen atoms in red, hydrogen atoms in blue, and lithium atoms in gray.

An analysis of the energetics of the two possible PVA conformations indicates that PVA-2 exhibits higher stability. The energy of PVA-2 is approximately 0.01 eV lower than that of PVA-1. The band-gap energies of the two conformations were also calculated, yielding 4.79 eV for PVA-1 and 4.99 eV for PVA-2.

To understand the effect of LiOH on PVA, a 7% concentration was considered for both conformations. The formation energy of a lithium ion interacting with the polymer corresponds to the energy change associated with the incorporation of the ion into the polymer matrix [141]. This parameter reflects the stability of the resulting complex and indicates whether the interaction is energetically favorable.

The formation energies due to lithium ion insertion were calculated using equation 4.13, giving us the following table 5.4.

Table 5.4: Formation energies ( $E_F$ ) for PVA conformations with Li adsorption

<b>Conformation</b>	<b>Formation Energy (<math>E_F</math>) [eV]</b>
PVA-1	-1.27
PVA-2	-0.97

Both conformations form stable structures upon lithium ion coordination. Lithium ions interact with PVA via a coordination mechanism, forming complexes with the hydroxyl (-OH) groups along the polymer chains [142, 143, 144]. The oxygen atoms of these hydroxyl groups, possessing lone electron pairs, act as electron donors, establishing coordinate bonds with the  $\text{Li}^+$  cations. This interaction is characterized by Li-O bond lengths ranging from approximately 1.85 Å to 1.96 Å for the PVA-1+Li system, and from 1.87 Å to 1.99 Å for PVA-2+Li, indicating specific and relatively strong interactions distinct from the weaker forces associated with physisorption.

Furthermore, PVA-1+Li exhibits a lower formation energy and a higher probability of formation compared to PVA-2+Li, indicating a more favorable and stable  $\text{Li}^+$  coordination in this configuration. This bonding plays a key role in stabilizing lithium ions within the polymer matrix, directly affecting both the structural arrangement and the dynamics of the system, including ion mobility and polymer chain conformation. Importantly, despite the predominantly ionic nature with partial covalent character of the Li-O bonds, the association remains reversible and dynamic, allowing  $\text{Li}^+$  ions to

migrate and the polymer chains to reorient within the polymer structure.

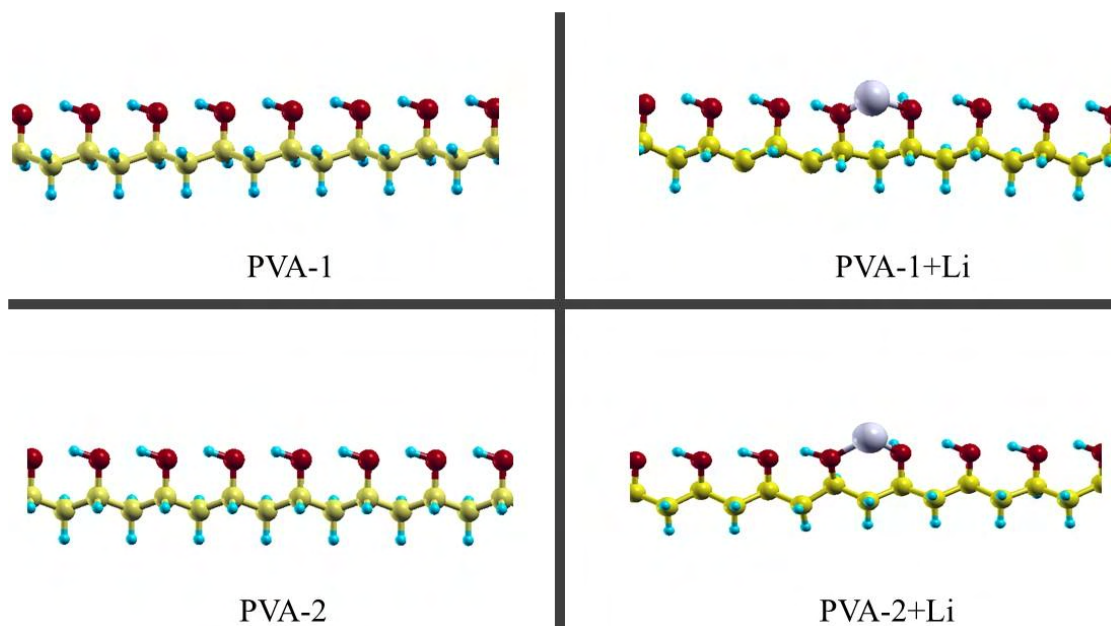


Figure 5.5: Relaxed structures before and after lithium ion insertion. PVA-1 structure projected onto the  $-\mathbf{b} \times \mathbf{a}$  plane and PVA-2 structure projected onto the  $-\mathbf{b} \times -\mathbf{c}$  plane. Li–O bond lengths varying approximately between 1.85 Å and 1.96 Å for the PVA-1+Li system, and between 1.87 Å and 1.99 Å for PVA-2+Li. O–H and C–C bond lengths also increased but the presence of lithium maintained the structural stability of both systems.

Molecular modeling of PVA revealed activation energies for hydroxyl and backbone conformational transitions ranging from 10 to 52 kJ/mol (0.10–0.54 eV), indicative of moderate segmental mobility and weak hydrogen-bonding interactions governed by physisorption. For comparison, lithium interactions with functionalized polymers, typically studied for applications such as selective ion binding, are stronger and site-specific. For PAA–Li, Li–O distances of 2.00 to 2.15 Å correspond to adsorption energies of  $-1.5$  to  $-2.5$  eV [145]. Sulfonated lignin exhibits Li–O distances of 1.753 to 1.862 Å with energies between  $-1.7$  and  $-2.3$  eV [146], while PAN/kaolin composites show Li–O distances near 1.9 Å with energies around  $-2.1$  eV [147]. This comparison highlights the transition from weak physisorption in pristine PVA to stronger chemisorption in  $\text{Li}^+$ -functionalized polymer matrices.

For PVA–  $\text{Li}^+$  interactions, the present study reports  $\text{Li}^+$ –O bond lengths ranging from 1.85 to 1.99 Å with formation energies between  $-1.27$  and  $-0.97$  eV, indicating an intermediate interaction strength. These values lie between typical physisorption and strong chemisorption ranges reported for  $\text{Li}^+$  coordination in functionalized polymers, highlighting PVA’s potential as a host polymer capable of stabilizing  $\text{Li}^+$  ions while

maintaining some dynamic mobility.

### 5.1.1.2 Morphological Characterization of the Samples

Figure 5.6 shows the morphology of the membranes as revealed by Scanning Electron Microscopy. To obtain high-quality images under vacuum, the membranes were sputtered with a thin gold film. The images are presented at the microscale, with a scale of 10–20  $\mu\text{m}$ .

The PVA membranes prepared by solvent casting exhibited a dense, non-porous morphology, as confirmed by SEM. In Figure 5.6, the image of the pure PVA membrane shows a smooth surface, consistent with its expected amorphous nature, as well as the transparency and enhanced refractive index of the membrane [100, 148]. This compact and homogeneous surface, typical of films formed by controlled drying of aqueous PVA solutions, is advantageous for solid electrolyte applications, as the absence of pores prevents undesired ionic pathways and promotes controlled ion transport through the polymer matrix. Therefore, the semi-crystallinity structure of PVA is likely submicroscopic in nature [149].

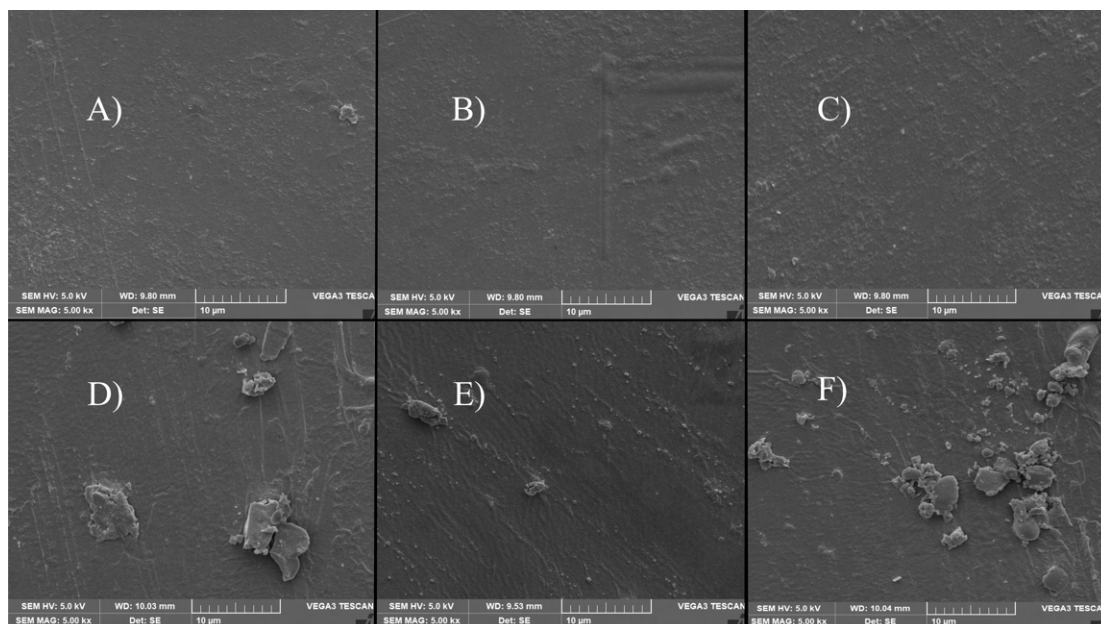


Figure 5.6: Morphology images of the membranes by SEM, labeled from A) to F). Image A) shows the pure PVA membrane, while images B) through F) correspond to membranes with increasing LiOH content at 1%, 3%, 5%, 7%, and 9% (w/w), respectively.

Upon the addition of LiOH, as shown in Figures 5.6D–F), no well-defined

spherulitic structures or crystalline salt domains were observed. Instead, a few irregularly shaped polymeric agglomerates appeared, most likely resulting from interactions between  $\text{Li}^+$  ions and PVA, which may have disrupted local hydrogen bonding and induced minor reorganization during solvent evaporation. These agglomerates were sparse and did not significantly modify the overall morphology of the membranes. Consistent with this observation, no structural changes were detected in XRD or Raman spectra, indicating that these features are localized and do not compromise the overall integrity or homogeneity of the membranes. It is therefore reasonable to assume that such minor and dispersed irregularities will not substantially affect other physicochemical analyses.

The results presented in Table 5.5 include measurement uncertainties ( $\sigma_{\text{EDS}}$ ) ranging from 0.6 to 1.0 wt%, which represent acceptable precision for elemental quantification by EDS and support a reliable interpretation of the sample composition. The incorporation of  $\text{OH}^-$  ions increases the oxygen proportion and, consequently, decreases the relative carbon content, as expected.  $\text{Li}^+$  ions are not detected in the spectrum, since light elements such as hydrogen and lithium cannot be quantified by this technique, resulting in spectra dominated by the carbon and oxygen contributions from PVA [150].

A small proportion of gold was detected in the EDS analysis, which is attributed to the conductive gold coating applied to the sample surface prior to measurement.

Table 5.5: Elemental composition of the analyzed samples as determined by EDS, presented in weight percent (Wt%) along with the associated standard deviations ( $\sigma_{\text{EDS}}$ ).

<b>Element</b>	<b>PVA (Wt% <math>\pm\sigma_{\text{EDS}}</math>)</b>	<b>9% LiOH (Wt% <math>\pm\sigma_{\text{EDS}}</math>)</b>
C	59.9 $\pm$ 0.9	47.1 $\pm$ 1.0
O	29.4 $\pm$ 0.9	40.6 $\pm$ 1.0
Au	10.7 $\pm$ 0.6	12.3 $\pm$ 0.6

This behavior contrasts with reports on other lithium salts, such as LiTFSI and  $\text{LiPF}_6$ , which are known to induce pronounced morphological modifications in polymers [151, 152]. In these systems, the stronger disruption of hydrogen bonding frequently promotes phase separation, increased porosity, or crystallinity changes, ultimately compromising membrane uniformity.

## 5.1.2 Assessment of Thermal Properties Using Tg and DSC Techniques

Thermal analysis plays a fundamental role in the characterization of polymer membranes, offering critical insights into their stability, phase transitions, and degradation pathways. Techniques such as thermogravimetric analysis and differential scanning calorimetry allow the evaluation of temperature-dependent properties that are essential for ensuring membrane reliability and long-term performance in advanced applications.

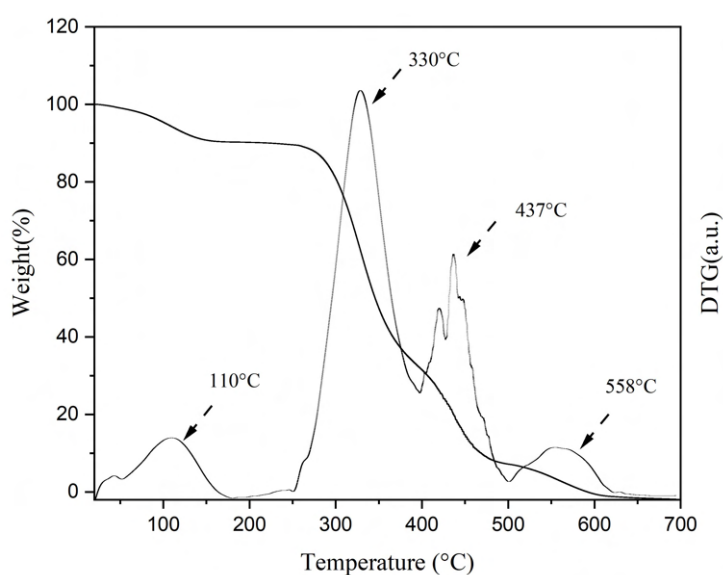


Figure 5.7: TG and DTG curves of PVA membrane. Major mass loss peaks are highlighted.

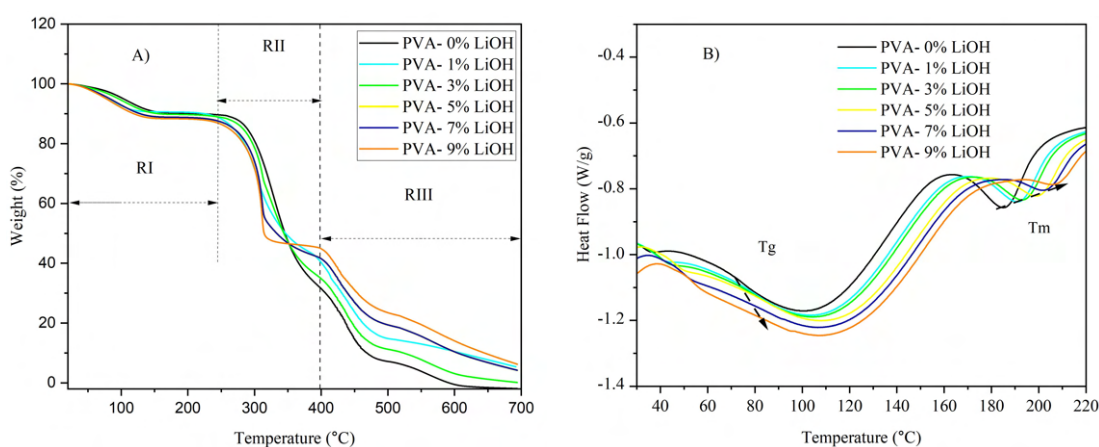


Figure 5.8: TG and DSC (exo up convention) curves of PVA/LiOH membranes. Glass and melting temperature are indicated in the graph.

In Figure 5.7, the TGA profile of the pure PVA membrane is presented together with the derivative thermogravimetric (DTG) curve, plotted as a function of temperature and normalized as percentage of total mass and arbitrary units, respectively. In Region I (RI), a mass loss of approximately 10 °C is observed around 110 °C, corresponding to moisture release. This dehydration process mainly occurs between 50 and 130 °C, associated with the evaporation of absorbed and bound water. Following this stage, a plateau is observed up to nearly 250 °C, indicating a temperature interval of thermal stability in which the polymer mass remains nearly constant. This behavior demonstrates that PVA retains its chemical integrity without significant decomposition, highlighting its ability to withstand moderately high temperatures prior to molecular chain scission [111, 110].

Beyond this point, in Region II (RII), the polymer undergoes its main thermal degradation, resulting in a total mass loss of approximately 89.1%. Three distinct degradation peaks are identified at 330 °C, 437 °C, and 558 °C. The first event, at around 330 °C, is attributed to the elimination of hydroxyl (O–H) side groups and the initial scission of the polymer backbone, primarily involving the cleavage of C–O and selected C–C bonds [153, 154]. This stage is also associated with dehydration and partial oxidation reactions, leading to the formation of unsaturated bonds and carbonyl (C=O) groups along the chains.

In Region III (RIII), the second degradation peak, observed at approximately 437 °C, corresponds to more extensive decomposition of the carbon backbone, marked by intensified rupture of C–C bonds and the breakdown of intermediate structures, including the carbonyl functionalities generated in earlier stages. The presence of C=O groups is indicative of oxidative degradation pathways, in which hydroxyl groups are progressively converted into carbonyl species.

Finally, the third peak at 558 °C represents the complete decomposition of residual carbonaceous structures, involving the rupture of the most stable C–C bonds. At 700 °C, the residual mass is approximately 0.1%, confirming the near-complete thermal degradation of the PVA membrane.

Figure 5.8 presents the TG and DSC curves of the PVA/LiOH membranes. As shown in Figure 5.8A), the thermal regions previously described are observed in all samples. In Region I, the mass loss is comparable among the membranes, mainly reflecting moisture evaporation. In Region II, however, the curves become progressively



distinct with increasing salt content, suggesting the emergence of structural ordering induced by LiOH. In contrast, in Region III, the degradation proceeds through sequential bond cleavage, leading to irregular thermal behavior and preventing the establishment of a consistent trend across the samples.

Figure 5.8B) present the heat flow data as a function of temperature obtained from DSC measurements. The glass transition temperature was determined as the midpoint of the heat flow change within the glass transition region, whereas  $T_m$  was identified as the minimum of the endothermic peak, following the exothermic-up convention. Both transitions indicate enhanced thermal properties, suggesting increased stability of the membranes. The enthalpy required to melt each sample was estimated from the intensity of the heat flow signal within the same thermogram[111, 155].

According to the literature [111],  $\Delta H_m$  corresponds to the enthalpy required for melting the sample, whereas  $\Delta H_m^\circ = 138.6$  J/g represents the enthalpy associated with the melting of fully crystalline PVA. The degree of crystallinity was calculated using Equation (1). Systematic errors in the determination of enthalpy and crystallinity are estimated to be below 3%. The results are summarized in Table 5.12.

Table 5.6: Glass transition, melting and decomposition temperatures, enthalpy ( $\Delta H_m$ ), and crystallinity ( $X_c$ ) of the PVA and PVA/LiOH samples.

PVA + X wt% LiClO <sub>4</sub>	$T_g$ (°C)	$T_m$ (°C)	$T_D$ (°C)	$\Delta H_m$ (J/g)	$X_c$ (%)
0%	77.9	195.9	297.1	18.9	13.6
1%	78.1	196.0	297.4	19.0	13.7
3%	80.9	196.2	297.9	19.1	13.9
5%	82.3	196.7	298.3	19.2	14.2
7%	84.2	197.1	298.7	19.3	14.5
9%	84.3	197.5	299.0	19.5	14.6

Although the absolute crystallinity values obtained from DSC differ from those measured by XRD due to the distinct underlying principles—DSC quantifies thermal transitions associated with melting enthalpy, whereas XRD evaluates the degree of structural order—the trends observed with increasing salt content in PVA membranes are consistent across both techniques. Consequently, despite the methodological differences and inherent limitations of each approach, the two techniques provide complementary insights, collectively confirming the structural evolution of the membranes

upon salt incorporation.

### 5.1.3 Impedance Spectroscopy Analysis of PVA/LiOH Membranes

This section presents the analysis of the electrical properties of polymer membranes. Complex impedance spectroscopy is a powerful technique that provides detailed insights into ionic conduction and relaxation phenomena, allowing the identification of limiting processes within the electrolyte. A clear understanding of these processes is crucial for optimizing membrane performance and guiding the development of more efficient solid-state electrolytes.

Figure 5.9 presents the Cole–Cole plots ( $Z'$  vs  $-Z''$ ) obtained from CIS measurements of pure PVA and PVA/LiOH membranes. The impedance response was measured at room temperature (300 K) over the frequency range of 10 Hz to 1 MHz, allowing the evaluation of the AC transport behavior of the membranes.

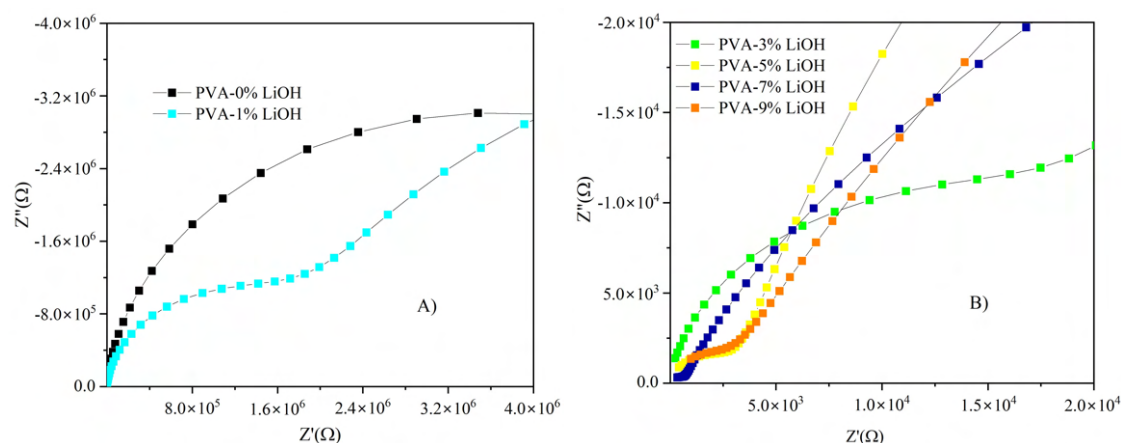


Figure 5.9: Cole–Cole plots for PVA-based membranes containing different LiOH concentrations. It is revealing a progressive decrease in bulk resistance.

For the pure PVA membrane, the conduction process is represented by the characteristic semicircle, which is incomplete at lower frequencies, indicating a high bulk resistance ( $R_b$ ) and, consequently, an electrically insulating response [156, 157, 55]. The observed semicircle reflects the structural response of the polymer matrix to the applied alternating electric field. The bulk resistance in these materials is typically high due to the lack of mobile charge carriers and the inherently insulating nature of the polymer, which limits charge transport [158, 115]. Furthermore, the segmental mobility of the polymer chains may be constrained by molecular entanglement and the

presence of semicrystalline domains. These structural restrictions result in a depressed semicircle, indicative of non-ideal and heterogeneous dielectric behavior associated with the internal organization of the polymer matrix.

In the PVA-1% sample, a linear region appears at low frequencies, commonly attributed to interfacial effects, reflecting structural or kinetic limitations within the membrane. In CIS, it is intrinsic for blocking behavior to occur at the electrode/electrolyte interface, since no faradaic reactions take place and only ionic displacement contributes to the measured signal. Under these conditions, the interface behaves as a capacitive element, which ideally would produce a vertical line in the Cole-Cole plot. However, the observed inclined tail below  $90^\circ$  indicates a non-ideal capacitive response, often caused by surface roughness or interfacial heterogeneity, resulting in distributed relaxation times and charge accumulation effects [159, 160, 161].

Still in the PVA-1% result,  $R_b$  reflects the primary ionic conduction pathway within the polymer matrix. Increasing the lithium salt concentration provides a greater number of mobile ions, thereby reducing the bulk resistance. The polymer's structure also influences the ease of ion transport, affecting the overall electrical properties.

Consequently, for PVA membranes doped with 3%, 5%, and 7% LiOH, the bulk resistance decreases, indicating enhanced ionic mobility and conductivity. This improvement arises because the added ions facilitate charge transport [162]. However, the high concentration of ions in the host polymer produces numerous unpaired ions that do not interact effectively with the polymer chains. As a result, during ionic transport, the relaxation of the segmental motion of the polymer chains is impeded by these unpaired ions [163]. When the LiOH concentration exceeds 9%, this effect is intensified, further restricting polymer chain mobility and causing an increase in  $R_b$ , thereby reversing the previous trend. In the impedance spectra, a second semicircle appears at low frequencies, overlapping with the linear tail, and is attributed to the membrane-electrode interface [164]. Due to the overlap of multiple impedance effects in the spectra, accurately determining the bulk resistance required fitting the Cole-Cole plots using an equivalent circuit model. This approach allowed proper separation of the bulk contribution from other interfacial processes.

The impedance data were analyzed using the ZView software. To properly represent this behavior of Pure PVA membrane, the data were fitted using an equivalent circuit consisting a series resistor ( $R_1$ , representing the ohmic resistance  $R_s$ ) and a

constant phase element ( $CPE_1$ ) in parallel, the  $CPE_1$  models the non-ideal capacitive behavior of the bulk polymer.

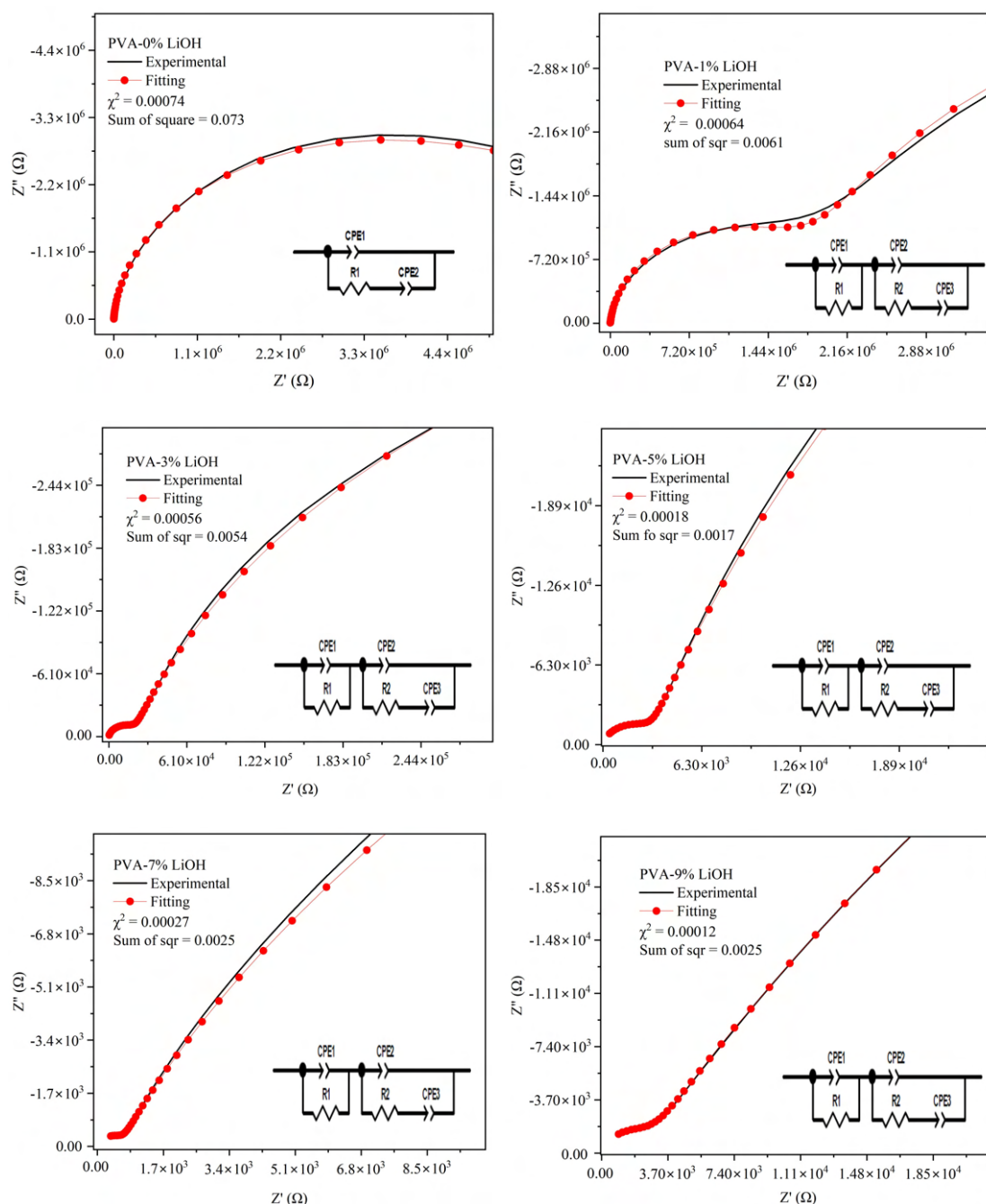


Figure 5.10: Cole–Cole plots were fitted using the ECM. Chi-square and sum of squares statistics are provided to evaluate the accuracy and reliability of the model fits.

To accurately describe the impedance response of the pure PVA membrane with lithium incorporation, the experimental data were fitted using a two-part equivalent cir-

cuit model. In the high-frequency region, the semicircle was represented by a parallel combination of a resistor and a constant phase element (CPE), reflecting the reduced bulk resistance and the non-ideal capacitive behavior of the polymer matrix, as previously discussed. In the low-frequency region, a more complex Randles-type equivalent circuit was applied to model the semicircle overlapping with the capacitive spike. This configuration comprises a second CPE ( $CPE_2$ ) in parallel with a series combination of a resistor ( $R_2$ ) and a third CPE ( $CPE_3$ ). This modeling strategy allows a clear distinction between bulk conduction phenomena and interfacial processes, providing a comprehensive understanding of the impedance characteristics.

The equivalent circuit model was fitted to the experimental CIS data using a non-linear least-squares procedure. The quality of the fit was assessed via the reduced chi-square ( $\chi^2$ ) statistic, as defined in Equation 4.9, considering both the real and imaginary components of the impedance. The maximum obtained chi-square value of 0.00074 indicates an excellent agreement between the equivalent circuit model and the experimental impedance data, demonstrating that the model accurately represents the electrochemical behavior of the system within the measurement uncertainties. The generally low  $\chi^2$  values observed in *ZView* arise because the metric is based on absolute squared differences in impedance (expressed in ohms squared), which are inherently small. Such low values are expected when the experimental data exhibit minimal noise, the model is physically meaningful, and the fitting procedure is accurate and stable.

When comparing the values of the table 5.7 the CPE1 parameters of the samples, it is observed that the pure PVA exhibits a  $P$  value of 0.96, very close to the behavior of an ideal capacitor, indicating a highly homogeneous response in the high-frequency region, associated with conduction within the membrane bulk. In contrast, the PVA sample with 7% LiOH shows a lower CPE1- $P$  value of 0.88, suggesting a more dispersive capacitive response, likely due to heterogeneities introduced by salt addition. Regarding the CPE1- $T$  parameter, the doped sample exhibits a value of  $1.50 \times 10^{-9}$ , which is nearly two orders of magnitude higher than the pure PVA value of  $7.56 \times 10^{-11}$ . This significant increase indicates an enhanced effective capacitance in the bulk region of the membrane, reflecting a higher charge storage capacity likely related to increased ionic mobility and interaction with the polymer matrix.

Table 5.7: Electrical circuit elements and their corresponding fitted values obtained from the CIS analysis of PVA and PVA-7% LiOH membranes.

Membrane	Element	Value	Error (%)
PVA	CPE1-T	$7.56 \times 10^{-11}$	1.08
	CPE1-P	0.96	0.09
	R1	$3.41 \times 10^6$	1.69
PVA-7% LiOH	CPE1-T	$1.50 \times 10^{-9}$	0.06
	CPE1-P	0.88	0.12
	R1	$5.95 \times 10^2$	1.42
	CPE2-T	$8.85 \times 10^{-8}$	4.45
	CPE2-P	0.75	0.86
	R2	$3.53 \times 10^4$	1.88
	CPE3-T	$1.14 \times 10^{-6}$	5.22
	CPE3-P	0.45	3.00

Table 5.8: Bulk resistance ( $R_b$ ) and calculated DC conductivity ( $\sigma_{DC}$ ) for PVA-based membranes with different LiOH contents.

Sample	$R_b$ ( $\Omega$ )	$\sigma_{DC}$ (S/cm)
PVA	$3.41 \times 10^6$	$1.53 \times 10^{-9}$
PVA-1% LiOH	$1.72 \times 10^6$	$2.98 \times 10^{-9}$
PVA-3% LiOH	$1.91 \times 10^4$	$1.51 \times 10^{-7}$
PVA-5% LiOH	$2.88 \times 10^3$	$1.54 \times 10^{-6}$
PVA-7% LiOH	$5.95 \times 10^2$	$1.02 \times 10^{-6}$
PVA-9% LiOH	$2.21 \times 10^3$	$2.52 \times 10^{-6}$

Furthermore, the  $R_1$  values support this interpretation: pure PVA exhibits a very high resistance of  $3.41 \times 10^6 \Omega$ , while the doped membrane exhibits a substantially lower resistance of  $5.95 \times 10^2 \Omega$ . This reduction of more than three orders of magnitude evidences improvement in ionic conduction, directly impacting the impedance

response. Therefore, despite a slight compromise in capacitive ideality, the overall impedance behavior is markedly enhanced by the presence of lithium salt. In the table 5.8 is presented the  $R_b$  of each sample and then the  $\sigma_{DC}$ , confirming that the sample with best impedance result is PVA-7% LiOH.

The CPE3-P value of 0.45, with variations between 0.45 and 0.60 observed in other samples, indicates non-ideal capacitive behavior. These values are consistent with literature reports on lithium-doped polymer electrolytes, supporting the interpretation of interfacial polarization at low frequencies [164].

The electric modulus formalism is widely used because it emphasizes ionic transport processes within the material, minimizing the influence of electrode polarization effects. The analysis of the imaginary part of the modulus is preferred, as it exhibits well-defined peaks that facilitate the interpretation of the observed phenomena. Accordingly, the imaginary electric modulus spectrum is analyzed, which proves more suitable than the real part by displaying such peaks, as shown in Figure 5.12. These peaks are fitted using equation 4.12 of the Havriliak-Negami model, allowing the determination of the parameters  $\alpha$ ,  $\beta$ , and the characteristic relaxation time of the system. The Havriliak-Negami model is a widely used empirical function to describe complex relaxation behaviors in polymers and heterogeneous materials. By adjusting the shape parameters  $\alpha$  and  $\beta$ , it can account for symmetric and asymmetric broadening of relaxation peaks, thus capturing a wide distribution of relaxation times beyond the classical Debye model.

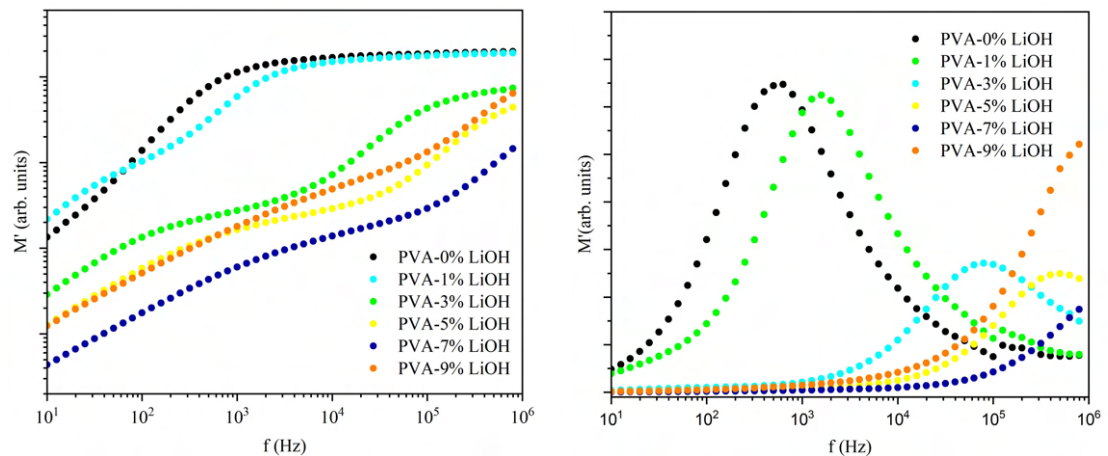


Figure 5.11: Real and imaginary spectra of the electrical modulus.

The Havriliak-Negami model parameters  $\alpha \approx 0.9$  and  $\beta \approx 0.55$  obtained for the PVA samples doped with varying concentrations of LiOH reveal a relaxation behav-

ior characterized by a predominantly symmetric, yet notably asymmetric distribution of relaxation times. The  $\alpha$  value, close to unity, suggests that the main relaxation mechanism is relatively uniform across the samples, indicative of consistent molecular dynamics within the polymer matrix. Conversely, the reduced  $\beta$  value reflects a pronounced broadening and skewness of the relaxation peak, evidencing complex interactions between the lithium salt and the polymer chains. These properties are typical of doped polymeric systems where local heterogeneities arise from salt-polymer interactions, leading to non-ideal relaxation dynamics.

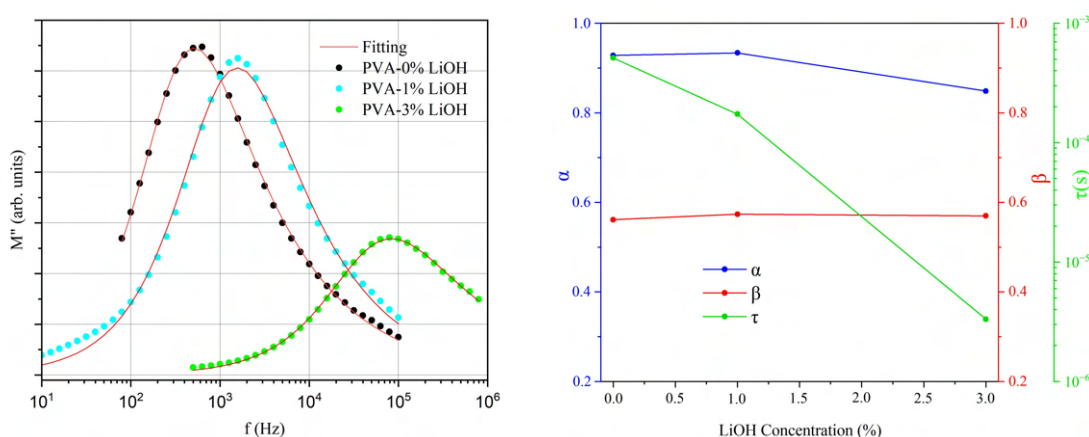


Figure 5.12: Imaginary part of the electrical modulus fitted by the Havriliak-Negami (HN) model, with parameters  $\alpha_{\text{HN}}$ ,  $\beta_{\text{HN}}$ , and relaxation time  $\tau_{\text{HN}}$ .

The incorporation of lithium salt into the PVA matrix results in increased ionic concentration and mobility, which considerably reduces the characteristic relaxation time  $\tau$ . For the samples containing 0%, 1%, and 3% LiOH,  $\tau$  decreases from approximately  $10^{-3}$  to  $10^{-5}$  s, indicative of accelerated ionic relaxation processes attributable to enhanced ion transport and polymer-salt interactions. This effect is observed as a shift of the imaginary electric modulus ( $M''_{\text{elec}}$ ) peaks toward higher frequencies, signifying a more rapid response of the system to the applied electric field and improved ionic conduction within the membrane [165, 166]. Samples with higher LiOH concentrations (5%, 7%, and 9%) exhibit relaxation times beyond the measurable spectral window, precluding precise quantification but suggesting further acceleration of relaxation dynamics. Collectively, these findings corroborate the increasing complexity and heterogeneity of the relaxation phenomena with rising salt content, as delineated by the Havriliak-Negami parameters.



Figure 5.13 presents the conductivity spectra of PVA membranes containing varying proportions of LiOH, along with the fittings performed across three distinct frequency regions. The data were analyzed using the complete Jonscher's equation 3.11(Model 1) and a simplified version considering only the AC conductivity term 4.10(Model 2). Both models were applied to each sample and frequency range, and the resulting parameter values, along with the corresponding fitting errors for the best-fitting model in each case, are summarized in the following table.

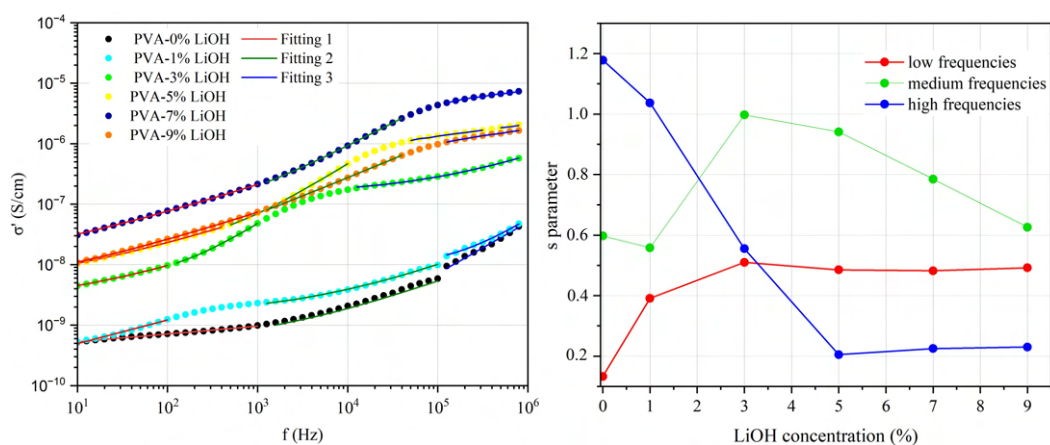


Figure 5.13: Conductivity spectra fitted by Jonscher's power law for low, medium and high range frequencies.

Firstly, no DC conductivity plateau was observed in any of the analyzed frequency ranges. This absence may arise from several factors. One possibility is the limitation of the accessible frequency window, where the plateau might occur at lower frequencies beyond the measurement range. Additionally, electrode polarization effects, which dominate the low- and intermediate-frequency regions, could mask the plateau. This interpretation is supported by the frequency-dependent exponent  $s$ , which varies from approximately 0.4–0.5 at low frequencies to 0.5–1.0 at intermediate frequencies, indicating dispersive ionic transport rather than steady-state conduction. Notably,  $s$  values in the intermediate frequency range (typically 0.5–0.8) are commonly associated with effective ionic conduction via hopping mechanisms, suggesting that, even in the absence of a visible DC plateau, significant frequency-dependent ionic mobility is present, likely facilitated by the segmental dynamics of the polymer matrix.

Although a low-frequency exponent of  $s \approx 0.2$  was observed at high frequencies, the substantial decrease in  $R_b$  seen in the Cole-Cole plots, along with the shift of peaks to higher frequencies in the imaginary electric modulus spectra, confirms enhanced

ionic mobility. The low  $s$  value reflects localized, dispersive ionic motions dominating at high frequencies, while overall ion transport and bulk conductivity improve due to the incorporation of lithium salt.

Table 5.9: Values of  $s$ ,  $R$ , and  $\chi$  parameters and their respective errors for different frequency ranges, obtained by fitting the conductivity data using Jonscher's model.

<b>Low Frequency</b>								
Sample	Model	$s$	$\Delta s$	$\Delta s$ (%)	$R$	$\Delta R$	$\Delta R$ (%)	$\chi$
LIOH0	model 2	0.133	0.004	2.65	0.9938	0.0734	7.38	2.06e-13
LIOH1	model 2	0.391	0.013	3.30	0.9911	0.0879	8.87	3.65e-12
LIOH3	model 1	0.510	0.021	4.07	0.9997	0.0171	1.71	7.24e-13
LIOH5	model 1	0.485	0.010	2.11	0.9997	0.0129	1.29	1.12e-11
LIOH7	model 1	0.482	0.008	1.64	0.9997	0.0120	1.20	1.15e-10
LIOH9	model 1	0.492	0.005	1.00	0.9999	0.0074	0.74	1.63e-11
LIOH10	model 1	0.416	0.004	0.97	0.9999	0.0052	0.52	6.60e-12
<b>Intermediate Frequency</b>								
Sample	Model	$s$	$\Delta s$	$\Delta s$ (%)	$R$	$\Delta R$	$\Delta R$ (%)	$\chi$
LIOH0	model 1	0.597	0.005	0.82	0.9998	0.0081	0.81	7.52e-13
LIOH1	model 1	0.558	0.020	3.57	0.9982	0.0279	2.80	1.60e-11
LIOH3	model 1	0.997	0.011	1.12	0.9999	0.0076	0.76	1.71e-12
LIOH5	model 1	0.941	0.013	1.36	0.9998	0.0117	1.17	1.30e-10
LIOH7	model 1	0.785	0.011	1.44	0.9997	0.0121	1.21	1.11e-09
LIOH9	model 1	0.626	0.010	1.59	0.9998	0.0114	1.14	2.26e-10
LIOH10	model 1	0.802	0.006	0.78	0.9999	0.0061	0.61	1.10e-10
<b>High Frequency</b>								
Sample	Model	$s$	$\Delta s$	$\Delta s$ (%)	$R$	$\Delta R$	$\Delta R$ (%)	$\chi$
LIOH0	model 1	1.178	0.074	6.27	0.9983	0.0438	4.38	5.89e-11
LIOH1	model 1	1.037	0.078	7.48	0.9980	0.0474	4.74	4.99e-11
LIOH3	model 1	0.555	0.019	3.47	0.9986	0.0260	2.60	5.36e-10
LIOH5	model 2	0.205	0.003	1.54	0.9975	0.0425	4.26	7.77e-10
LIOH7	model 2	0.225	0.007	3.22	0.9930	0.0885	8.91	3.86e-09
LIOH9	model 2	0.230	0.006	2.71	0.9950	0.0748	7.52	6.28e-10
LIOH10	model 2	0.226	0.009	3.87	0.9900	0.1055	10.65	5.68e-09

## 5.2 PVA/LiClO<sub>4</sub> membranes

### 5.2.1 Investigation of Structural and Morphological Aspects by Spectroscopic, Crystallographic, and Microscopic Analyses

Figure 5.14A) displays the FT-IR transmittance spectra of the samples measured within the 4000–650  $\text{cm}^{-1}$  wavenumber range. The key absorption bands associated with O–H, C–H, C=O, and C–O vibrational modes are indicated.

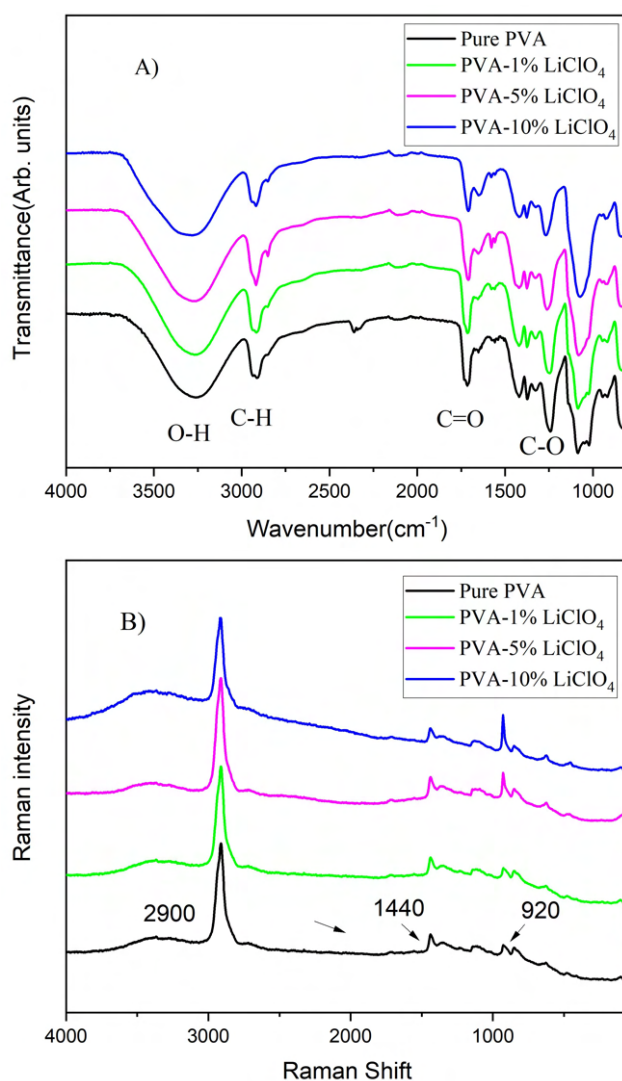


Figure 5.14: Transmittance and Raman intensities of PVA/LiClO<sub>4</sub>.

The incorporation of LiClO<sub>4</sub> into the PVA matrix does not lead to the appearance of new bands in the FT-IR and Raman spectra, indicating that Li<sup>+</sup> ions do not form covalent bonds with either the semi-crystalline or amorphous regions of the polymer. The C=O stretching band at 1709  $\text{cm}^{-1}$ , corresponding to residual acetate groups, remains

unaltered, confirming that the carbon–oxygen double bond is intact and no conversion to carboxylate species occurs. This behavior is attributed to the high stability and weak nucleophilicity of perchlorate ions ( $\text{ClO}_4^-$ ), which lack the basicity necessary to induce hydrolysis or chemical modification of the polymer's functional groups. The absence of the band at  $1550\text{ cm}^{-1}$ , characteristic of asymmetric carboxylate stretching, further corroborates this interpretation. Additionally, the increased intensity of the C–H stretching band upon the addition of 5%  $\text{LiClO}_4$  likely reflects local polymer chain reorganization or enhanced polarization of these bonds by  $\text{Li}^+$  ions, without implying significant chemical modification of the polymer backbone.

The  $\text{ClO}_4^-$  ion primarily acts as a charge-neutralizing agent for the positive  $\text{Li}^+$  cation when it coordinates with the oxygen atoms of the PVA chain. While  $\text{ClO}_4^-$  does not strongly interact directly with the chemical structure of the polymer, its presence is essential for maintaining electroneutrality and stabilizing the ionic environment within the matrix.

Figure 5.15 presents the normalized PXRD patterns of pure PVA powder, crystalline  $\text{LiClO}_4$ , and PVA membranes containing 1, 5, and 10 wt%  $\text{LiClO}_4$ . The characteristic diffraction peaks of crystalline  $\text{LiClO}_4$  are absent in the PXRD profiles of the post-synthesis membranes, indicating that the salt is fully dissociated during membrane formation. Visual inspection of the diffraction data also reveals subtle changes in the polymer structure as a function of  $\text{LiClO}_4$  concentration.

Our findings indicate notable differences in the quality of the XRD patterns. The powder sample exhibited sharper and more defined diffraction peaks, whereas the membrane showed broader peaks accompanied by an elevated diffraction background. This difference arises from structural reorganization during membrane preparation: the dissolution, casting, and drying steps disrupt the original semicrystalline arrangement of PVA chains, leading to reduced crystallinity and an increase in amorphous character.

The results indicate that at 1%, there is no discernible change in the PVA structure. However, when the content is increased to 5%, a noticeable reduction in the diffuse XRD occurs, as shown in Figure 5.15B). In other words, the background intensity decreases to approximately 5%, indicating an enhancement in crystallinity. This suggests an improvement in the efficiency of PVA polymerization. However, when the concentration surpasses 10%, there appears to be an inhibitory effect on PVA polymerization. Notably, the principal XRD peak (around  $2\theta = 20^\circ$ ) corresponding to the PVA

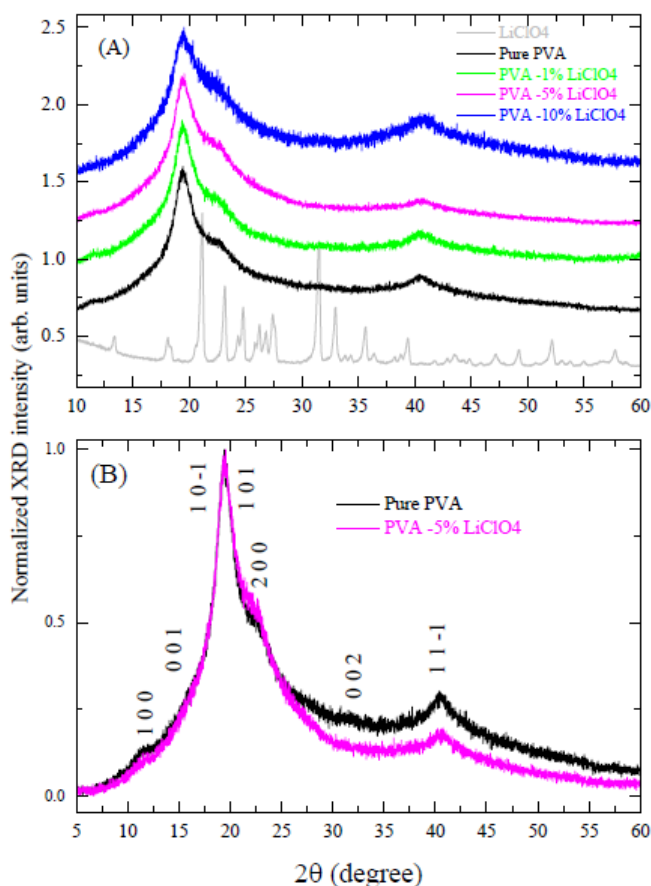


Figure 5.15: A) XRD patterns and B) Comparison of background intensities for different compositions.

10%- sample is relatively smaller compared to the other samples.

Figures 5.16A), B), C), and D) display the XRD patterns obtained after Rietveld refinement, considering the  $P2_1/m$  space group for different LiClO<sub>4</sub> concentrations (1wt%, 5wt%, and 10wt%). The refinement process effectively converged to match the experimental data. The resulting unit cell parameters and calculated crystalline content (%) are presented in Table.

The Rietveld refinement of the PVA pattern yielded a chi-square value below 2%, indicating an excellent agreement between the structural model and the experimental data. This result demonstrates that the semicrystalline/amorphous structure of the polymer is well represented, despite the inherent challenges associated with the analysis of polymeric materials, which typically exhibit broad and less defined peaks.

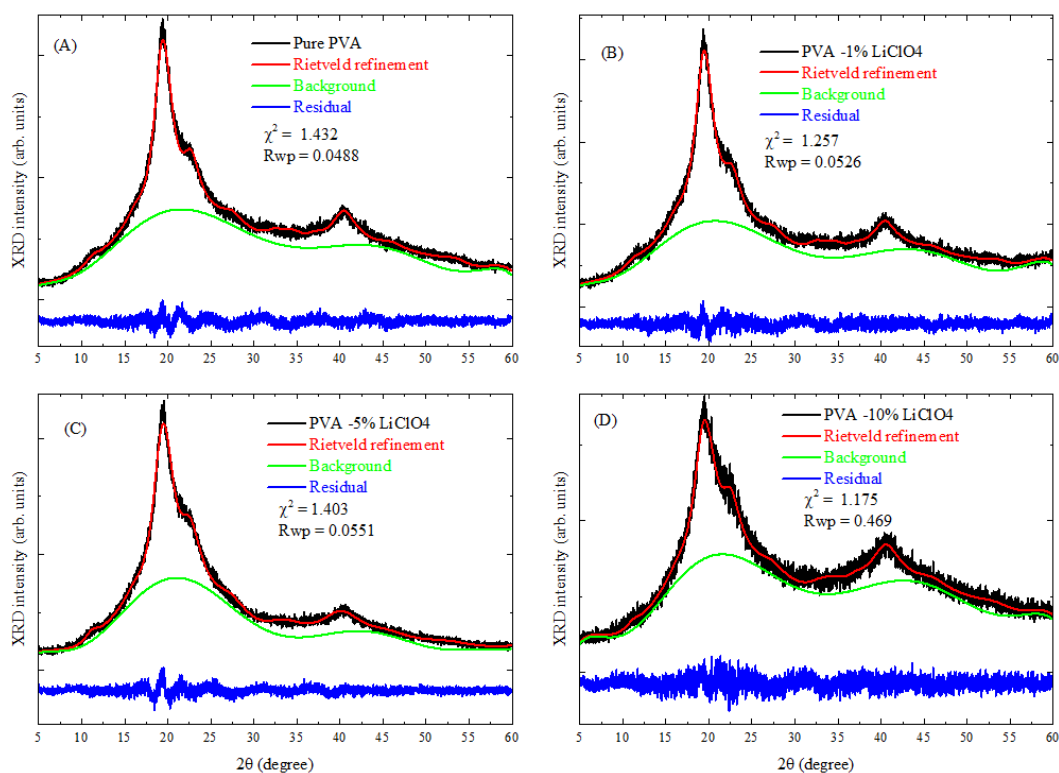


Figure 5.16: Rietveld structural refinements at different  $\text{LiClO}_4$  concentrations. Background and residual curves illustrate the semicrystalline/amorphous nature of the samples.

Table 5.10: Lattice parameters  $a$ ,  $b$ , and  $c$ , monoclinic angle  $\beta$ , and unit cell volume of PVA/ $\text{LiClO}_4$  composites, determined through Rietveld refinement analysis, alongside their corresponding crystallinity indices. .

Sample	$a$ (Å)	$b$ (Å)	$c$ (Å)	$\beta$ (°)	$V$ (Å <sup>3</sup> )	$x_c$ (%)
Pure PVA	7.832(5)	2.549(2)	5.512(7)	92.35(9)	109.9(1)	28.3
1 wt%	7.837(6)	2.554(2)	5.516(4)	92.06(9)	110.4(2)	27.6
5 wt%	7.882(2)	2.582(5)	5.523(3)	91.90(10)	112.3(2)	30.2
10 wt%	7.896(8)	2.545(3)	5.484(6)	92.60(10)	110.1(2)	21.3

In Figure 5.17, the morphologies of polymer membranes with 0%, 1%, 5%, and 10%  $\text{LiClO}_4$  incorporated into the PVA matrix are presented. The images were acquired with a working distance (WD) ranging from approximately 9.5 to 10.1 mm and a SEM magnification between 3x and 5x.

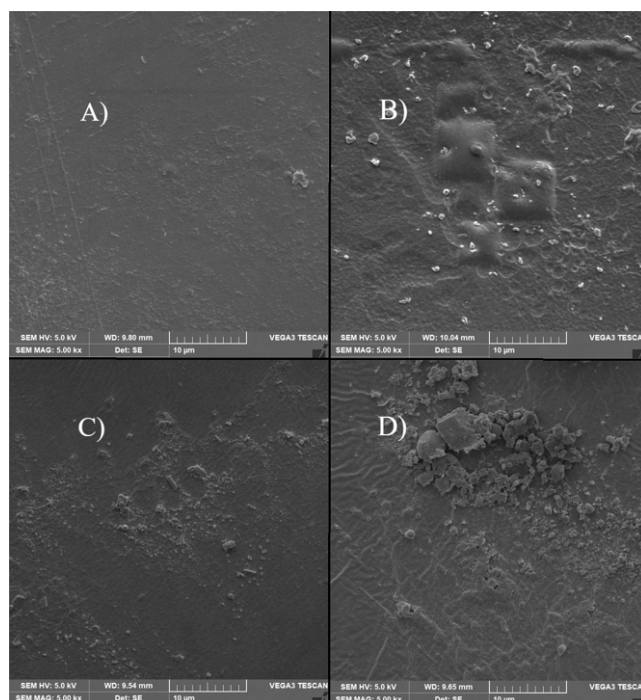


Figure 5.17: Surface morphologies of polymer membranes with the addition of 1% B), 5% C), and 10% D)  $\text{LiClO}_4$  in PVA.

During the drying process, perchlorate ions ( $\text{ClO}_4^-$ ) can migrate and accumulate locally within the PVA matrix, particularly at higher salt concentrations. This ionic redistribution significantly affects the membrane morphology, promoting the formation of amorphous agglomerates, increased surface roughness, and, in some cases, micro-cracks. These morphological changes are primarily caused by internal stresses resulting from uneven solvent evaporation and the disruption of intermolecular hydrogen bonding within the polymer chains. As the  $\text{LiClO}_4$  concentration rises up to 10%, the number and size of agglomerates increase, leading to pronounced roughness and ionic segregation in the host polymer matrix. Such heterogeneities may negatively impact the mechanical integrity and structural properties of the membranes, as corroborated by XRD analysis.

Table 5.11 presents the elemental composition of pure PVA and PVA containing 10%  $\text{LiClO}_4$ . The detection of chlorine in the doped sample confirms salt incorporation, while variations in carbon, oxygen, and gold content reflect the effects of  $\text{LiClO}_4$  addition on the polymer matrix.

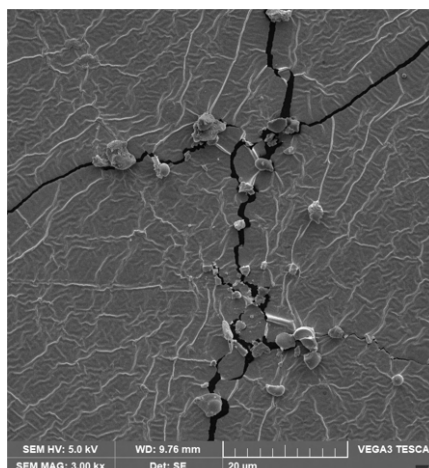


Figure 5.18: Surface image of PVA membrane containing 10% LiClO<sub>4</sub>, showing the presence of cracks attributed to the high concentration of lithium salt.

Table 5.11: Elemental composition by EDS – Comparison between PVA sample and PVA with 10% LiClO<sub>4</sub>.

Element	PVA (Wt% $\pm\sigma_{\text{EDS}}$ )	10% LiClO <sub>4</sub> (Wt% $\pm\sigma_{\text{EDS}}$ )
C	59.9 $\pm$ 0.9	45.2 $\pm$ 1.5
O	29.4 $\pm$ 0.9	30.5 $\pm$ 1.2
Au	10.7 $\pm$ 0.6	18.2 $\pm$ 0.9
Cl	–	5.2 $\pm$ 0.3

## 5.2.2 Thermal Evaluation Using Thermogravimetric and Calorimetric Techniques.

In Figure 5.19B), the weight loss curves for pure PVA and PVA/LiClO<sub>4</sub> samples are presented. The addition of 5% LiClO<sub>4</sub> to PVA leads to a more defined weight loss, indicating a more uniform thermal behavior. This effect is associated with the increased crystallinity promoted by the salt, which enhances molecular ordering and favors a more synchronized decomposition of the polymer chains. Additionally, coordination between Li<sup>+</sup> ions and hydroxyl groups may contribute to denser chain packing, further reinforcing this structural organization. At 10% LiClO<sub>4</sub>, the mass loss during thermal degradation becomes more pronounced and occurs over a narrower temperature range, indicating a faster and more distinct decomposition process. This behavior may result from surpassing a critical threshold in salt concentration, where enhanced polymer chain mobility and disruption of intermolecular interactions accelerate ther-



mal degradation. Consequently,  $\text{LiClO}_4$  not only modifies the structural organization of the polymer but also facilitates thermal breakdown, reducing the overall thermal stability of the membrane.

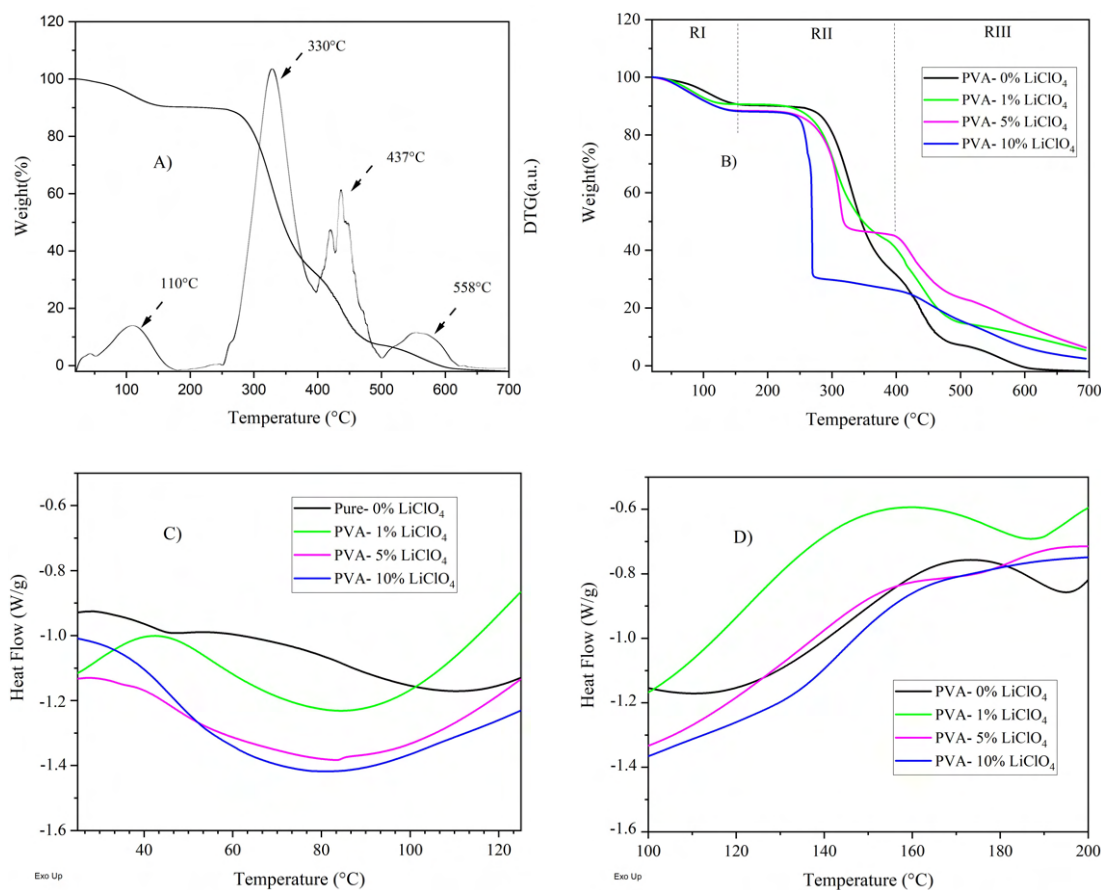


Figure 5.19: Weight loss and DTG data of the pure PVA membrane A); comparison between pure PVA and PVA/ $\text{LiClO}_4$  membranes B); and heat flow data in two different temperature ranges: 10 °C to 120 °C, C) and 100 °C to 200 °C, D).

The residual percentage of each sample are 7.2%, 7% and 4% for PVA-1% $\text{LiClO}_4$ , PVA-5% $\text{LiClO}_4$ , and PVA-10% $\text{LiClO}_4$ , respectively.

Figure 5.19C) and D) present the DSC heat flow curves as a function of temperature. The thermogram was divided into two regions: the first region was used to determine  $T_g$ , while the second region allowed identification of  $T_m$  and the enthalpy of fusion for each sample, based on the difference in heat flow intensities.

Table 5.12: Thermal properties ( $T_D$ ,  $\Delta H_m$ ) and crystallinity ( $X_c$ ) of the PVA and PVA/LiClO<sub>4</sub> samples.

PVA + X wt% LiClO <sub>4</sub>	$T_g$ (°C)	$T_m$ (°C)	$T_D$ (°C)	$\Delta H_m$ (J/g)	$X_c$ (%)
0%	77.9	195.9	297.1	18.9	13.6
1%	70.4	187.5	280.9	15.9	11.5
5%	84.2	175.2	298.7	19.5	14.1
10%	40.7	183.6	255.4	10.4	7.5

The thermal behavior of the PVA and PVA/LiClO<sub>4</sub> samples reveals distinct trends as a function of salt concentration. Pure PVA exhibits  $T_g$  of 77.9 °C, which is consistent with literature values. The addition of 5% LiClO<sub>4</sub> increases  $T_g$  to 84.2 °C, indicating restricted chain mobility, likely due to stronger interactions between Li<sup>+</sup> ions and hydroxyl groups along the polymer backbone. This coordination promotes enhanced molecular ordering, leading to the highest observed crystallinity (14.1%) and enthalpy of fusion (19.5 J/g) among all samples. Although  $T_m$  decreases slightly to 175.2 °C, the degradation temperature ( $T_D$ ) rises to 298.7 °C, suggesting improved thermal organization and stability in the semicrystalline regions.

In contrast, the sample containing 10% LiClO<sub>4</sub> exhibits a marked decrease in  $T_g$  to 40.7 °C and the lowest degree of crystallinity (7.5%), accompanied by a significant reduction in both  $T_m$  and  $T_D$ . This behavior can be attributed to excessive salt loading within the polymer matrix, in which the excess salt disrupts the polymer's structural organization and functions as a plasticizer, thereby increasing chain mobility and decreasing thermal stability. These findings indicate that 5% LiClO<sub>4</sub> represents an optimal concentration for enhancing the thermal and structural properties of the polymer, whereas higher salt contents lead to destabilization of the polymer chains.

### 5.2.3 Mechanical analysis

The mechanical characterization of polymeric membranes using DMA and tensile (stress–strain) testing is essential for evaluating their performance, particularly when applied as solid electrolytes in batteries. DMA provides valuable insights into viscoelastic properties, such as the storage modulus ( $M'_{\text{mech}}$ ) and loss modulus ( $M''_{\text{mech}}$ ), which are critical for ensuring dimensional stability under operating conditions. Ten-

sile testing, in turn, evaluates mechanical strength and flexibility, verifying the membrane's ability to withstand electrochemical stress while maintaining structural integrity and effective interfacial contact.

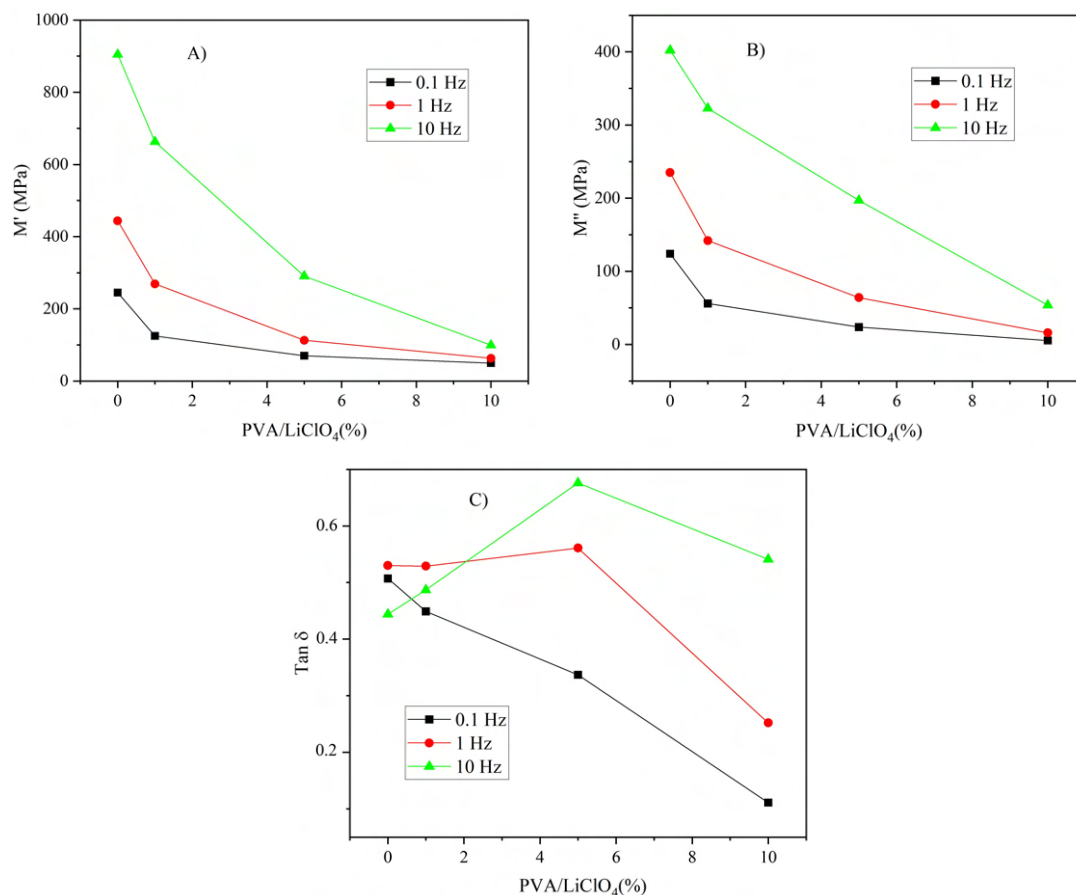


Figure 5.20: Frequency-dependent mechanical response of the material at different LiClO<sub>4</sub> concentrations: (A) real modulus  $M'_{\text{mech}}$ ; (B) imaginary modulus  $M''_{\text{mech}}$ ; (C) loss factor  $\tan \delta$ .

Figure 5.20 presents both  $M'_{\text{mech}}$  and  $M''_{\text{mech}}$  values at frequencies of 0.1, 1, and 10 Hz as a function of LiClO<sub>4</sub> concentration at room temperature. From Figure 5.20A), the  $M'$  value for the pure PVA sample reaches approximately 900 MPa at 10 Hz, which is consistent with values reported in the literature for dry PVA membranes with good mechanical integrity [167, 168, 169]. This elevated modulus arises from a dense polymer chain, where closer packing of chains enhances intermolecular hydrogen bonding, thus increasing rigidity and elastic energy storage. The storage modulus  $M'_{\text{mech}}$  reflects the amount of elastic energy stored under mechanical loading and its frequency-dependent behavior is typical of viscoelastic materials. At higher frequencies, restricted molecular rearrangements result in a stiffer response and higher  $M'_{\text{mech}}$ ,

whereas at lower frequencies, greater molecular mobility leads to reduced stiffness. As shown,  $M'_{\text{mech}}$  decreases to 430 MPa and 220 MPa at lower frequencies and higher salt concentrations, suggesting that  $\text{LiClO}_4$  reduces intermolecular cohesion and thus the membrane's resistance to deformation.

In Figure 5.20B), the loss modulus  $M''_{\text{mech}}$  is plotted under similar conditions. The trends closely follow those of A), indicating that  $M''_{\text{mech}}$  arises from energy dissipation through internal molecular motions. It reflects the ability of the PVA chains to reconfigure in response to applied stress, highlighting the dynamic aspect of their viscoelastic behavior. Variations in  $M''_{\text{mech}}$  further reveal how structural modifications that affect the energy dissipation mechanisms within the membrane during mechanical deformation.

The elastic energy loss coefficient, commonly referred to as damping or internal friction, is a critical anelastic property measured by DMA. It quantifies the efficiency with which a material dissipates energy through molecular rearrangements. As shown in Figure 5.20C), this coefficient expressed as  $\tan \delta$ , the tangent of the phase angle  $\delta$  depends on both frequency and salt concentration [168, 169]. Variations in  $\tan \delta$  provide valuable insights into the material's capacity for energy dissipation and internal structural dynamics under mechanical stress.

The addition of 1%  $\text{LiClO}_4$  results in a negligible change in  $\tan \delta$  compared to pure PVA. In contrast, the membrane with 5%  $\text{LiClO}_4$  presents a marked increase, reaching a maximum  $\tan \delta$  of 0.68 at 10 Hz. This behavior causes greater mechanical energy dissipation, indicating increased polymer chain mobility in response to dynamic loading. Such an increase is often associated with a shift in the  $T_g$  to higher values, as observed in DSC analysis, suggesting improved thermal stability and a more dynamically responsive polymer chain.

In tensile test measurements, the applied stress ( $\sigma_{\text{mech}}$ ) is expressed in megapascals (MPa), while strain ( $\varepsilon_{\text{mech}}$ ) is a dimensionless ratio in mm/mm. For clarity, Figure 5.21 presents the results as strain percentages. In agreement with the DMA results, the pure PVA membrane exhibits high tensile strength, while the stress at failure decreases progressively with increasing  $\text{LiClO}_4$  content. This reduction is accompanied by an increase in strain capacity, with elongation at break reaching 300–350% of the original dimensions.

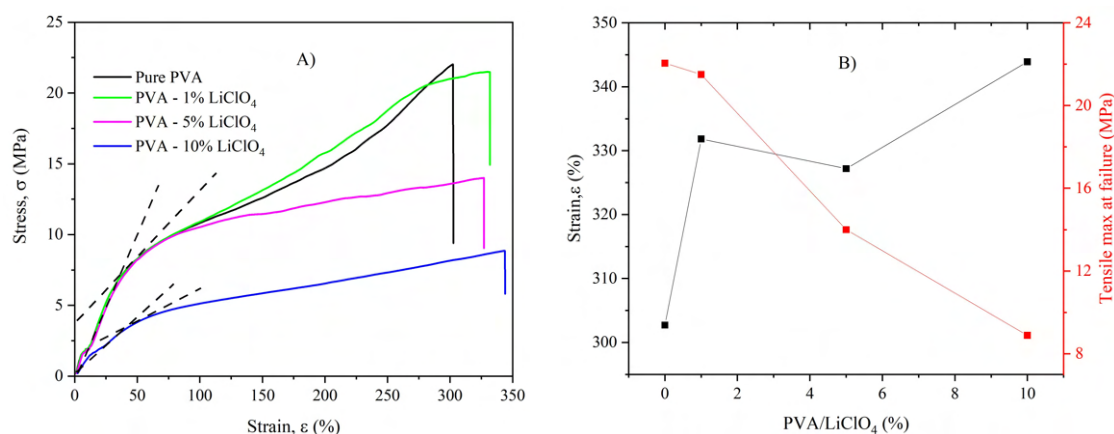


Figure 5.21: Strain–Stress and Tensile limit at failure. Transition between elastic and plastic behaviors are separated by dashed lines.

Figure 5.21B) illustrates the inverse relationship between strain at failure and maximum tensile stress, a typical property of polymeric membranes [170]. This correlation reflects the trade-off between stiffness and flexibility: as tensile strength increases, ductility decreases. Additionally, dashed lines in Figure 5.21A) indicate the transition between elastic and plastic behavior, clearly defined for pure PVA and for 1% and 5% LiClO<sub>4</sub> membranes, with greater deviation observed at 10%. The reduced mechanical performance at higher salt concentrations is likely due to structural disruption caused by LiClO<sub>4</sub> ions, which interfere with hydrogen bonding and increase free volume. These effects weaken chain interactions and compromise structural integrity, leading to lower strength and higher ductility, ultimately reducing mechanical robustness and long-term stability.

The column graph in Figure 5.22A) shows the Young's modulus ( $E$ ) as a function of LiClO<sub>4</sub> concentration. The addition of 1% LiClO<sub>4</sub> does not significantly alter  $E$  compared to pure PVA, while the membrane with 5% LiClO<sub>4</sub> presents a similar modulus despite not reaching the same maximum tensile stress. This indicates a structurally organized polymer matrix that resists deformation during the elastic phase, exhibiting a good balance between stiffness and adaptability. The onset of plasticity in this composition suggests the presence of elastic resistance followed by conformational adjustments of the polymer chains under stress.

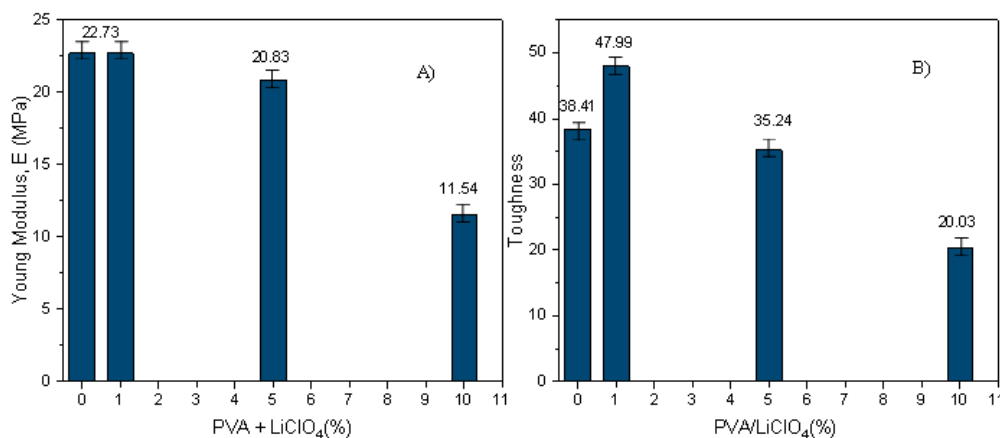


Figure 5.22: Calculated Young Modulus and Toughness.

Figure 5.22B) illustrates how toughness varies with salt concentration. The 1% LiClO<sub>4</sub> membrane presents the highest toughness, indicating it can deform more before rupture. In contrast, the 5% and 10% LiClO<sub>4</sub> membranes absorb less energy prior to failure. While both show increased strain capacity, the 5% membrane maintains a favorable mechanical balance, whereas the 10% membrane becomes structurally compromised and less able to resist applied stress. This suggests that excessive salt disrupts the polymer matrix, reducing energy absorption and overall mechanical robustness.

### 5.3 Electrical Characterization and Properties Based on CIS.

Figure 5.23 presents the Cole-Cole plots ( $Z'$  vs.  $-Z''$ ) derived from CIS measurements of both pure PVA and PVA/LiClO<sub>4</sub> membranes. The measurements were conducted aiming to evaluate the effect of lithium salt incorporation on the AC impedance behavior of the membranes.

For the pure PVA membrane, the impedance response exhibits an incomplete semi-circle at high frequencies, indicative of a high bulk resistance and an overall electrically insulating behavior. Consequently, the membrane shows poor ionic conductivity, limiting its practical applicability. The addition of LiClO<sub>4</sub> aims to enhance ionic conduction.

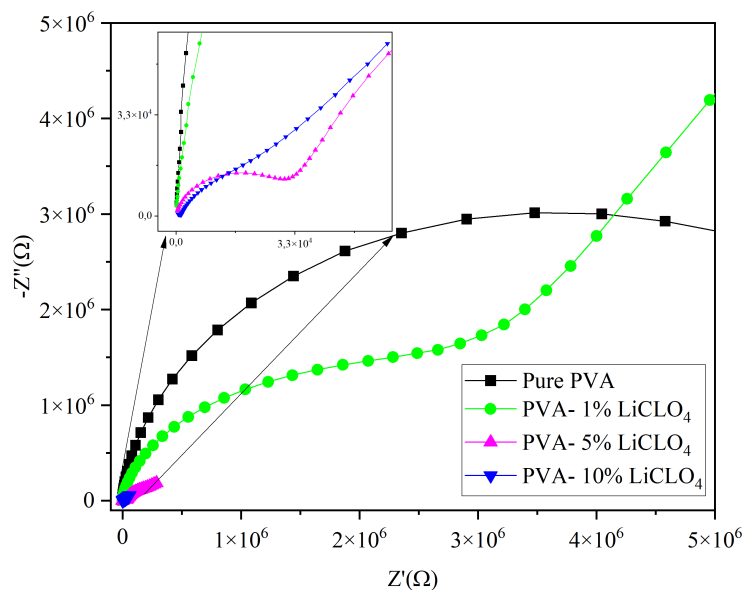


Figure 5.23: Cole-Cole fitting By Equivalent Circuit Model.

In the PVA-1% membrane, a linear region appears at low frequencies, indicative of electrode polarization effects. The bulk resistance represents the primary ionic conduction pathway within the polymer matrix, and its reduction with increasing lithium salt concentration reflects enhanced ion mobility due to a higher number of available charge carriers. For the PVA-5% and PVA-10% membranes, the continued decrease in  $R_b$  confirms that  $\text{LiClO}_4$  incorporation improves ionic conductivity. Since no increase in  $R_b$  is observed, this suggests that the salt concentration has not yet reached a saturation limit, and further conductivity improvements may be achieved. The linear tail at low frequencies, overlapping with the semicircle, is attributed to electrode polarization effects.

The impedance response of the pure PVA membrane with lithium addition was analyzed using the equivalent circuit model previously established for PVA/LiOH samples. In the high-frequency region, the impedance semicircle was represented by a parallel combination of a resistor and a CPE, capturing the decreased bulk resistance and the non-ideal capacitive behavior introduced by lithium ions. For the lower frequency range, the more intricate equivalent circuit described earlier was utilized to represent interfacial and polarization contributions. This approach allows a clear distinction between bulk ionic transport and electrode-related phenomena, enabling comprehensive interpretation of the measured impedance spectra.

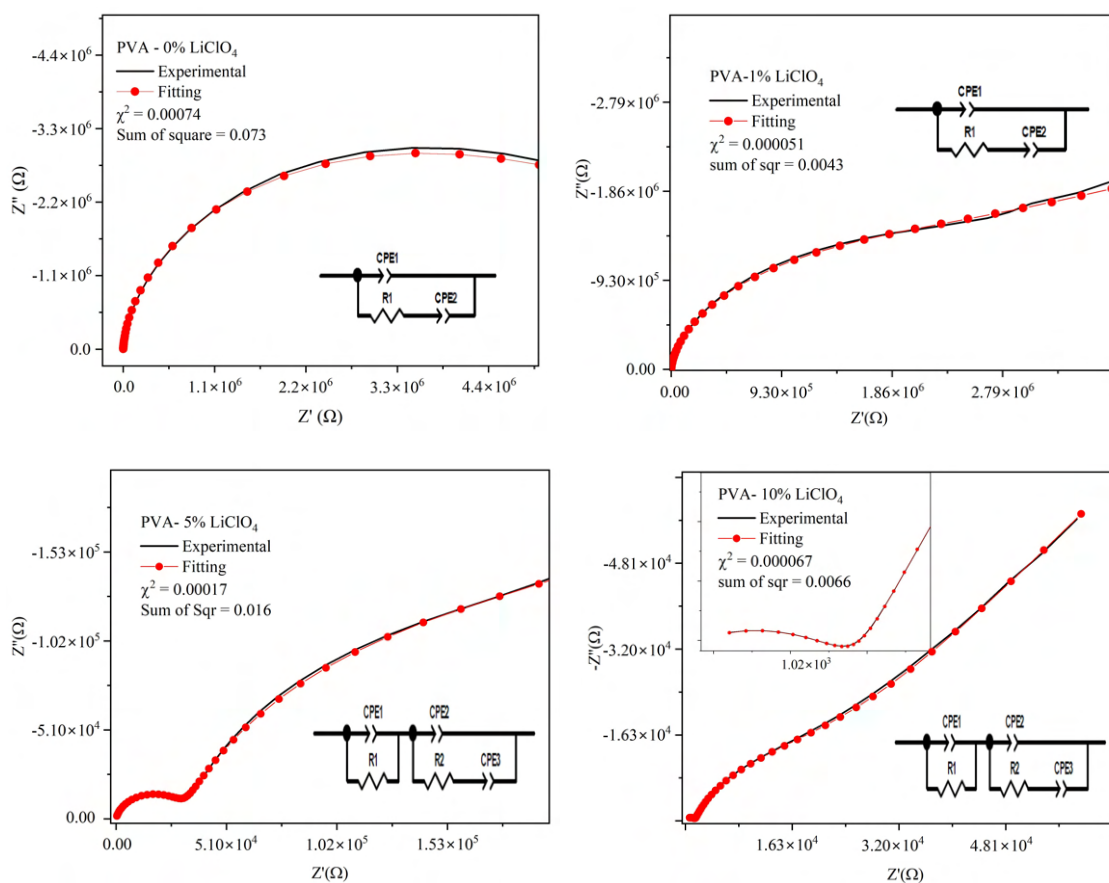


Figure 5.24: Cole–Cole plots for PVA-based polymer membranes containing different LiOH concentrations, showing a progressive decrease in bulk resistance.

The respective fitting values for each circuit element are presented in Table 5.13, with all error values below 5%, which is within the acceptable range for CIS measurements. The low cumulative error, reflected in the chi-square values shown in Figure 5.24, confirms both the reliability of the fitted parameters and the suitability of the chosen model for describing the system's impedance response.

The observed decrease in bulk resistance is directly associated with an increase in the DC conductivity of the membranes, thereby enhancing their ionic conduction efficiency. Consequently, the reduction in resistance with increasing  $\text{LiClO}_4$  content confirms the improved performance of the membranes.



Table 5.13: Electrical elements and their values from CIS fitting of PVA and PVA–LiClO<sub>4</sub> membranes.

Element	PVA	PVA–1% LiClO <sub>4</sub>	PVA–5% LiClO <sub>4</sub>	PVA–10% LiClO <sub>4</sub>
CPE1-T	$7.56 \times 10^{-11}$	$9.39 \times 10^{-11}$	$6.60 \times 10^{-10}$	$1.87 \times 10^{-9}$
CPE1-P	0.96	0.96	0.88	0.83
R1	$3.41 \times 10^6$	$3.33 \times 10^5$	$3.03 \times 10^4$	$1.42 \times 10^3$
CPE2-T	—	$5.41 \times 10^{-8}$	$3.93 \times 10^{-8}$	$8.34 \times 10^{-8}$
CPE2-P	—	0.26	0.78	0.81
R2	—	—	$2.99 \times 10^5$	$2.78 \times 10^4$
CPE3-T	—	—	$3.19 \times 10^{-7}$	$1.21 \times 10^{-6}$
CPE3-P	—	—	0.68	0.57

Table 5.14: Measured bulk resistance ( $R_b$ ) and corresponding DC conductivity ( $\sigma_{DC}$ ) values for PVA–LiClO<sub>4</sub> membranes.

Sample	$R_b$ ( $\Omega$ )	$\sigma_{DC}$ (S/cm)
PVA	$3.41 \times 10^6$	$1.53 \times 10^{-9}$
PVA–1% LiClO <sub>4</sub>	$3.33 \times 10^5$	$1.50 \times 10^{-8}$
PVA–5% LiClO <sub>4</sub>	$3.03 \times 10^4$	$1.51 \times 10^{-7}$
PVA–10% LiClO <sub>4</sub>	$1.42 \times 10^3$	$3.65 \times 10^{-6}$

The presence of a plateau in the high-frequency region of the real part of the electric modulus ( $M'_{\text{elec}}$ ) for the pure PVA and PVA–1% LiClO<sub>4</sub> membranes indicates a dielectric behavior typical of insulating materials, where fast relaxation mechanisms dominate and ionic conduction is limited. In contrast, the absence of this plateau in the PVA–5% and PVA–10% LiClO<sub>4</sub> membranes reveals a transition to a more conductive regime. In these cases, the material response remains active even at high frequencies, suggesting increased ionic mobility and a higher density of charge carriers.

The analysis of the imaginary part of the electric modulus ( $M''_{\text{elec}}$ ) complements this interpretation, as it exhibits well-defined peaks that allow the extraction of the system's characteristic relaxation times. These peaks are fitted using the Havriliak–Negami

(HN) model, enabling determination of the parameters  $\alpha$ ,  $\beta$ , and the relaxation times associated with the various ionic dynamics present in the membranes.

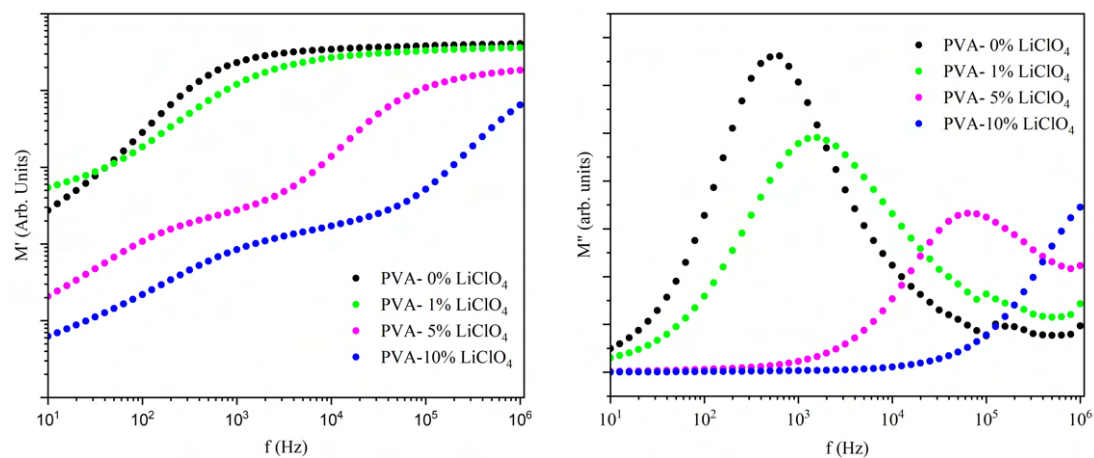


Figure 5.25: The real component of the electrical modulus indicates an insulating dielectric behavior for PVA and 1%  $\text{LiClO}_4$ , while the imaginary component shows a shift of the peaks toward higher frequencies.

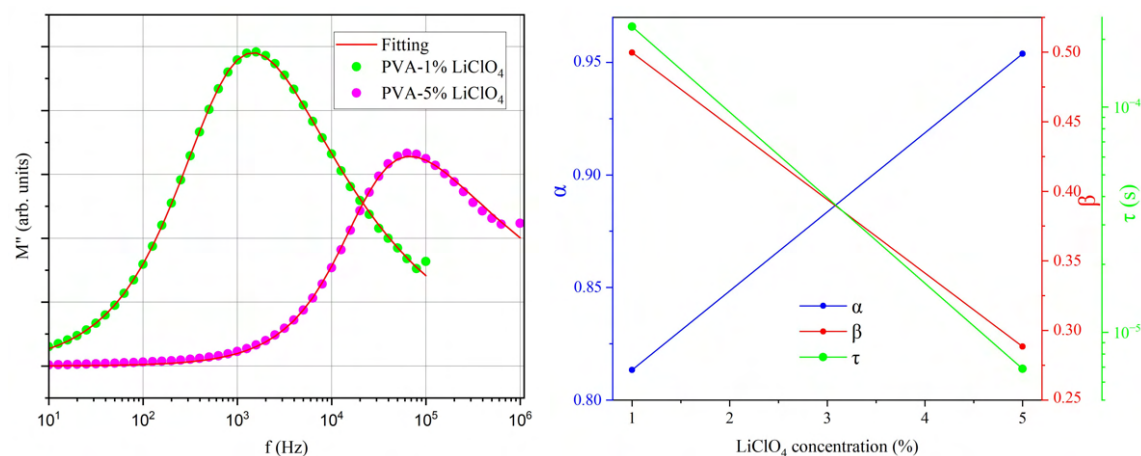


Figure 5.26: HN model fitting peaks and their parameters.

After analysis using the HN model, the parameter  $\alpha$  was found to range between 0.8 and 0.9, indicating relatively broad relaxation processes, yet still close to the ideal Debye behavior ( $\alpha = 1$ ). In contrast, the  $\beta$  parameter decreased from 0.5 to 0.3, suggesting that the relaxation peaks became increasingly asymmetric and dispersed as the salt concentration increased.

Furthermore, the characteristic relaxation time decreased from the order of  $10^{-3}$  s to  $10^{-5}$  s, indicating that the ionic relaxation processes became faster. This behavior

reflects a more efficient response of the mobile ions to the applied electric field as the concentration of  $\text{LiClO}_4$  increases.

## 5.4 Discussion and Contextualization of the results.

Considering the scope of this research, a critical parameter in the field of polymer-based electrolytes is the DC ionic conductivity. Table 5.15 presents the best results obtained in this study, along with a comparison to similar systems reported in the literature. In our case, the membrane containing LiOH exhibited a conductivity on the order of  $10^{-5}\text{S/cm}$ , whereas the membrane with  $\text{LiClO}_4$  reached approximately  $10^{-6}\text{S/cm}$ . Although Aji M. P. et al.[89] reported a higher conductivity, essential experimental details—such as the PVA molecular weight and sample dimensions—were not provided, precluding direct comparison. These observations support the reliability and reproducibility of the parameters reported in this thesis.

In addition, Gunawan et al. [86] provided results of comparable magnitude, particularly for samples doped with up to 20%  $\text{LiClO}_4$ , also reaching conductivities on the order of  $10^{-6}\text{S/cm}$ . However, in their study, the observed enhancement in conductivity was also attributed to a drastic reduction in crystallinity, reaching values below 10%. In contrast, our results demonstrate that significant improvements in ionic conductivity were achieved without compromising the structural ordering of the system. Both PVA/LiOH and PVA/ $\text{LiClO}_4$  membranes maintained relatively stable crystallinity levels, indicating that the increase in conductivity arises from factors beyond mere structural disorder. This distinction underscores the advantage of our approach, as it allows for conductivity enhancement while preserving the material's structural integrity.

Table 5.15 presents the PEO/PVA/LiOH composites. Despite the presence of PEO, which is known to enhance ionic conductivity, this system serves as a valuable reference for comparison. The improved conductivity observed in that work is attributed not only to the incorporation of LiOH and PEO, but also to the fact that the Mw of PVA used corresponds to the average molecular weight adopted in the present study. This value lies within the recommended range for PVA-based solid polymer electrolytes. These combined factors contributed to a conductivity on the order of  $10^{-4}\text{S/cm}$ .

As shown in Table 5.15, the composites PVA/LiAc-based and PVA/ $\text{LiClO}_4$ /cellulose are derived from two recent studies focused on PVA ma-

trices [171, 172]. In these works, lithium acetate (LiAc) is explored as an alternative ionic salt, while cellulose is introduced as a reinforcing agent alongside the lithium salt. Both cases reported improvements in ionic conductivity; however, the incorporation of cellulose resulted in a reduction in mechanical performance, specifically in terms of elongation at break.

Table 5.15: Comparison of calculated  $\sigma_{DC}$  values for PVA-based membranes synthesized with the results reported in the literature.

Sample	$\sigma_{DC}$ (S/cm)
PVA-7% LiOH	$1.02 \times 10^{-5}$
PVA-10% LiClO <sub>4</sub>	$3.65 \times 10^{-6}$
PVA-7% LiOH [89]	$1.33 \times 10^{-3}$
PVA-20% LiClO <sub>4</sub> [86]	$4.00 \times 10^{-6}$
PEO/PVA/LiOH [32]	$1.25 \times 10^{-4}$
PVA/LiAc-based [171]	$2.21 \times 10^{-5}$
PVA/ LiClO <sub>4</sub> /cellulose [172]	$1.31 \times 10^{-4}$

Among the results obtained, another one interesting finding is related to the crystalline behavior of the membranes, evaluated through XRD and DSC analyses, as well as the accompanying thermal, mechanical parameters. It is generally expected that the incorporation of lithium salts into polymer-based materials leads to a progressive decrease in crystallinity. This reduction is typically associated with increased structural disorder and the disruption of polymer chain packing, resulting in enhanced ionic mobility due to a more amorphous character—albeit at the cost of mechanical and thermal stability. This trend is widely reported in the literature and represents the conventional understanding of salt–polymer interactions in solid-state electrolyte systems [4, 53, 3].

However, the results observed in this study deviate from this common behavior. In the case of the PVA/LiOH system, the crystallinity was found to slightly increase with the addition of the salt, which also led to improvements in both thermal stability and ionic conductivity. This suggests that, under certain conditions, LiOH can pro-

mote a degree of structural organization rather than disrupt it. For the PVA/LiClO<sub>4</sub> membranes, the crystallinity exhibited a non-monotonic trend, varying with salt concentration. These variations are likely associated with the appearance of microstructural defects such as cracks and agglomerates at higher concentrations; nonetheless, mechanical integrity and ionic conductivity remained enhanced across the samples.

Similar observations have been reported in the literature. Sheela et al. (2016) [173] showed that LiClO<sub>4</sub> can increase crystallinity in PVA/NaAlg composites at certain concentrations due to Li<sup>+</sup>–OH interactions and enhanced free volume, which promote chain packing and ordering. Likewise, Putri et al. (2020) [32] found that adding LiOH to PEO/PVA matrices did not significantly disrupt the semicrystalline structure, preserving mechanical and thermal stability. These findings reinforce that, while crystallinity reduction is common, structural preservation—or even enhancement—can occur depending on the salt type, concentration, and polymer–ion interactions.

## 6 CONCLUSIONS

The PVA/LiOH and PVA/LiClO<sub>4</sub> polymeric membranes were successfully prepared via solvent casting, exhibiting uniform thickness of approximately 0.1 mm. FT-IR analysis revealed interactions between Li<sup>+</sup> ions and the polymer matrix, evidenced by redshifts in the O–H (3271 cm<sup>-1</sup> to 3233 cm<sup>-1</sup>) and C–C (1428 cm<sup>-1</sup> to 1409 cm<sup>-1</sup>) vibrational bands, indicating changes in chemical force constants. XRD patterns matched the *P2<sub>1</sub>/m* space group (monoclinic symmetry) as determined by Rietveld refinement, which also indicated a semicrystalline/amorphous nature with crystallinity around 30%. Morphological analysis showed homogeneous surfaces, with a few agglomerates in PVA/LiOH membranes and signs of internal stresses and cracks in PVA/LiClO<sub>4</sub> samples at higher salt concentrations.

First-principles studies using DFT revealed that the effects observed in the FT-IR spectra are primarily attributed to ionic coordination mechanism between the lithium ions and the polymer matrix. This interaction occurs with Li–O bond lengths ranging approximately from 1.85 Å to 1.96 Å for the PVA-1+Li system, and from 1.87 Å to 1.99 Å for PVA-2+Li. The formation energies were calculated as -1.27 eV and -0.97 eV, respectively, indicating that the PVA-1+Li configuration has a lower formation energy and a higher probability of formation than more favorable and stable coordination complex. These interactions contribute to the modification of the vibrational modes discussed in the FT-IR analysis.

Thermal analyses (TGA–DSC) were used to determine  $T_g$ ,  $T_m$ ,  $T_D$ , and the degree of crystallinity of the samples, which ranged from 13.6% to 14.6%. These crystallinity values were consistent with the XRD results, showing a slight increase with the incorporation of lithium salts. In PVA–LiOH membranes, the thermal parameters exhibited an upward trend: the pure PVA membrane showed  $T_g = 77.09^\circ\text{C}$ ,  $T_m = 195.9^\circ\text{C}$ , and  $T_D = 297^\circ\text{C}$ , which increased to  $T_g = 84.3^\circ\text{C}$ ,  $T_m = 197.5^\circ\text{C}$ , and  $T_D = 299^\circ\text{C}$  for

samples containing up to 9% LiOH and 5% LiClO<sub>4</sub>. The maximum degradation rate, identified by the DTG peak, was observed at 330 °C. In contrast, PVA/LiClO<sub>4</sub> membranes with 10% salt exhibited a marked change in thermal behavior, characterized by a rapid and intense mass loss.

Mechanical analysis performed by DMA and Strain-stress indicated that the membranes retained adequate mechanical strength, with the storage modulus remaining within 900 MPa. Moreover, the membranes exhibited good flexibility, with strain values exceeding of 303% for PVA and 345% for 10% LiClO<sub>4</sub>. These results demonstrate a favorable balance between mechanical strength and flexibility, which is essential for electrolyte applications.

CIS, modeled using equivalent circuit models, the Havriliak–Negami (HN) formalism, and Jonscher’s universal power law, revealed a decrease in bulk resistance and, consequently, an increase in ionic conductivity. The resulting ionic conductivity of the pure polymer membrane was  $1.53 \times 10^{-9}$  S/cm, increasing to  $3.65 \times 10^{-6}$  S/cm for the PVA/LiClO<sub>4</sub> membranes and reaching  $1.02 \times 10^{-5}$  S/cm for the PVA–7%LiOH samples—representing the best-performing compositions. These values indicate a higher concentration of mobile ionic charge carriers and are associated with a rapid ionic relaxation process occurring in less than  $10^{-5}$  s.

In general, solvent evaporation limits membrane synthesis for mechanical testing, as precise control of thickness is technically challenging. Similarly, data analysis is complicated by overlapping polarization and conduction effects, requiring the conductivity spectrum to be assessed over specific frequency ranges. Furthermore, the ab initio study is limited to linear polymer chains, which may represent potential constraints.

Despite the limitations, the results were successful analysed and they indicated that PVA/LiClO<sub>4</sub> and PVA/LiOH membranes are promising materials, exhibiting improvements in ionic, structural, thermal, and mechanical properties, and thus merit further investigation for potential application as solid electrolytes.

## 6.1 Perspectives for Future Studies

Based on these findings, two main research directions are proposed for future work:

- (i) **Experimental perspective:** The synthesis route can be extended to improve membrane performance by testing the use of organic solvents such as DMSO and DMF, alternative lithium salts, and polymer blending/composites strategies, to enhance flexibility, structurally and ionic conductivity.
- (ii) **Theoretical perspective:** DFT should be further employed to investigate other host polymers and lithium salts. Additionally, Molecular Dynamics (MD) simulations are encouraged to explore polymer conformations and evaluate the influence of solvent environments on structural and transport properties.



## REFERENCES

- [1] FINGER, S.; PICCOLINO, M.; STAHNISCH, F. W. Alexander von Humboldt: galvanism, animal electricity, and self-experimentation part 1: formative years, naturphilosophie, and galvanism. *Journal of the History of the Neurosciences*, Taylor & Francis, v. 22, n. 3, p. 225–260, 2013.
- [2] BURETEA, D.; CORMOS, C. Hybrid car battery management. *CNCSIS*, p. 503–509, 2007.
- [3] ARYA, A.; SHARMA, A. A glimpse on all-solid-state li-ion battery (asslib) performance based on novel solid polymer electrolytes: a topical review. *Journal of Materials Science*, Springer, v. 55, n. 15, p. 6242–6304, 2020.
- [4] DENNIS, J. O. *et al.* A review of current trends on polyvinyl alcohol (pva)-based solid polymer electrolytes. *Molecules*, MDPI, v. 28, n. 4, p. 1781, 2023.
- [5] VAGANOV, G. *et al.* Influence of molecular weight on thermal and mechanical properties of carbon-fiber-reinforced plastics based on thermoplastic partially crystalline polyimide. *Polymers*, MDPI, v. 15, n. 13, p. 2922, 2023.
- [6] RAYUNG, M. *et al.* Bio-based polymer electrolytes for electrochemical devices: Insight into the ionic conductivity performance. *Materials*, MDPI, v. 13, n. 4, p. 838, 2020.
- [7] RIAZI, K. *et al.* Polystyrene comb architectures as model systems for the optimized solution electrospinning of branched polymers. *Polymer*, Elsevier, v. 104, p. 240–250, 2016.
- [8] NAYAB, S. S. *et al.* Anti-foulant ultrafiltration polymer composite membranes incorporated with composite activated carbon/chitosan and activated carbon/thiolated chitosan with enhanced hydrophilicity. *Membranes*, MDPI, v. 11, n. 11, p. 827, 2021.
- [9] XUE, Z.; HE, D.; XIE, X. Poly (ethylene oxide)-based electrolytes for lithium-ion batteries. *Journal of Materials Chemistry A*, Royal Society of Chemistry, v. 3, n. 38, p. 19218–19253, 2015.
- [10] AHMED, M. B.; AZIZ, S. B.; MURAD, A. R. Diffusion and ion carrier mobility studies in binary spes based on pva integrated with k+ ion provider salt: structural and electrical insights. *Ionics*, Springer, v. 28, n. 11, p. 5153–5169, 2022.
- [11] BUNN, C. Crystal structure of polyvinyl alcohol. *Nature*, Nature Publishing Group UK London, v. 161, n. 4102, p. 929–930, 1948.
- [12] GREENHOE, B. M. *et al.* Universal power law behavior of the ac conductivity versus frequency of agglomerate morphologies in conductive carbon nanotube-reinforced

- epoxy networks. *Journal of Polymer Science Part B: Polymer Physics*, Wiley Online Library, v. 54, n. 19, p. 1918–1923, 2016.
- [13] MARCELLI, A. *et al.* Biological applications of synchrotron radiation infrared spectromicroscopy. *Biotechnology Advances*, Elsevier, v. 30, n. 6, p. 1390–1404, 2012.
- [14] Materion. All About Tensile Testing: How to Set Up Your Samples for Accurate Results. 2024. Accessed: 2025-04-21. Disponível em: <https://www.materion.com/de/insights/material-matters-blog/all-about-tensile-testing-how-to-set-up-your-samples-for-accurate-results>.
- [15] NAWAZ, A.; HÜMMELGEN, I. A. Poly (vinyl alcohol) gate dielectric in organic field-effect transistors. *Journal of Materials Science: Materials in Electronics*, Springer, v. 30, n. 6, p. 5299–5326, 2019.
- [16] OLABISI, O.; ADEWALE, K. Handbook of Thermoplastics. [S.l.]: CRC Press, 2016.
- [17] MACDONALD, J. R. Impedance spectroscopy: emphasizing solid materials and systems. *Applied Optics*, v. 28, n. 6, p. 1083, 1989.
- [18] SZE, S. M.; LI, Y.; NG, K. K. Physics of Semiconductor Devices. [S.l.]: John Wiley & Sons, 2021.
- [19] HOSSAIN, N. *et al.* Advances and significances of nanoparticles in semiconductor applications—a review. *Results in Engineering*, Elsevier, v. 19, p. 101347, 2023.
- [20] JURASZ, J. *et al.* A review on the complementarity of renewable energy sources: Concept, metrics, application and future research directions. *Solar Energy*, Elsevier, v. 195, p. 703–724, 2020.
- [21] WARSINGER, D. M. *et al.* A review of polymeric membranes and processes for potable water reuse. *Progress in Polymer Science*, Elsevier, v. 81, p. 209–237, 2018.
- [22] PERRY, J. D.; NAGAI, K.; KOROS, W. J. Polymer membranes for hydrogen separations. *MRS Bulletin*, Cambridge University Press, v. 31, n. 10, p. 745–749, 2006.
- [23] SHIOHARA, A.; PRIETO-SIMON, B.; VOELCKER, N. H. Porous polymeric membranes: Fabrication techniques and biomedical applications. *Journal of Materials Chemistry B*, v. 9, n. 9, p. 2129–2154, 2021.
- [24] KIM, D. J.; JO, M. J.; NAM, S. Y. A review of polymer–nanocomposite electrolyte membranes for fuel cell application. *Journal of Industrial and Engineering Chemistry*, Elsevier, v. 21, p. 36–52, 2015.
- [25] XI, G. *et al.* Polymer-based solid electrolytes: material selection, design, and application. *Advanced Functional Materials*, Wiley Online Library, v. 31, n. 9, p. 2007598, 2021.
- [26] WU, K. *et al.* Incombustible solid polymer electrolytes: A critical review and perspective. *Journal of Energy Chemistry*, Elsevier, v. 93, p. 264–281, 2024.

- [27] WU, M. *et al.* Fire-safe polymer electrolyte strategies for lithium batteries. *Energy Storage Materials*, Elsevier, v. 66, p. 103174, 2024.
- [28] LI, Z. *et al.* Ionic conduction in polymer-based solid electrolytes. *Advanced Science*, Wiley Online Library, v. 10, n. 10, p. 2201718, 2023.
- [29] NAGARKAR, R.; PATEL, J. *et al.* Polyvinyl alcohol: a comprehensive study. *Acta Scientiarum. Pharmaceutica*, v. 3, n. 4, p. 34–44, 2019.
- [30] NASAR, G.; KHAN, M. S.; KHALIL, U. Structural study of PVA composites with inorganic salts by X-ray diffraction. *Journal of the Pakistan Materials Society*, v. 3, n. 2, p. 67, 2009.
- [31] GARCIA, P. V. *et al.* PVA blends and nanocomposites: properties and applications — A review. *Green-Based Nanocomposite Materials and Applications*, Springer, p. 191–206, 2023.
- [32] PUTRI, R. M. *et al.* PEO/PVA/LiOH solid polymer electrolyte prepared via ultrasound-assisted solution cast method. *Journal of Non-Crystalline Solids*, Elsevier, v. 556, p. 120549, 2021.
- [33] LOBO-GUERRERO, A. X-ray analysis and Rietveld refinement of polyvinyl alcohol. *Materials Letters*, Elsevier, v. 265, p. 127434, 2020.
- [34] BHAVANI, S. *et al.* Studies on structural, electrical, and dielectric properties of nickel-ion-conducting polyvinyl alcohol based polymer electrolyte films. *Journal of Materials Science: Materials in Electronics*, Springer, v. 28, p. 13344–13349, 2017.
- [35] RADHA, K. *et al.* Synthesis and impedance analysis of proton-conducting polymer electrolyte PVA: NH<sub>4</sub>F. *Ionics*, Springer, v. 19, p. 1437–1447, 2013.
- [36] BAILLE, J. B. A Wonders of Electricity. [S.l.]: Scribner, Armstrong, and Company, 1872. 34–37 p.
- [37] ROSA, A. V. D.; ORDONEZ, J. C. Fundamentals of Renewable Energy Processes. [S.l.]: Academic Press, 2021.
- [38] BERG, K. C. de. The significance of the origin of physical chemistry for physical chemistry education: the case of electrolyte solution chemistry. *Chemistry Education Research and Practice*, Royal Society of Chemistry, v. 15, n. 3, p. 266–275, 2014.
- [39] ROSS, S.; FARADAY, M. Faraday consults the scholars: the origins of the terms of electrochemistry. *Notes and Records of the Royal Society of London*, The Royal Society London, v. 16, n. 2, p. 187–220, 1961.
- [40] WISNIAK, J. Electrochemistry and fuel cells: the contribution of William Robert Grove. *Indian Journal of History of Science*, Springer, v. 50, n. 3, p. 476–490, 2015.
- [41] JENSEN, W. B. The Leclanché cell. *Notes from the Oesper Collections*, 2014.
- [42] SILVA, B. O. d. *et al.* Série histórica da composição química de pilhas alcalinas e zinco-carbono fabricadas entre 1991 e 2009. *Química Nova*, SciELO Brasil, v. 34, p. 812–818, 2011.

- [43] TAKAMURA, T. Primary batteries—aqueous systems | alkaline manganese–zinc. Elsevier, 2009.
- [44] RAND, D. A.; MOSELEY, P. T. Energy storage with lead–acid batteries. *Electrochemical Energy Storage for Renewable Sources and Grid Balancing*. [S.l.]: Elsevier, 2015. p. 201–222.
- [45] PARK, M. *et al.* Practical challenges associated with catalyst development for the commercialization of Li-air batteries. *Journal of Electrochemical Science and Technology*, The Korean Electrochemical Society, v. 5, n. 1, p. 1–18, 2014.
- [46] BERNARD, P.; LIPPERT, M. Nickel–cadmium and nickel–metal hydride battery energy storage. In: *Electrochemical Energy Storage for Renewable Sources and Grid Balancing*. [S.l.]: Elsevier, 2015. p. 223–251.
- [47] STEVENSON, K. J. The Origin, Development, and Future of the Lithium-Ion Battery. [S.l.]: Springer, 2012. 2017–2018 p.
- [48] RANGARAJAN, S. S. *et al.* Lithium-ion batteries—the crux of electric vehicles with opportunities and challenges. *Clean Technologies*, MDPI, v. 4, n. 4, p. 908–930, 2022.
- [49] RAHARDIAN, S. *et al.* Review of solid-state battery technology progress. In: IEEE. *2019 6th International Conference on Electric Vehicular Technology (ICEVT)*. [S.l.], 2019. p. 310–315.
- [50] RANA, S.; THAKUR, R. C.; DOSANJH, H. S. Ionic liquids as battery electrolytes for lithium-ion batteries: Recent advances and future prospects. *Solid State Ionics*, Elsevier, v. 400, p. 116340, 2023.
- [51] RESEARCH, G. V. *Battery Electrolyte Market Analysis*. 2024. Accessed: 2024-04-18. Disponível em: <<https://www.grandviewresearch.com/industry-analysis/battery-electrolyte-market-report>>.
- [52] ZHANG, L. *et al.* Recent advances in electrochemical impedance spectroscopy for solid-state batteries. *Energy Storage Materials*, Elsevier, p. 103378, 2024.
- [53] YANG, H.; WU, N. Ionic conductivity and ion transport mechanisms of solid-state lithium-ion battery electrolytes: A review. *Energy Science & Engineering*, Wiley Online Library, v. 10, n. 5, p. 1643–1671, 2022.
- [54] FAMPRIKIS, T. *et al.* Fundamentals of inorganic solid-state electrolytes for batteries. *Nature Materials*, Nature Publishing Group UK London, v. 18, n. 12, p. 1278–1291, 2019.
- [55] DOMINGUEZ, L. A. *et al.* Investigating surface and wettability properties of Na<sub>2</sub>Ti<sub>3</sub>O<sub>7</sub>/Na<sub>2</sub>Ti<sub>6</sub>O<sub>13</sub>/PVA composites. *Surface Topography: Metrology and Properties*, IOP Publishing, v. 11, n. 4, p. 045008, 2023.
- [56] SILVA-PEREIRA, J. *et al.* Electrical response of La<sub>2/3-x</sub>Li<sub>3x</sub>TiO<sub>3</sub> ceramics obtained by spark plasma sintering. In: EDP SCIENCES. *EPJ Web of Conferences*. [S.l.], 2020. v. 233, p. 04003.

- [57] MILERIO, J. V. G. *et al.* Tuning ionic conductivity and thermal stability in POMA-enriched LLZO composites for next-generation lithium-ion batteries. *The Journal of Physical Chemistry C*, ACS Publications, v. 129, n. 19, p. 9127–9139, 2025.
- [58] COSTA, S. D. S. *et al.* Temperature dependence of the electrical properties of  $\text{Na}_2\text{Ti}_3\text{O}_7/\text{Na}_2\text{Ti}_6\text{O}_{13}$ /POMA composites. *Molecules*, MDPI, v. 27, n. 18, p. 5756, 2022.
- [59] CHAAR, S. *et al.* Sonochemical synthesis and characterization of the biphasic compound  $\text{Na}_2\text{Ti}_3\text{O}_7/\text{Na}_2\text{Ti}_6\text{O}_{13}$ . *Materials Research*, SciELO Brasil, v. 24, n. suppl 1, p. e20210011, 2021.
- [60] JIANG, S. *et al.* MOFs containing solid-state electrolytes for batteries. *Advanced Science*, Wiley Online Library, v. 10, n. 10, p. 2206887, 2023.
- [61] ZHANG, X. *et al.* Advancements and challenges in organic–inorganic composite solid electrolytes for all-solid-state lithium batteries. *Nano-Micro Letters*, Springer, v. 17, n. 1, p. 2, 2025.
- [62] DONG, X. *et al.* Polymers and solvents used in membrane fabrication: a review focusing on sustainable membrane development. *Membranes*, MDPI, v. 11, n. 5, p. 309, 2021.
- [63] KHALIFEH, S. 1—Introduction to polymers for electronic engineers. *Polymers in Organic Electronics*, Elsevier, p. 1–31, 2020.
- [64] MCKEEN, L. Introduction to plastics and polymers compositions. *The Effect of UV Light and Weather on Plastics and Elastomers*, William Andrew Publishing: Boston, p. 1–16, 2013.
- [65] SHIVASHARANA, C.; KESTI, S. S. Physical and chemical characterization of low density polyethylene and high density polyethylene. *Journal of Advanced Scientific Research*, v. 10, n. 03, p. 30–34, 2019.
- [66] TAN, X.; RODRIGUE, D. A review on porous polymeric membrane preparation. Part II: Production techniques with polyethylene, polydimethylsiloxane, polypropylene, polyimide, and polytetrafluoroethylene. *Polymers*, MDPI, v. 11, n. 8, p. 1310, 2019.
- [67] BHATIA, S.; BHATIA, S. Natural polymers vs synthetic polymer. *Natural Polymer Drug Delivery Systems: Nanoparticles, Plants, and Algae*, Springer, p. 95–118, 2016.
- [68] NGAI, K. S. *et al.* A review of polymer electrolytes: fundamental, approaches and applications. *Ionics*, Springer, v. 22, p. 1259–1279, 2016.
- [69] BARANWAL, J. *et al.* Biopolymer: A sustainable material for food and medical applications. *Polymers*, MDPI, v. 14, n. 5, p. 983, 2022.
- [70] HSISSOU, R. *et al.* Polymer composite materials: A comprehensive review. *Composite Structures*, Elsevier, v. 262, p. 113640, 2021.

- [71] VERDIER, N. *et al.* Challenges in solvent-free methods for manufacturing electrodes and electrolytes for lithium-based batteries. *Polymers*, MDPI, v. 13, n. 3, p. 323, 2021.
- [72] ISLAM, M. S. *et al.* A review on fabrication of nanofibers via electrospinning and their applications. *SN Applied Sciences*, Springer, v. 1, p. 1–16, 2019.
- [73] ROZELLE, L. *et al.* Phase inversion membranes. *Encyclopedia of Separation Science*, Academic Press, Cambridge, MA, USA, p. 3331–3346, 2000.
- [74] THIAM, B. G. *et al.* 3D printed and conventional membranes—a review. *Polymers*, MDPI, v. 14, n. 5, p. 1023, 2022.
- [75] BALAJI, J. *et al.* Recent developments in sol-gel based polymer electrolyte membranes for vanadium redox flow batteries—a review. *Polymer Testing*, Elsevier, v. 89, p. 106567, 2020.
- [76] HIMMA, N. F.; WARDANI, A. K.; WENTEN, I. G. Preparation of superhydrophobic polypropylene membrane using dip-coating method: the effects of solution and process parameters. *Polymer-Plastics Technology and Engineering*, Taylor & Francis, v. 56, n. 2, p. 184–194, 2017.
- [77] KIDAMBI, P. R. *et al.* A scalable route to nanoporous large-area atomically thin graphene membranes by roll-to-roll chemical vapor deposition and polymer support casting. *ACS Applied Materials & Interfaces*, ACS Publications, v. 10, n. 12, p. 10369–10378, 2018.
- [78] GUO, P. *et al.* Nanomaterial preparation by extrusion through nanoporous membranes. *Small*, Wiley Online Library, v. 14, n. 18, p. 1703493, 2018.
- [79] CHATTOPADHYAY, J.; PATHAK, T. S.; SANTOS, D. M. Applications of polymer electrolytes in lithium-ion batteries: a review. *Polymers*, MDPI, v. 15, n. 19, p. 3907, 2023.
- [80] SUBRAMANIA, A. *et al.* A one-step procedure to prepare LiASF<sub>6</sub> and other allied lithium-based fluoro compounds used as electrolyte in lithium cells. *Ionics*, Springer, v. 12, p. 327–329, 2006.
- [81] ARCHULETA, M. M. Toxicity of materials used in the manufacture of lithium batteries. *Journal of Power Sources*, Elsevier, v. 54, n. 1, p. 138–142, 1995.
- [82] SIVAKUMAR, M. *et al.* Electrochemical studies on [(1-x) PVA-xPMMA] solid polymer blend electrolytes complexed with LiBF<sub>4</sub>. *Materials Chemistry and Physics*, Elsevier, v. 97, n. 2-3, p. 330–336, 2006.
- [83] YAP, A. Y.; LIEW, C.-W. Structural, thermal, and electrochemical studies on PVA-LiTF-TiO<sub>2</sub> nanocomposite polymer electrolyte and the performance on electric double layer capacitor application. *Ionics*, Springer, v. 28, n. 9, p. 4111–4128, 2022.
- [84] YOUNESI, R. *et al.* Lithium salts for advanced lithium batteries: Li-metal, Li-O<sub>2</sub>, and Li-S. *Energy & Environmental Science*, Royal Society of Chemistry, v. 8, n. 7, p. 1905–1922, 2015.

- [85] ABARNA, S.; HIRANKUMAR, G. Vibrational, electrical, dielectric and optical properties of PVA-LiPF<sub>6</sub> solid polymer electrolytes. *Mater Sci-Pol*, v. 37, n. 3, p. 331–337, 2019.
- [86] GUNAWAN, I.; SUGENG, B. *et al.* Synthesis and characterization of PVA blended LiClO<sub>4</sub> as electrolyte material for battery Li-ion. *IOP Conference Series: Materials Science and Engineering*, IOP Publishing, v. 223, n. 1, p. 012039, 2017.
- [87] RANGASAMY, V. S.; THAYUMANASUNDARAM, S.; LOCQUET, J.-P. Solid polymer electrolytes with poly(vinyl alcohol) and piperidinium based ionic liquid for Li-ion batteries. *Solid State Ionics*, Elsevier, v. 333, p. 76–82, 2019.
- [88] MAROM, R. *et al.* Revisiting LiClO<sub>4</sub> as an electrolyte for rechargeable lithium-ion batteries. *Journal of the Electrochemical Society*, IOP Publishing, v. 157, n. 8, p. A972, 2010.
- [89] AJI, M. P. *et al.* Electrical conductivity study of polymer electrolyte magnetic nanocomposite based poly(vinyl) alcohol (PVA) doping lithium and nickel salt. *AIP Conference Proceedings*, American Institute of Physics, v. 1284, n. 1, p. 51–54, 2010.
- [90] VERDUZCO, J. C. *et al.* Hybrid polymer-garnet materials for all-solid-state energy storage devices. *ACS Omega*, ACS Publications, v. 6, n. 24, p. 15551–15558, 2021.
- [91] RATHOD, S. G. *et al.* High mechanical and pressure sensitive dielectric properties of graphene oxide doped PVA nanocomposites. *RSC Advances*, Royal Society of Chemistry, v. 6, n. 81, p. 77977–77986, 2016.
- [92] YANG, W. *et al.* Effect of cellulose nanocrystals and lignin nanoparticles on mechanical, antioxidant and water vapour barrier properties of glutaraldehyde crosslinked PVA films. *Polymers*, MDPI, v. 12, n. 6, p. 1364, 2020.
- [93] HALLE, F.; HOFMANN, W. Faserdiagramme von Polyvinylalkohol. *Naturwissenschaften*, Springer, v. 23, n. 45, p. 770–770, 1935.
- [94] MOONEY, R. C. An X-ray study of the structure of polyvinyl alcohol. *Journal of the American Chemical Society*, ACS Publications, v. 63, n. 10, p. 2828–2832, 1941.
- [95] BUNN, C.; PEISER, H. Mixed crystal formation in high polymers. *Nature*, Nature Publishing Group UK, v. 159, n. 4031, p. 161–162, 1947.
- [96] OLIVEIRA, L. S. de *et al.* Phase transformations in a nitige system induced by high energy milling. *Journal of Solid State Chemistry*, Elsevier, v. 281, p. 121056, 2020.
- [97] CHOLANT, C. M. *et al.* Study of the conductivity of solid polymeric electrolyte based on PVA/GA blend with addition of acetic acid. *Journal of Solid State Electrochemistry*, Springer, v. 24, p. 1867–1875, 2020.
- [98] MONTOYA-ESCOBAR, N. *et al.* Use of Fourier series in X-ray diffraction (XRD) analysis and Fourier-transform infrared spectroscopy (FTIR) for estimation of crystallinity in cellulose from different sources. *Polymers (Basel)*, v. 14, p. 5199, 2022.

- [99] AHMED, M. B. *et al.* The study of ion transport parameters associated with dissociated cation using EIS model in solid polymer electrolytes (SPEs) based on PVA host polymer: XRD, FTIR, and dielectric properties. *Arabian Journal of Chemistry*, Elsevier, v. 15, n. 11, p. 104196, 2022.
- [100] SAU, S.; PANDIT, S.; KUNDU, S. Crosslinked poly(vinyl alcohol): Structural, optical and mechanical properties. *Surfaces and Interfaces*, Elsevier, v. 25, p. 101198, 2021.
- [101] ALI, Z.; EISA, W. Characterization of electron beam irradiated polyvinyl alcohol/polyethylene glycol blends. *Journal of Scientific Research*, v. 6, n. 1, p. 29–42, 2014.
- [102] RODRÍGUEZ-CARVAJAL, J. Recent advances in magnetic structure determination by neutron powder diffraction. *Physica B: Condensed Matter*, Elsevier, v. 192, n. 1-2, p. 55–69, 1993.
- [103] LUTTEROTTI, L. *et al.* Quantitative analysis of silicate glass in ceramic materials by the Rietveld method. *Materials Science Forum*, Trans Tech Publications, v. 278, n. 281, p. 87–92, 1998.
- [104] LARSON, A. C.; DREELE, R. B. V. General structure analysis system (GSAS)(report LAUR 86-748). *Los Alamos National Laboratory*, Los Alamos, New Mexico, 2004.
- [105] BELSKY, A. *et al.* New developments in the inorganic crystal structure database (ICSD): accessibility in support of materials research and design. *Structural Science*, International Union of Crystallography, v. 58, n. 3, p. 364–369, 2002.
- [106] GROOM, C. R. *et al.* The Cambridge Structural Database. *Structural Science*, International Union of Crystallography, v. 72, n. 2, p. 171–179, 2016.
- [107] GRAŽULIS, S. *et al.* Crystallography Open Database—an open-access collection of crystal structures. *Applied Crystallography*, International Union of Crystallography, v. 42, n. 4, p. 726–729, 2009.
- [108] KULASEKARAN, P.; MAHIMAI, B. M.; DEIVANAYAGAM, P. Novel cross-linked poly(vinyl alcohol)-based electrolyte membranes for fuel cell applications. *RSC Advances*, Royal Society of Chemistry, v. 10, n. 44, p. 26521–26527, 2020.
- [109] GOPI, K. H.; DHAVALE, V. M.; BHAT, S. D. Development of polyvinyl alcohol/chitosan blend anion exchange membrane with mono and di quaternizing agents for application in alkaline polymer electrolyte fuel cells. *Materials Science for Energy Technologies*, Elsevier, v. 2, n. 2, p. 194–202, 2019.
- [110] HIRANKUMAR, G.; MEHTA, N. Effect of incorporation of different plasticizers on structural and ion transport properties of PVA-LiClO<sub>4</sub> based electrolytes. *Heliyon*, Elsevier, v. 4, n. 12, 2018.
- [111] SAROJ, A.; SINGH, R. K. Thermal, dielectric and conductivity studies on PVA/ionic liquid [EMIM][ETSO<sub>4</sub>] based polymer electrolytes. *Journal of Physics and Chemistry of Solids*, Elsevier, v. 73, n. 2, p. 162–168, 2012.



- [112] AZIZ, S. B. *et al.* Employing of Trukhan model to estimate ion transport parameters in PVA based solid polymer electrolyte. *Polymers*, MDPI, v. 11, n. 10, p. 1694, 2019.
- [113] ZHU, Y. *et al.* A new single-ion polymer electrolyte based on polyvinyl alcohol for lithium ion batteries. *Electrochimica Acta*, Elsevier, v. 87, p. 113–118, 2013.
- [114] ABDELHAMIED, M.; ABDELREHEEM, A.; ATTA, A. Influence of ion beam and silver nanoparticles on dielectric properties of flexible PVA/PANI polymer composite films. *Plastics, Rubber and Composites*, SAGE Publications, v. 51, n. 1, p. 1–12, 2022.
- [115] NANGIA, R.; SHUKLA, N. K.; SHARMA, A. Frequency and temperature-dependent impedance spectroscopy of PVA/PEG polymer blend film. *High Performance Polymers*, SAGE Publications, v. 30, n. 8, p. 918–926, 2018.
- [116] SHCHERBAKOV, V. V. *et al.* Dielectric characteristics, electrical conductivity and solvation of ions in electrolyte solutions. *Materials*, MDPI, v. 14, n. 19, p. 5617, 2021.
- [117] BARSOUKOV, E.; MACDONALD, J. R. (Ed.). *Impedance Spectroscopy: Theory, Experiment, and Applications*. 3. ed. Hoboken, NJ: Wiley, 2018.
- [118] COLE, K. S. Permeability and impermeability of cell membranes for ions. *Cold Spring Harbor Symposia on Quantitative Biology*, Cold Spring Harbor Laboratory Press, v. 8, p. 110–122, 1940.
- [119] MACDONALD, J. R. Note on the parameterization of the constant-phase admittance element. *Solid State Ionics*, Elsevier, v. 13, n. 2, p. 147–149, 1984.
- [120] ASSOCIATES, I. S. ZView: Impedance Spectroscopy Analysis Software. 2025. Accessed: 2025-04-19. Disponível em: <<http://www.scribner.com/zview.html>>.
- [121] VADHVA, P. *et al.* Electrochemical impedance spectroscopy for all-solid-state batteries: theory, methods and future outlook. *ChemElectroChem*, Wiley Online Library, v. 8, n. 11, p. 1930–1947, 2021.
- [122] DEBYE, P. J. W. *Polar molecules*. [S.l.]: Dover Publications, 1929.
- [123] HUNT, A. Non-Debye relaxation and the glass transition. *Journal of Non-Crystalline Solids*, Elsevier, v. 160, n. 3, p. 183–227, 1993.
- [124] DAS, S.; GHOSH, A. Charge carrier relaxation in different plasticized PEO/PVDF-HFP blend solid polymer electrolytes. *The Journal of Physical Chemistry B*, ACS Publications, v. 121, n. 21, p. 5422–5432, 2017.
- [125] ALLAGUI, A. *et al.* Extended RC impedance and relaxation models for dissipative electrochemical capacitors. *IEEE Transactions on Electron Devices*, IEEE, v. 69, n. 10, p. 5792–5799, 2022.
- [126] JONSCHER, A. K. Dielectric relaxation in solids. *Journal of Physics D: Applied Physics*, IOP Publishing, v. 32, n. 14, p. R57, 1999.

- [127] DHATARWAL, P.; SENGWA, R. Dielectric polarization and relaxation processes of the lithium-ion conducting PEO/PVDF blend matrix-based electrolytes: effect of TiO<sub>2</sub> nanofiller. *SN Applied Sciences*, Springer, v. 2, n. 5, p. 833, 2020.
- [128] FETTER, A. L.; WALECKA, J. D. *Quantum Theory of Many-Particle Systems*. New York: McGraw-Hill, 1971. ISBN 978-0070057075.
- [129] BRUUS, H.; FLENSBERG, K. *Many-body Quantum Theory in Condensed Matter Physics: An Introduction*. Oxford: Oxford University Press, 2004, p. 123–145. ISBN 978-0198520812.
- [130] MONTEIRO, J. R. de M. *Estudo ab initio por DFT+U de monocamadas de Sn<sub>1-x</sub>SeAg<sub>x</sub>, SnSe<sub>1-x</sub>Ag<sub>x</sub> e ZnX (X = O, S, Se, Te)*. Tese (PhD thesis) — Universidade Federal do Amazonas, Manaus, Amazonas, Brazil, 2020.
- [131] ANSARI, S.; ALI, P.; SRIVASTAVA, S. Normal modes, their dispersions and heat capacity of isotactic poly(vinyl alcohol). *Int J Eng Res Technol*, v. 1, n. 9, p. 1–6, 2012.
- [132] MCHALE, J. L. *Molecular Spectroscopy*. [S.l.]: CRC Press, 2017.
- [133] JOSE, J.; SHEHZAD, F.; AL-HARTHI, M. A. Preparation method and physical, mechanical, thermal characterization of poly(vinyl alcohol)/poly(acrylic acid) blends. *Polymer Bulletin*, Springer, v. 71, n. 11, p. 2787–2802, 2014.
- [134] WHEELER, O.; ERNST, S.; CROZIER, R. Molecular weight degradation of polyvinyl acetate on hydrolysis. *Journal of Polymer Science*, Wiley Online Library, v. 8, n. 4, p. 409–423, 1952.
- [135] RAJESWARI, N. *et al.* Structural, vibrational, thermal, and electrical properties of PVA/PVP biodegradable polymer blend electrolyte with CH<sub>3</sub>COONH<sub>4</sub>. *Ionics*, Springer, v. 19, p. 1105–1113, 2013.
- [136] HEMA, M. *et al.* FTIR, XRD and AC impedance spectroscopic study on PVA based polymer electrolyte doped with NH<sub>4</sub>X (X= Cl, Br, I). *Journal of Non-Crystalline Solids*, Elsevier, v. 355, n. 2, p. 84–90, 2009.
- [137] AZIZ, S. B. *et al.* Innovative green chemistry approach to synthesis of Sn<sup>2+</sup>-metal complex and design of polymer composites with small optical band gaps. *Molecules*, MDPI, v. 27, n. 6, p. 1965, 2022.
- [138] RAJENDRAN, S. *et al.* Characterization of PVA–PVDF based solid polymer blend electrolytes. *Physica B: Condensed Matter*, Elsevier, v. 348, n. 1-4, p. 73–78, 2004.
- [139] BRZA, M. *et al.* Metal framework as a novel approach for the fabrication of electric double layer capacitor device with high energy density using plasticized poly(vinyl alcohol): Ammonium thiocyanate based polymer electrolyte. *Arabian Journal of Chemistry*, Elsevier, v. 13, n. 10, p. 7247–7263, 2020.
- [140] ASSENDER, H. E.; WINDLE, A. H. Crystallinity in poly(vinyl alcohol). 1. An X-ray diffraction study of atactic PVOH. *Polymer*, Elsevier, v. 39, n. 18, p. 4295–4302, 1998.

- [141] LIU, F. *et al.* Polymer-ion interaction prompted quasi-solid electrolyte for room-temperature high-performance lithium-ion batteries. *Advanced Materials*, Wiley Online Library, v. 36, n. 45, p. 2409838, 2024.
- [142] SONG, J. *et al.* Strong lithium polysulfide chemisorption on electroactive sites of nitrogen-doped carbon composites for high-performance lithium–sulfur battery cathodes. *Angewandte Chemie*, Wiley Online Library, v. 127, n. 14, p. 4399–4403, 2015.
- [143] ZHENG, X. *et al.* Crown ether grafted graphene oxide/chitosan/polyvinyl alcohol nanofiber membrane for highly selective adsorption and separation of lithium ion. *Nanomaterials*, MDPI, v. 11, n. 10, p. 2668, 2021.
- [144] ZHANG, X. *et al.* Porous polyvinyl alcohol/polyacrylamide hydrogels loaded with HTO lithium-ion sieves for highly rapid and efficient Li<sup>+</sup> extraction. *Desalination*, Elsevier, v. 580, p. 117587, 2024.
- [145] XU, J.; CHEN, P. Selective biosorption of Li<sup>+</sup> in aqueous solution by lithium ion-imprinted material on the surface of chitosan/attapulgite. *International Journal of Biological Macromolecules*, Elsevier, v. 273, p. 133150, 2024.
- [146] HAMZA, M. F. *et al.* Sulfonation of chitosan for enhanced sorption of Li(I) from acidic solutions—application to metal recovery from waste Li-ion mobile battery. *Chemical Engineering Journal*, Elsevier, v. 441, p. 135941, 2022.
- [147] DING, T.; ZHENG, M.; LIN, Y. Adsorption of Li(I) ions through new high-performance electrospun PAN/kaolin nanofibers: A combined experimental and theoretical calculation. *ACS Omega*, ACS Publications, v. 7, n. 13, p. 11430–11439, 2022.
- [148] ABU-SAIED, M. *et al.* Sulfated chitosan/PVA absorbent membrane for removal of copper and nickel ions from aqueous solutions—fabrication and sorption studies. *Carbohydrate Polymers*, Elsevier, v. 165, p. 149–158, 2017.
- [149] SIDDAIAH, T. *et al.* Thermal, structural, optical and electrical properties of PVA/-MAA:EA polymer blend filled with different concentrations of lithium perchlorate. *Journal of Science: Advanced Materials and Devices*, Elsevier, v. 3, n. 4, p. 456–463, 2018.
- [150] HOVINGTON, P. *et al.* Can we detect Li K X-ray in lithium compounds using energy dispersive spectroscopy? *Scanning*, Wiley Online Library, v. 38, n. 6, p. 571–578, 2016.
- [151] MARZANTOWICZ, M. *et al.* Crystalline phases, morphology and conductivity of PEO:LiTFSI electrolytes in the eutectic region. *Journal of Power Sources*, Elsevier, v. 159, n. 1, p. 420–430, 2006.
- [152] OSAKA, N.; MINEMATSU, Y.; TOSAKA, M. Influence of lithium salt-induced phase separation on thermal behaviors of poly(vinylidene fluoride)/ionic liquid gels and pore/void formation by competition with crystallization. *RSC Advances*, Royal Society of Chemistry, v. 8, n. 71, p. 40570–40580, 2018.

- [153] SHI, W. *et al.* Biodiesel production catalyzed by polyvinyl guanidineacetic membrane. *Catalysis Letters*, Springer, v. 151, p. 153–163, 2021.
- [154] PENG, Z.; KONG, L. X. A thermal degradation mechanism of polyvinyl alcohol/silica nanocomposites. *Polymer Degradation and Stability*, Elsevier, v. 92, n. 6, p. 1061–1071, 2007.
- [155] RAJENDRAN, S.; SIVAKUMAR, M.; SUBADEVI, R. Li-ion conduction of plasticized pva solid polymer electrolytes complexed with various lithium salts. *Solid State Ionics*, Elsevier, v. 167, n. 3-4, p. 335–339, 2004.
- [156] AZIZ, S. B. *et al.* The study of the degree of crystallinity, electrical equivalent circuit, and dielectric properties of polyvinyl alcohol (pva)-based biopolymer electrolytes. *Polymers*, MDPI, v. 12, n. 10, p. 2184, 2020.
- [157] DANNOUN, E. M. *et al.* The study of impedance, ion transport properties, eec modeling, dielectric and electrochemical characteristics of plasticized proton conducting pva based electrolytes. *Journal of Materials Research and Technology*, Elsevier, v. 17, p. 1976–1985, 2022.
- [158] SILVA, J. P. da *et al.* Towards a new type of polymer-ceramic composites na2ti3o7/na2ti6o13/pva. *Polymer Bulletin*, Springer, v. 81, n. 9, p. 7855–7874, 2024.
- [159] HEMA, M. *et al.* Structural, vibrational and electrical characterization of pva–nh4br polymer electrolyte system. *Physica B: Condensed Matter*, Elsevier, v. 403, n. 17, p. 2740–2747, 2008.
- [160] SAMSUDIN, A.; KHAIRUL, W. M.; ISA, M. Characterization on the potential of carboxy methylcellulose for application as proton conducting biopolymer electrolytes. *Journal of Non-crystalline solids*, Elsevier, v. 358, n. 8, p. 1104–1112, 2012.
- [161] YUSOF, Y. *et al.* Characterization of starch-chitosan blend-based electrolyte doped with ammonium iodide for application in proton batteries. *Ionics*, Springer, v. 23, p. 681–697, 2017.
- [162] SILVA, J. da *et al.* One-pot synthesis of li3xla2/3- xtio3/pva composite with high tunable electrical attributes governed by the li+ content. *Ceramics International*, Elsevier, v. 50, n. 18, p. 33546–33554, 2024.
- [163] AJI, M. P. *et al.* Electrical and magnetic properties of polymer electrolyte pva. lioh dispersed by fe 3 o 4 nanoparticles. In: AMERICAN INSTITUTE OF PHYSICS. *AIP Conference Proceedings*, [S.l.], v. 1415, n. 1, p. 94–97, 2011.
- [164] CYRIAC, V. *et al.* Ionic conductivity enhancement of pva: carboxymethyl cellulose poly-blend electrolyte films through the doping of nai salt. *Cellulose*, Springer, v. 29, n. 6, p. 3271–3291, 2022.
- [165] BRZA, M. A. *et al.* Characteristics of a plasticized pva-based polymer electrolyte membrane and h+ conductor for an electrical double-layer capacitor: Structural, morphological, and ion transport properties. *Membranes*, MDPI, v. 11, n. 4, p. 296, 2021.

- [166] PAL, P.; GHOSH, A. Broadband dielectric spectroscopy of bmptfsi ionic liquid doped solid-state polymer electrolytes: Coupled ion transport and dielectric relaxation mechanism. *Journal of Applied Physics*, AIP Publishing, v. 128, n. 8, 2020.
- [167] RATHOD, S. G. *et al.* Influence of transport parameters on conductivity of lithium perchlorate-doped poly (vinyl alcohol)/chitosan composites. *Journal of Elastomers & Plastics*, SAGE Publications Sage UK: London, England, v. 48, n. 5, p. 442–455, 2016.
- [168] GONZÁLEZ-CAMPOS, J. B. *et al.* Molecular dynamics analysis of pva-agnp composites by dielectric spectroscopy. *Journal of Nanomaterials*, Wiley Online Library, v. 2012, n. 1, p. 925750, 2012.
- [169] PENG, J. *et al.* Oriented polyvinyl alcohol films using short cellulose nanofibrils as a reinforcement. *Journal of Applied Polymer Science*, Wiley Online Library, v. 132, n. 48, 2015.
- [170] BEGUM, M. H. A. *et al.* Preparation and characterization of polyvinyl alcohol–starch composites reinforced with pulp. *SN Applied Sciences*, Springer, v. 1, p. 1–9, 2019.
- [171] PURWANTI, E. *et al.* Incorporating ionic liquid 1-ethyl-3-methylimidazolium bromide into pva-liac–based solid polymer electrolytes to achieve advanced solid-state lithium-ion batteries. *Journal of Applied Polymer Science*, Wiley Online Library, v. 142, n. 15, p. e56718, 2025.
- [172] PURWANTI, E. *et al.* Polymer electrolyte membrane based on pva/licl<sub>4</sub> nanocomposite reinforced cellulose nanocrystalline from corncob for lithium-ion battery. *Journal of Polymer Science*, Wiley Online Library, v. 62, n. 7, p. 1424–1436, 2024.
- [173] SHEELA, T. *et al.* Ionic conductivity and free volume related microstructural properties of licl<sub>4</sub>/pva/naalg polymer composites: Positron annihilation spectroscopic studies. *Journal of Non-crystalline solids*, Elsevier, v. 454, p. 19–30, 2016.

## SCIENTIFIC IMPACTS

### Published articles:

The following articles, published with the author as the primary contributor, represent notable scientific achievements and reflect high-quality research recognized in the field.


Yan M.C. Pinto, et al. "Understanding the LiOH effect on PVA membranes from an experimental vision and a density functional theory study." *Journal of Materials Science* 58.35 (2023): 13935-13945. <https://doi.org/10.1007/s10853-023-08896-4>

*J Mater Sci*

**Chemical routes to materials**



### Understanding the LiOH effect on PVA membranes from an experimental vision and a density functional theory study

Yan M. C. Pinto<sup>1</sup>, J. P. da Silva<sup>2</sup>, F. X. Nobre<sup>3</sup>, Marcus V. B. do Nascimento<sup>5</sup>, Francisco M. de B. Neto<sup>5</sup>, Diogo P. Oliveira<sup>5</sup>, João C. M. da Costa<sup>5</sup>, José V. G. Milério<sup>5</sup>, E. A. Sanches<sup>1,4</sup>, Angsula Ghosh<sup>1</sup>, L. Aguilera<sup>5</sup>, and Y. Leyet<sup>1,2,\*</sup> 

<sup>1</sup> Departamento de Física de Materiais, Universidade Federal do Amazonas, Manaus, Amazonas, Brazil

<sup>2</sup> LPMaT, Departamento de Engenharia de Materiais, Universidade Federal do Amazonas, Manaus, Amazonas, Brazil

<sup>3</sup> Departamento de Química, Alimentos e Meio Ambiente (DQA), Instituto Federal de Educação, Ciência e Tecnologia do Amazonas, Campus Manaus Centro (CMC), Manaus, Amazonas, Brazil

<sup>4</sup> Laboratório de Polímeros Nanoestruturados (NANOPOL), Universidade Federal do Amazonas, Manaus, Amazonas, Brazil

<sup>5</sup> Instituto de Desenvolvimento Tecnológico, Manaus, Amazonas, Brazil

Y. M. C. Pinto, et al. "Revealing structural and electrical details of PVA/LiClO<sub>4</sub> thermoplastic membranes." *Materials Science and Engineering: B* 302 (2024): 117219. <https://doi.org/10.1016/j.mseb.2024.117219>

Materials Science and Engineering B 302 (2024) 117219



Contents lists available at ScienceDirect

Materials Science & Engineering B

journal homepage: [www.elsevier.com/locate/mseb](http://www.elsevier.com/locate/mseb)



## Revealing structural and electrical details of PVA/LiClO<sub>4</sub> thermoplastic membranes

Y.M.C. Pinto<sup>a</sup>, J.P. da Silva<sup>b</sup>, F.X. Nobre<sup>c</sup>, J. Anglada-Rivera<sup>c</sup>, D. Comedi<sup>d</sup>, R.S. Silva<sup>e</sup>, M.M.S. Paula<sup>a</sup>, S. Michielon de Souza<sup>a</sup>, L. Aguilera<sup>f</sup>, Y. Leyet<sup>a,b,\*</sup>

<sup>a</sup> Departamento de Física, Universidade Federal do Amazonas, Manaus, Amazonas, Brazil

<sup>b</sup> LPMaT, Departamento de Engenharia de Materiais, Universidade Federal do Amazonas, Manaus, Amazonas, Brazil

<sup>c</sup> Departamento de Química, Alimentos e Meio Ambiente - DQA, Instituto Federal de Educação, Ciência e Tecnologia do Amazonas, Campus Manaus Centro - CMC, Manaus, Amazonas, Brazil

<sup>d</sup> Nanoproject - LN and LAFISO, Dep. de Física, Facultad de Ciencias Exactas y Tecnología, Universidad Nacional de Tucumán and INFNOA (CONICET-UNT), Av. Independencia 1800, San Miguel de Tucumán 4000, Argentina

<sup>e</sup> Department of Physics, Federal University of Sergipe, Sergipe, 49100-000, Brazil

<sup>f</sup> INDT, Instituto de Desenvolvimento Tecnológico, Manaus, Amazonas, Brazil

Ativar

The following publications, in which the author contributed as a co-author, further demonstrate active participation in collaborative research efforts within the field.

Silva, J. B., da Silva, Pinto, Y. M. C., Colares, Ruiz, Y. L. "Synergistic Effects of Lithium Doping and Organic Phases on the Electrical and Dielectric Properties of Sodium Titanate Solid-State Electrolytes." *Solid State Sciences* 108036 (2025). <https://doi.org/10.1016/j.solidstatesciences.2025.108036>

Silva, E. C., Pinto, Y. M. C., Aguilera, L., Leyet, Y. "Sonochemical activation for BaTiO<sub>3</sub> synthesis: A rapid and efficient route to the tetragonal phase." *International Journal of Applied Ceramic Technology*, e70054 (2025). <https://doi.org/10.1111/ijac.70054>

**Participation in conferences and events:**

1. 11th Brazilian German Workshop on Applied Surface Science. April 19-21, 2022, Manaus - AM.
2. IX Semana de Ciências e Tecnologia (SECT) do ICE, October 18-21, 2022, Manaus - AM.
3. XX Brazilian Materials Research Society (SBPMat) Meeting. September 25-29, 2022, Foz do Iguaçu - PR.
4. V Workshop de Química Inorgânica (WQI) da UFAM, November 9-11, 2022, Manaus - AM.
5. X Semana de Ciências e Tecnologia (SECT) do ICE, October 17-20, 2023, Manaus - AM.
6. XXI Brazilian Materials Research Society (SBPMat) Meeting. October 1-5, 2023, Maceió - AL.
7. I Meeting on Materials for Energy Applications in Amazonas (MMEA). April 15-17, 2024, Manaus - AM.